Evaluation of Diffuse Reflectance Spectroscopy and Fluorescence Spectroscopy for Detection of Glioma Brain Tumors

Evaluation of Diffuse Reflectance Spectroscopy and Fluorescence Spectroscopy for Detection of Glioma Brain Tumors

by

VINH NGUYEN DU LE, M.Sc.

A Thesis

To Be Submitted to the School of Graduate Studies in Partial Fulfillment of the Requirements for the Degree Doctor of Philosophy

McMaster University

DOCTOR OF PHILOSOPHY (2016)

DEPARTMENT OF MEDICAL PHYSICS & APPLIED RADIATION SCIENCES

MCMASTER UNIVERSITY

HAMILTON, ON

CANADA

TITLE: Evaluation of Diffuse Reflectance Spectroscopy and Fluorescence Spectroscopy for Detection of Glioma Brain Tumors

AUTHOR: Vinh Nguyen Du Le, M.Sc., B.Sc. (The Catholic University of America)

SUPERVISOR: Qiyin Fang, Ph.D.

NUMBER OF PAGES: xiv, 159

Abstract

Imaging instruments are required for accurate tumor resection during neurosurgery, especially in the case of glioblastoma multiforme (GBM) - the most common and aggressive malignant glioma. However, current intraoperative imaging techniques for detection of glioma either suffer low sensitivity and low specificity or require a significant capital cost. Advances in diffuse reflectance spectroscopy and fluorescence spectroscopy have offered high sensitivity and high specificity in differentiating tumors from normal tissues with much lower capital cost. Whereas diffuse reflectance spectroscopy alone and fluorescence spectroscopy alone has been used in limited studies to differentiate normal brain tissues from brain tumors with moderate sensitivity and specificity, low specificity and sensitivity were usually observed when studying high grade glioma (HGG) such as GBM. Furthermore, optical properties and diffuse reflectance signal of HGG and low grade glioma (LGG) have not been observed separately, and thus a relation between optical properties and glioma progression has not been established. Intraoperative differentiation of GBM and LGG can be helpful in making treatment plan at the first surgery.

This thesis focuses on characterizing a previous integrated system of diffuse reflectance spectroscopy and fluorescence spectroscopy to extract optical properties and fluorescence properties of LGG and GBM. First, tissue-simulating phantom models were developed to calibrate the integrated system. The direct method and Mie theory were used to calculate optical scattering of the phantoms while Beer-Lambert's law was used to calculate optical absorption. Second, an experimental method was introduced to recover intrinsic fluorescence because the measured fluorescence signal is likely distorted by the presence of scatterers and absorbers in tissue (i.e. hemoglobin). Third, an experimental method was developed to recover optical properties of both GBM and LGG. In addition, the sensitivity and specificity of the integrated system was optimized.

Acknowledgements

I am very grateful to my Ph.D. supervisor, Dr. Qiyin Fang, for his thoughtful advices, and for valuable learning opportunities he has provided throughout my studying period. I would also like to thank my supervising committee members, Dr. Thomas J. Farrell, Dr. Joseph E. Hayward for their helpful discussions in each project meeting, and for their time and effort on guiding me and editing the manuscripts. In addition, I would like to express my thanks to Dr. Michael S. Patterson who had gave me valuable advices to improve my manuscripts, to Dr. John Provias who had gave me informative discussion on histopathology of brain tumors, and to Dr. Naresh Murty for his time and efforts of delivering brain tumor specimen for the study.

Moreover, I would like to say thank you to all of my good friends and colleagues, who have been always so helpful and giving me such a great experience at McMaster during these years. In particular, I want to thank Zhaojun Nie for her detailed explanation on the time-resolved fluorescence system, Derrek Cappon for his helpful discussion on the diffuse reflectance spectroscopy. In addition, I would like to thank Sharon Goh for her help ordering the chemicals, and to Dr. Leyla Soleymani for giving me permission to access her laboratory during phantom making, and to people who work in Dr. Soleymani's laboratory including Jie Yang and Barnabas Fung for their guidances.

Finally, I would like to thank my brother Duy, and my grandfather Thanh for their warm supports through my studies.

This thesis is to honor the memory of my mother (1955-2000), and of my grandmother (1930-2001).

Table of Contents

List of Figures

Chapter 2

Chapter 3

Chapter 4

Chapter 5

Appendix

List of Tables

Chapter 2

Chapter 4

Chapter 5

Chapter 1: Research Motivation, Objective and Contribution

1.1 Research motivation

Glioblastoma multiforme (GBM) is a high grade glioma (HGG) that accounts for nearly 55% of malignant brain tumors, and affects over 12,000 people in the United States per year [1-4]. GBM prognosis is very poor and its median survival is less than 2 years [5-7]. Currently, neurosurgeons define the extent of a GBM resection using brain biopsy combined with preoperative magnetic resonance (MR) images, or intraoperative ultrasound, or intraoperative MR imaging. Unfortunately, these methods suffer low sensitivity and specificity in detecting GBM. **Chapter 2** further discusses the statistical and pathological significance of GBM, and summarizes conventional imaging techniques used to detect GBM as well as their sensitivity and specificity.

Diffuse reflectance spectroscopy (DRS) and fluorescence spectroscopy have been used to detect tissue abnormalities, and are potential techniques to detect brain tumors. DRS and fluorescence spectroscopy are optical techniques that employ a point contact optical probe to measure light (from ultraviolet to near infra-red) intensity as a function of wavelength with high spectral resolution [8]. In early studies, it was shown that DRS alone and fluorescence spectroscopy alone could be used to detect tumors in the breast [9-13], the brain [14-17], the mucosa such as cervix [18,19], colon [20-22] , and the skin [23,24]. In general, diffuse reflectance signal can be modeled to extract tissue optical properties [23,25-27] whereas fluorescence signal can be used to identify the principal fluorophore present in the tissue based on fluorescence characteristics such as emission peaks and

fluorescence life-time [14,15,28,29]. Information on optical properties and fluorescence characteristics of the tissue have diagnostic values because their dynamic changes are bound to tissue neoplastic progression. Background in tissue optics is reviewed in **Chapter 2**.

While many recent studies have combined both DRS and fluorescence spectroscopy to improve accuracy in detecting tumors in human breast [30-35], skin [36-41], oral cavity [42-47] and cervix [48-54], very limited studies have used both techniques to study brain tissues [57-59]. For example, Lin *et al.* were able to identify infiltrating tumor margins from normal brain tissues with a sensitivity of 100% and a specificity of 76% [57], and Toms *et al.* could identify glioma margins with sensitivity of 94% and specificity of 93% [58]. In these studies, separate analyses and observations for GBM and LGG were not available [57,58-61]. In general, intraoperative differentiation of GBM and LGG can be helpful in making treatment plan at the first surgery. For example, a complete removal of tumor is usually curable for LGG whereas a combination of surgery and radiation therapy is usually required for GBM [62]. If brachytherapy is applied, the radioactive seeds can be planted in the tumorous sites at the first surgery [63-64]. In addition, if brachytherapy is required for treatment of both LGG and GBM, radiative seeds with high dose rate (> 30 cGy/hr) are applied to GBM whereas seeds with low dose rate (10 cGy/hr) are applied to LGG [64].

In order to apply the integrated system of fluorescence spectroscopy and DRS to differentiate GBM from LGG during intraoperative procedure, it is necessary to evaluate

and pre-establish the performance of the integrated system during *ex vivo* measurements on LGG and GBM specimens.

1.2 Research objective and contribution

The objective of this thesis is to evaluate the ability of the previously developed integrated system of DRS and fluorescence spectroscopy [65] in identifying GBM during *ex vivo* measurement of brain tissue specimens. The approach relies on the interaction of light with tissue to extract optical properties and fluorescence properties.

The DRS system used in this thesis was previously developed by Derek Cappon [66] whereas the fluorescence spectroscopy system and fitting algorithms to extract fluorescence life-time were previously developed by Zhaojun Nie [67]. Schematic view and clinical set-up can also be found in the Appendix A.2. Both systems were assembled as a single unit of the integrated system by Zhaojun Nie, Derek Cappon and me [65].

The rest of the thesis will be organized in the following structure: **In Chapter 2**, we will briefly introduce the significance of glioma and GBM, their pathological appearances, conventional imaging techniques to detect glioma, and the background on tissue optics. **Chapter 3** to **5** will focus on my research contributions which include (i) developing tissue-simulating optical phantom models to characterize the integrated system (**Chapter 3**), (ii) developing models to recover intrinsic fluorescence spectral shape and intensity (**Chapter 4**), (iii) developing models to extract brain tissue optical properties during *ex vivo* measurement, and optimizing the system's sensitivity and specificity in detecting GBM (**Chapter 5**). In Chapter 3, 4, and 5, I developed the phantom models and experimental

models to recover optical properties, oxygen saturation and fluorescence intensity, and collected and analyzed all spectral data from the brain tissue measurements. Zhaojun Nie helped me with initial system trouble-shooting in Chapter 3. In Chapter 5, brain tissues were cut by Dr. Naresh Murty whereas histological analysis and tumor grading were performed by Dr. John Provias.

Chapter 3 (Paper 1) explores the options to use polystyrene microsphere and Intralipid to simulate scatterers in optical phantom models for calibration of the integrated system. Chapter 3 relies on the direct measurement to estimate scattering properties of Intralipid, applies Mie theory to calculate scattering properties of polymer microspheres, and discusses the benefits of polystyrene microsphere in optical phantoms toward the calibration of the integrated system.

Chapter 4 (Paper 2) introduces a simple experimental method to rapidly retrieve intrinsic fluorescence by using diffuse reflectance signal to compensate the effect of background scattering and absorption. To provide an accurate judgment on the amount of fluorophore present in tissue, a method must be developed to recover the intrinsic fluorescence. Furthermore, Chapter 4 explores the effect of background absorption and scattering on fluorescence spectral intensity.

Chapter 5 (Paper 3) introduces an experimental method to retrieve tissue optical properties and oxygen saturation number. In addition, Chapter 5 includes *ex vivo* measurements of GBM and LGG, and calculates the sensitivity and specificity of the integrated system by accessing optical properties, diffuse reflectance signal and fluorescence signal.

Chapter 6 summarizes and discusses the significances of the dissertation, and presents future work.

References

1. Q. T. Ostrom et al. "American Brain Tumor Association Adolescent and Young Adult Primary Brain and Central Nervous System Tumors Diagnosed in the United States in 2008-2012." Neuro-oncology **18** (1), i1-i50 (2016).

2. J. G. Scott et al., "Aggressive treatment is appropriate for glioblastoma multiforme patients 70 years old or older: a retrospective review of 206 cases, " Neuro-oncology **nor005** (2011).

3. A. Agnihotri et al., "Glioblastoma, a brief review of history, molecular genetics, animal models and novel therapeutic strategies,"Arch. Immunol. Ther. Exp. **61**, 25-41(2013).

4. K. R. Hess et al., "Adult glioma incidence trends in the United States, 1977–2000," Cancer **101** 2293-2299 (2004).

5. Golla H et al. "Glioblastoma multiforme from diagnosis to death: a prospective, hospital-based, cohort, pilot feasibility study of patient reported symptoms and needs," Supportive Care in Cancer **22** 3341-3352 (2014).

6. M. E. Hegi et al., "MGMT gene silencing and benefit from temozolomide in glioblastoma," New England J. Med **352**, 997-1003 (2005).

7. R Stupp et al., "Radiotherapy plus concomitant and adjuvant temozolomide for glioblastoma," New England J. Med. **352** 987-996 (2005).

8. R. Richards-Kortum, and E. Sevick-Muraca. "Quantitative optical spectroscopy for tissue diagnosis." Annual Rev. Physical Chem. **47**, 555-606 (1996).

9. I. J. Bigio et al., “Diagnosis of breast cancer using elastic-scattering spectroscopy: preliminary clinical results,” J. Biomed. Opt. **5**, 221-228 (2000).

10. P. K. Gupta, S. K. Majumder, and A. Uppal, "Breast cancer diagnosis using N2 laser excited autofluorescence spectroscopy," Lasers Surg. Med. **21**, 417–422 (1997).

11. S. Majumder, P. Gupta, B. Jain, and A. Uppal, "UV excited autofluorescence spectroscopy of human breast tissues for discriminating cancerous tissue from benign tumor and normal tissue," Lasers Life Sci. **00**, 1–16 (1998).

12. C. Zhu, G. M. Palmer, T. M. Breslin, J. Harter, and N. Ramanujam, "Diagnosis of breast cancer using diffuse reflectance spectroscopy: comparison of a Monte Carlo

versus partial least squares analysis based feature extraction technique, " Lasers Surg. Med. **38**, 714-724 (2006).

13. G. M. Palmer, C. Zhu, T. M. Breslin, F. Xu, K. W. Gilchrist, and N. Ramanujam, "Monte Carlo-based inverse model for calculating tissue optical properties. Part II: Application to breast cancer diagnosis, "Appl. Opt. **45**, 1072–1078 (2006).

14. L. Marcu et al., "Fluorescence lifetime spectroscopy of glioblastoma multiforme." Photochem. Photobiol. **80**, 98-10 (2004).

15. P. V. Butte et al., "Diagnosis of meningioma by time-resolved fluorescence spectroscopy." J. Biomed. Opt. **10**, 064026-0640266 (2005).

16. A. C. Croce et al. "Diagnostic potential of autofluorescence for an assisted intraoperative delineation of glioblastoma resection margins." Photochem. Photobiol. **77**, 309-318 (2003).

17. W. C. Lin et al., "Diffuse reflectance spectroscopy for in vivo pediatric brain tumor detection," J. Biomed. Opt. **15**, 061709-061709 (2010).

18. S. K. Chang, N. Marin, M. Follen, and R. Richards-Kortum, "Model-based analysis of clinical fluorescence spectroscopy for in vivo detection of cervical intraepithelial dysplasia," J. Biomed. Opt. **11**, 024008-024008 (2006).

19. Y. N. Mirabal et al. "Reflectance spectroscopy for in vivo detection of cervical precancer." J. Biomed. Opt. **7**, 587-59 (2002)

20. G. Zonios, L. T. Perelman, V. Backman, R. Manoharan, M. Fitzmaurice, J. V. Dam, and M. S. Feld, "Diffuse reflectance spectroscopy of human adenomatous colon polyps in vivo," Appl. Opt. **38**, 6628 (1999).

21. G. Bottiroli et al. "Natural fluorescence of normal and neoplastic human colon: a comprehensive “ex vivo” study." Lasers Surg. Med. **16**, 48-60 (1995):

22. H. W. Wang et al. "Diffuse reflectance spectroscopy detects increased hemoglobin concentration and decreased oxygenation during colon carcinogenesis from normal to malignant tumors." Optics Express **17**, 2805-2817 (2009).

23. G. Zonios, J. Bykowski, and N. Kollias, "Skin melanin, hemoglobin, and light scattering properties can be quantitatively assessed in vivo using diffuse reflectance spectroscopy." J. Investi. Derma. **117**, 1452-1457 (2001).

24. R. Marbach, and H. M. Heise, "Optical diffuse reflectance accessory for measurements of skin tissue by near-infrared spectroscopy." Appl. Opt. **34**, 610-621 (1995).

25. T. J. Farrell, B. C. Wilson, and M. S. Patterson. "The use of a neural network to determine tissue optical properties from spatially resolved diffuse reflectance measurements." Phys. Med. Biol. **3**, 2281 (1992).

26. T. J. Farrell, M. S. Patterson, and B. Wilson, "A diffusion theory model of spatially resolved, steady-state diffuse reflectance for the noninvasive determination of tissue optical properties in vivo," Medical Physics **19**, 879-888 (1992).

27. T. J. Pfefer et al. "Reflectance-based determination of optical properties in highly attenuating tissue." J. Biomed. Opt. **8**, 206-215 (2003).

28. R. Drezek, K. Sokolov, U. Utzinger, I. Boiko, A. Malpica, M. Follen, R. Richards-Kortstum, "Understanding the contributions of NADH and collagen to cervical tissue fluorescence spectra: modeling, measurements, and implications." J. Biomed. Opt. **6**(4), 385-396 (2001).

29. S. K. Chang, D. Arifler, R. Drezek, M. Follen, and R. Richards-Kortum, "Analytical model to describe fluorescence spectra of normal and preneoplastic epithelial tissue: comparison with Monte Carlo simulations and clinical measurements." J. Biomed. Opt. **9**(3), 511-522 (2004).

30. C. Zhu, et al. "Diagnosis of breast cancer using fluorescence and diffuse reflectance spectroscopy: a Monte-Carlo-model-based approach." J. Biomed. Opt **13**, 034015-034015 (2008).

31. T. M. Breslin et al. "Autofluorescence and diffuse reflectance properties of malignant and benign breast tissues, "Annals Surg. Oncol. **11**, 65–70 (2004).

32. G. M. Palmer, and N. Ramanujam. "Diagnosis of breast cancer using optical spectroscopy." Medical Laser Application **18**, 233-248 (2003).

33. Z. Volynskaya et al., "Diagnosing breast cancer using diffuse reflectance spectroscopy and intrinsic fluorescence spectroscopy." J. Biomed. Opt. **13**, 024012-024012 (2008).

34. M. D. Keller al. "Autofluorescence and diffuse reflectance spectroscopy and spectral imaging for breast surgical margin analysis." Lasers Surg. Med. **42**, 15-23 (2010).

35. V. Sharma et al. "Auto-fluorescence lifetime and light reflectance spectroscopy for breast cancer diagnosis: potential tools for intraoperative margin detection." Biomed. Optics Express **3**, 1825-1840 (2012).

36. N. Rajaram et al. "Pilot clinical study for quantitative spectral diagnosis of non-melanoma skin cancer." Lasers Surg. Med. **42**, 876-887 (2010).

37. N. Rajaram et al. "Design and validation of a clinical instrument for spectral diagnosis of cutaneous malignancy." Appl. Opt. **49**, 142-152 (2010).

38. W. C. Vogt et al. "Effects of mechanical indentation on diffuse reflectance spectra, light transmission, and intrinsic optical properties in ex vivo porcine skin." Lasers Surg. Med. **44**, 303-309 (2012).

39. A. J. Thompson et al. "In vivo measurements of diffuse reflectance and time-resolved autofluorescence emission spectra of basal cell carcinomas." J. Biophotonics **5**, 240-254 (2012).

40. G. J. Greening et al. "Fiber-bundle microendoscopy with sub-diffuse reflectance spectroscopy and intensity mapping for multimodal optical biopsy of stratified epithelium." Biomed. Optics Express **6**, 4934-4950 (2015).

41. L. Lim et al. "Clinical study of noninvasive in vivo melanoma and nonmelanoma skin cancers using multimodal spectral diagnosis." J. Biomed. Opt. **19**, 117003-117003 (2014).

42. D. C. G. De Veld et al. "Autofluorescence and diffuse reflectance spectroscopy for oral oncology." Lasers Surg. Med. **36**, 356-364 (2005).

43. R. A. Schwarz, et al. "Autofluorescence and diffuse reflectance spectroscopy of oral epithelial tissue using a depth-sensitive fiber-optic probe." Appl. Optics **47**, 825-834 (2008).

44. J. L. Jayanthi et al. "Comparative evaluation of the diagnostic performance of autofluorescence and diffuse reflectance in oral cancer detection: a clinical study." J. Biophotonics **4**, 696-706 (2011).

45. M. S. McGee et al. "Anatomy-based algorithms for detecting oral cancer using reflectance and fluorescence spectroscopy." Annals of Otology, Rhinology & Laryngology **119**, 817-826 (2010).

46. L. Sweeny et al. "Assessment of tissue autofluorescence and reflectance for oral cavity cancer screening." Otolaryngology--Head and Neck Surgery **145**, 956-960 (2011).

47. R. J. Mallia et al. "Diffuse reflection spectroscopy: an alternative to autofluorescence spectroscopy in tongue cancer detection." Applied Spectroscopy **64**, 409-418 (2010).

48. R. J. Nordstrom et al. "Identification of cervical intraepithelial neoplasia (CIN) using UV-excited fluorescence and diffuse-reflectance tissue spectroscopy." Lasers Surg. Med. 29, 118-127 (2001)

49. S. K. Chang, et al. "Combined reflectance and fluorescence spectroscopy for in vivo detection of cervical pre-cancer." J. Biomed. Opt. **10** 024031-02403111 (2005).

50. Chidananda, Siddappa M., et al. "Optical diagnosis of cervical cancer by fluorescence spectroscopy technique." International Journal of Cancer **119**, 139-145 (2006).

51. J. A. Freeberg et al. "Fluorescence and reflectance device variability throughout the progression of a phase II clinical trial to detect and screen for cervical neoplasia using a fiber optic probe." J. Biomed. Opt. **12**, 034015-034015 (2007).

52. A. J. Freeberg et al. "The performance of fluorescence and reflectance spectroscopy for the in vivo diagnosis of cervical neoplasia; point probe versus multispectral approaches." Gynecologic Oncology 107, S248-S255 (2007).

53. Alvarez, Ronald D., Thomas C. Wright, and Optical Detection Group. "Effective cervical neoplasia detection with a novel optical detection system: a randomized trial." Gynecologic Oncology 104, 281-289 (2007).

54. C. R. Weber et al. "Model-based analysis of reflectance and fluorescence spectra for in vivo detection of cervical dysplasia and cancer." J. Biomed. Opt. **13**, 064016-064016 (2008).

55. P. V. Butte et al., "Intraoperative delineation of primary brain tumors using time-resolved fluorescence spectroscopy," J. Biomed. Opt **15**(2), 027008-027008 (2010).

56. P. V. Butte et al., "Fluorescence lifetime spectroscopy for guided therapy of brain tumors," Neuroimage **54**, S125-S135 (2011).

57. W. C. Lin et al., "In vivo brain tumor demarcation using optical spectroscopy," Photochem. Photobiol. **73**(4), 396-402 (2001).

58. S. A. Toms et al., "Intraoperative optical spectroscopy identifies infiltrating glioma margins with high sensitivity." Neurosurgery **57**, 382-3914 (2005).

59. P. A. Valdés et al., "Combined fluorescence and reflectance spectroscopy for in vivo quantification of cancer biomarkers in low-and high-grade glioma surgery." J. Biomed. Opt. **16**, 116007-11600714 (2011).

60. W. Stummer et al., "Fluorescence-guided surgery with 5-aminolevulinic acid for resection of malignant glioma: a randomised controlled multicentre phase III trial," Lancet Oncol. **7**(5), 392–401 (2006).

61. W. Stummer, et al. "Extent of resection and survival in glioblastoma multiforme: identification of and adjustment for bias." Neurosurgery **62**(3), 564-576 (2008).

62. S. A. Grossman, and J. F. Batara. "Current management of glioblastoma multiforme." Seminars in oncology. Vol. 31. No. 5. WB Saunders, 2004.

63. E. Barbarite, et al. "The role of brachytherapy in the treatment of glioblastoma multiforme." Neurosurgical review (2016): 1-17.

64. S. B. Schwarz, et al. "Iodine-125 brachytherapy for brain tumours-a review." Radiation Oncology 7.1 (2012): 1.

65. Z. Nie, V. N. Du Le, D. Cappon et al. "Integrated Time-resolved Fluorescence and Diffuse Reflectance Spectroscopy Instrument for Intraoperative Detection of Brain Tumor Margin," J. Selected Topic in Quantum Electronics, IEEE **22**(3), 6802109 (2016).

66. D. J. Cappon et al., "A Novel Fibre Optic Probe Design and Optical Property Recovery Algorithm for Optical Biopsy of Brain Tissue, " J. Biomed. Opt. **18**(10),107004 (2013)

67. Z. Nie et al. "Hyperspectral fluorescence lifetime imaging for optical biopsy," J. Biomed. Opt. **18** (9), 096001 (2013).

Chapter 2: Background Introduction

2.1 The brain, glioma and glioblastoma multiforme

2.1.1 The brain

The brain is the human body's control center which controls movement, speech, emotions, consciousness and internal body functions, such as heart rate, breathing and body temperature [1]. As shown in Fig. 2.1, the macroscopic level of the brain has three main parts: cerebrum, cerebellum, and brain stem [1]. At microscopic level, the brain is made of two main cell types - neurons and glia (glial cells) [1]. The cerebrum is the largest part of the brain, followed by the cerebellum and brain stem. The outer surface of the cerebrum is called the cerebral cortex or grey matter, the inner surface of the cerebrum is called white matter. The grey matter consists of glial cells, synapses, capillary, numerous neuronal cell bodies, and relatively few myelinated axons while white matter contains relatively very few cell bodies and is composed mainly of long-range myelinated axon tracts [1]. The dominated lipid content of myelin in white matter is responsible for the bright appearance in white matter [2-4].

The cerebrum can be sub-divided into frontal, parietal, temporal and occipital lobe. The frontal lobe controls movement, speech, memory, emotions, intellectual functioning. The parental lobe controls sensation and special orientation. The temporal lobe controls hearing and the occipital lobe control vision. The cerebellum is located under the cerebrum and is responsible for movement, postures, walking, talking. Similar to the cerebrum, the cerebellum has grey matter on the outer surface and white matter on inner area. The brain

stem is located at the base of the brain, and is responsible for connecting the cerebrum to the spinal cord and sending messages between different parts of the body and the brain.

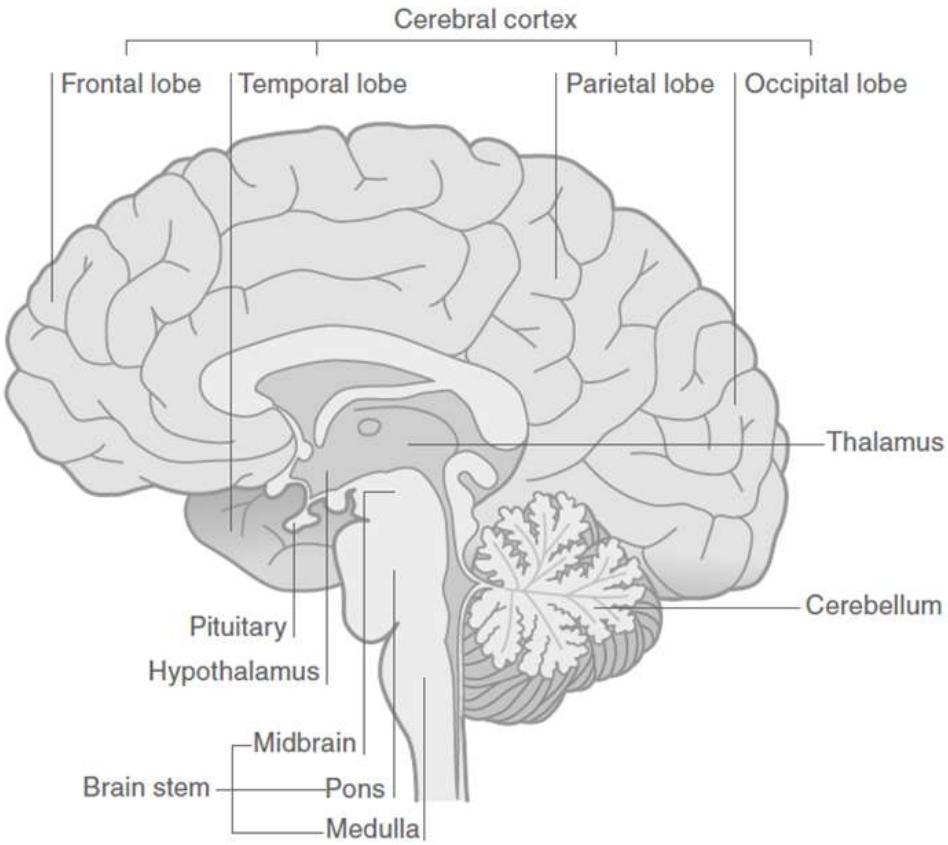

Fig. 2.1 Basic macroscopic anatomy of the human brain. Reprinted ref [1]. Copyright © 2014, Springer-Verlag Wien. Reprinted with permission.

2.1.2 Brain tumors statistics

Brain tumors can start in the brain (primary brain tumors) or can spread into the brain from a cancer at other organs (secondary brain tumors). Primary brain tumors (PBTs) are generally more invasive than secondary brain tumors, and will be discussed here. PBTs have the average age-adjusted annual incidence rate of about 22 per 100,000 population [5], and are responsible for nearly 16,000 deaths per year in the United States [6]. PBT incidence rate is about 5.6 per 100,000 population for age group of 0-19, and about 29 per 100,000 population for age group of 20 and above.

In general, malignant PBTs are more common in males than in female with ratio of 11:9 while non-malignant PBTs are more common in females than males with ratio of 16:9. For males in the U.S., the risk of developing a malignant PBT is about 0.69%, and the risk of dying from a malignant PBT is about 0.51%. These numbers are 0.55% and 0.41% for females. Five-year survival rate in the U.S. is approximately 31.7% for males and 34.4% for females [5].

2.1.3 Glioma and glial cells

Glioma - tumor starting in glial cells, is the most common PBT (30%) (Fig. 2.2), and accounts for nearly 80% all malignant PBTs (Fig. 2.3) [5]. Although glioma can occur outside the brain (i.e. spinal cord), majority of glioma occurs inside the brain. More specifically, there is 19.8% chance glioma occurs in the temporal lobe, 25.9% in frontal lobe, 12% in parietal lobe, and 3.1% in the occipital lobe of the brain (Fig. 2.4). According to WHO classification, the three main types of glioma are oligodendrocytoma, astrocytoma,

ependymona which starts in oligodendrocytes, astrocytes, and ependymal cells, respectively [7,8]. Glial cells are more numerous than neural cells in the brain, and occupy about half of the brain's volume. In general, glial cells control microenvironment of the brain, maintain an appropriate amount of ions, and regulate the formation of myelin shealths around axons [9-11]. Furthermore, astrocytes can control the brain-blood barrier that protect the CNS from unwanted substances whereas oligodendrocytes can form electrical insulation around nerve fibres and ependymal cells regulate the production of cerebrospinal fluid. Glial cells are generally smaller than neural cells, and lack of axons and dendrites [9-11].

Although tumor invasion is the key feature of glioma, the degree of invasion is variable [12]. For example, about 30% of high grade gliomas (HGG) have limited invasion, infiltrating cells less than 1 cm from the edge of gross tumor whereas about 20% of HGG have more extensive invasion, infiltrating cells more than 3 cm from the edge of gross tumor. At the presence, HGGs cannot be separated based on their extension of invasion, and must be treated the same way by combining maximal removal, chemotherapy and radiotherapy [12]. It has been showed that conventional brain imaging techniques such as computed tomography and magnetic resonance imaging have failed to improve the identification of glioma margins [13-16].

Histological analysis enables brain tumor grading so that low grades are WHO grade II, and high grades are WHO grade III and IV [7,8]. The grading is determined by the level of nuclear atypia, mitosis, microvessel proliferation, and necrosis. Among all gliomas, astrocytoma is the most common glioma, responsible for 76% of all gliomas while

glioblastoma multiform (GBM), a grade IV of astrocytoma, is the most malignant form of glioma with a median survival of less than 2 years, and accounts for nearly 55% all malignant PBTs [5,17]. GBM has the highest incidence among all malignant PBTs, approximately 3.2 per 100,000 population [5]. In the United States, there are about 12,000 patients were diagnosed with GBM per year. GBM is more common in male than female (ratio 3:2), and usually occurs in individuals at 60 years of age (90% of cases) [18,19].

Currently, GBM has the lowest survival rate among all malignant brain tumors, approximately 37.2% for first year, 15.2% for second year, 8.8% for third year and 6.3% for fourth year. Whereas its median survival is less than 2 years for a complete resection [17], the mean survival time is in the range of 6-9 months for an incomplete surgical resection [20].

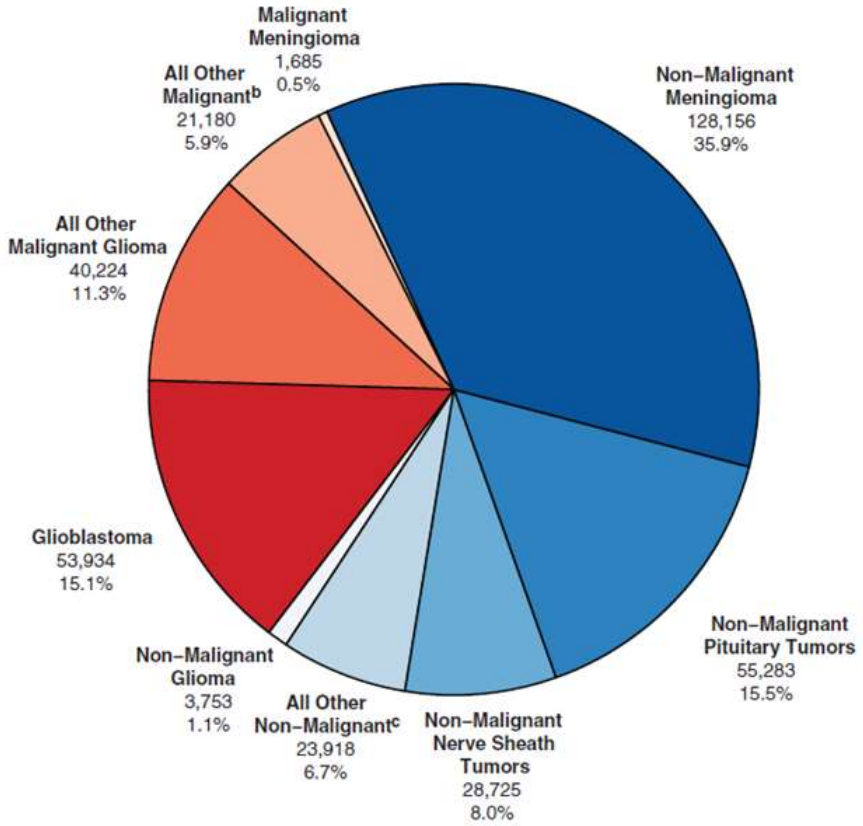

Fig. 2.2 Distribution of primary brain and CNS tumors. Reprinted from ref [5]. Glioblastoma is grade IV astrocytoma, which is one of the gliomas.

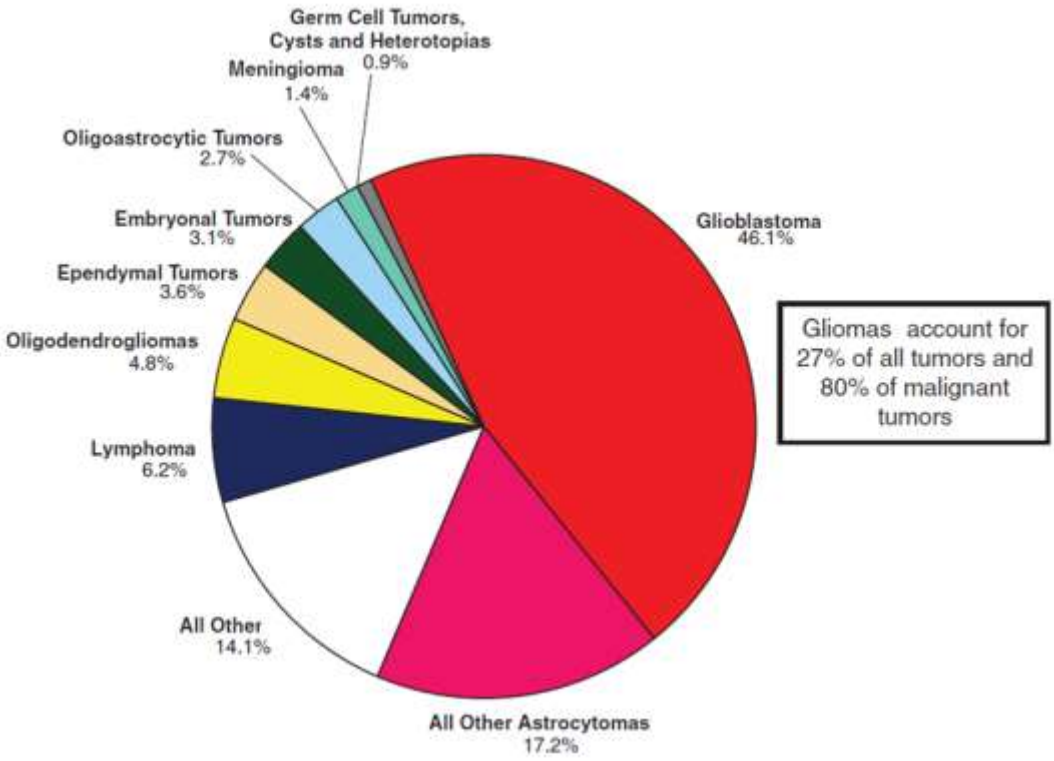

Fig. 2.3 Distribution of malignant primary brain and CNS tumors. Reprinted from ref [5]. Copyright © Oxford University Press 2015. Reprinted with permission.

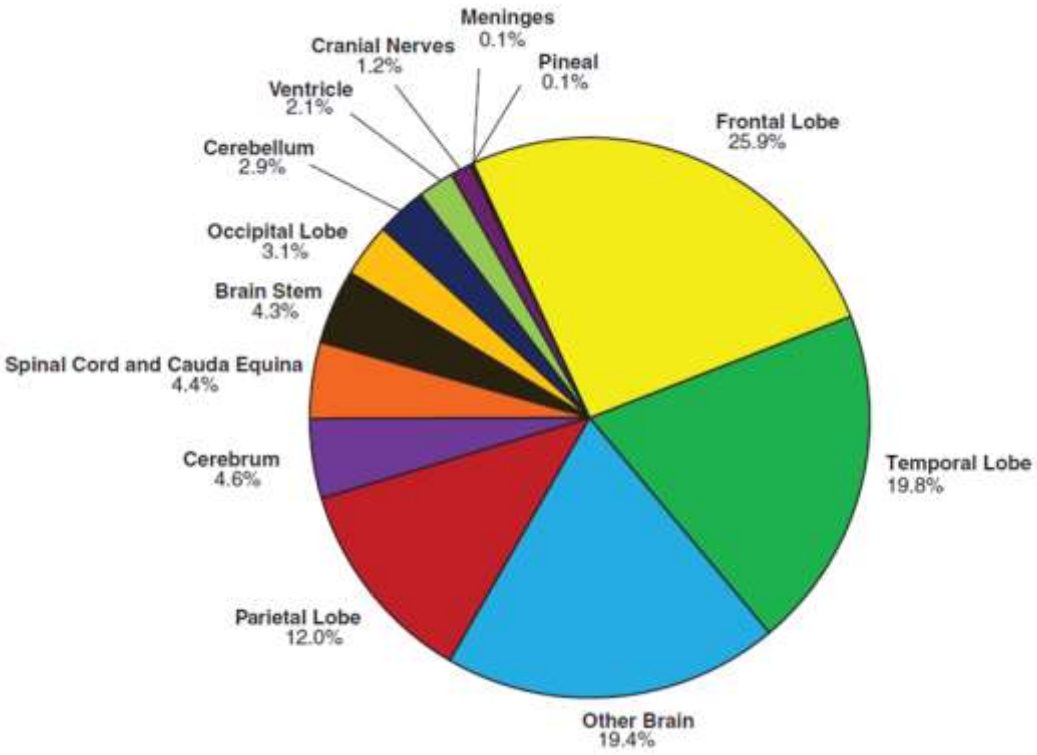

Fig. 2.4 Distribution of primary brain and CNS gliomas. Reprinted from ref [5]. Copyright © Oxford University Press 2015. Reprinted with permission.

2.1.4 Astrocytoma: Types and histopathology

Due to the common occurrence of astrocytoma among all gliomas (76%), astrocytoma is the principal target of current study, and its progression and histopathology is the topic of discussion here. Astrocytoma can be subdivided into four groups: pilocytic astrocytoma (WHO grade I), low-grade astrocytoma (WHO grade II), anaplastic astrocystoma (WHO grade III), and GBM (WHO grade IV) [18-20]. Grade III and IV are considered as high grade. Pilocytic astrocytoma (PA) is believed to be benign, and does not evolve into more malignant tumors. A complete surgical excision is considered curative for PA patients. PA

is commonly diagnosed in children with peak at age between 8 and 13 years [20]. Histologically, PA is characterized by bipolar, fusiform, or “piloid cells with dense fibrillation. The word pilocytic refers to the fiber-like appearance of the tumor cells [Fig. 2.5(a)]. Low grade astrocytoma (LGA) affects young adults with peak at age between 30 and 40 years. Histologically, the LGA cells can be stellate, spindle-shaped with fiber like processes, or plump with a large cytoplasmic mass, and can form microcysts [Fig. 2.5(b)]. If left untreated, LGA can progress into anaplastic astrocytoma which has an increase of cellularity. Anaplastic astrocytoma is characterized by mitotic activity which is absent in LGA. Anaplastic astrocytoma rapidly progresses into GBM.

GBM has a wide range of histological appearances, and can consist of different cell types such as those with round and oval shape [Fig. 2.6 (a)], or those with pleomorphic shape [Fig. 2.6(b)], or those with “giant” size [Fig. 2.6(c)] [21]. In addition, necrosis is an essential characteristics for histological identification of GBM [Fig. 2.5(c)] [20]. Necrosis may occur in more than 80% of GBM mass due to the insufficient blood supply. In addition, microvasculature proliferation (angiogenesis) is often observed in GBM because GBM cells can contribute significantly to the blood vessels supporting tumor growth by differentiating into functional vascular endothelium [22,23].

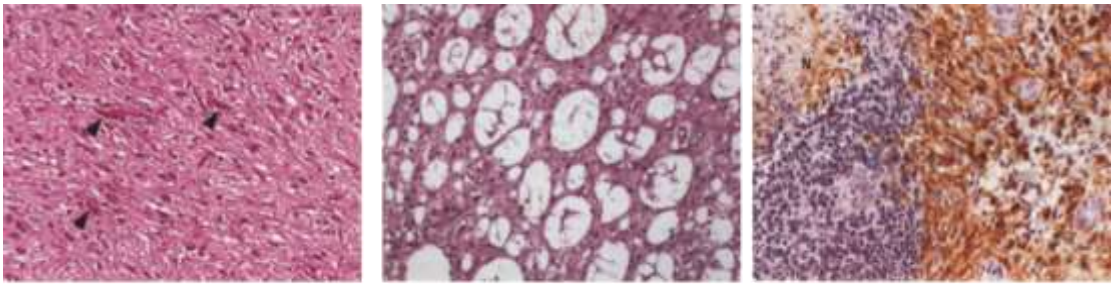

Fig. 2.5 The hematoxylin and eosin (H&E) stained section of (a) cerebellar pilocytic astrocytoma in a 7-year-old boy, (b) low grade astrocytoma in left frontal lobe of a 26 year old man, (c) GBM in the hypothalamus of a 57-year-old woman. In (a), image shows a tumor of low cellularity, forming a dense fibrillary matrix (arrows). In (b), image shows a fibrillary astrocytoma with low cellularity and numerous retention cysts. In (c), image shows a glioblastoma with focal necrosis (N). Reprinted from ref [20]. Copyright © 1995 Wiley-Liss, Inc. Reprinted with permission.

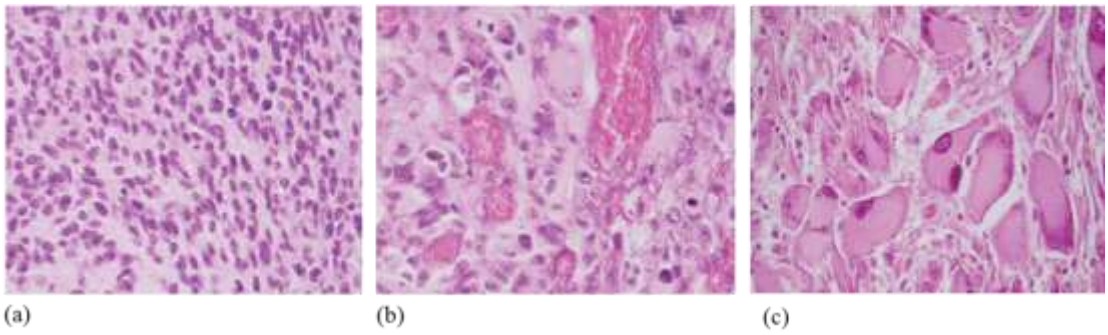

Fig. 2.6 Some examples of GBM histological appearances with H&E stain: (a) small homogeneous cells with high cellularity and high mitotic activities showing scant cytoplasm with round to oval nuclei; (b) pleomorphic shaped cells with bizarre nuclei. The term “pleomorphic" designation indicates that the tumor displays significant variety of cellular and nuclear size/shape; (c) multinucleated giant cells. Reprinted from ref [21]. Copyright © 2006, Copyright © 2006 by the American Association of Neuropathologists, Inc. Reprinted with permission

2.2 Conventional methods for intraoperative diagnostics of gliomas

2.2.1 Biopsy and preoperative magnetic resonance imaging (MRI)

When a brain tumor is suspected during neurological evaluation (i.e. mental status), magnetic resonance imaging (MRI) scans or computed tomography (CT) scans are used to identify the mass [18,19]. If a tumor is detected, a biopsy is usually done. Biopsy is the surgical removal of small amount of tumor tissues for pathological analysis [18,19,24]. There are two types of biopsy: stereotactic biopsy and open biopsy. Stereotactic biopsy involves the removal small incision of the scalp and the drill of small hole to insert the needle to remove the tissues. Open biopsy involves the removal of portion of the skull through a procedure called craniotomy. Whereas open biopsy is applied for patients with superficial lesions that can be accessed via a small craniotomy, stereotactic biopsy is reserved for patients with deeper lesions.

In either cases, a sample of the suspected tumor is removed, and analyzed by the pathologist in order to establish the tumor phenotype for treatment plan. Preoperative MRI with high field strength (1.5-3 Tesla) has been used as a standard guidance tool in neurosurgery [25-27]. However, the shift of the brain and cerebrospinal fluid during surgical procedure can lead to inaccurate registrations between the image spaces with the actual tissue space, resulting in navigation on the wrong track which could cause low sensitivity and specificity in brain tumor diagnosis [28,29]. It has been shown that during neurosurgery, the cortical surface can displace up to 1 cm while the brain tissue surface can shift up to 5 cm [30-32]. FitzGerald *et al.* demonstrated that preoperative MRI might have

sensitivity of 81% and specificity of 53% when brain tumor margin error was 10 mm [33], and of 92% and 0%, respectively when margin error was 20 mm [33]. Similarly, Pauleit *et al.* reported a high sensitivity (96%) and low specificity (53%) in differentiating 26 glioma residues from 26 normal tissues [34]. Therefore, intraoperative imaging methods are crucial for real-time tumor resection during neurosurgery.

2.2.2 Intraoperative MRI

Intraoperative MRI with contrast enhancement has been used to determine the extent of tumor removal by visualizing the accumulation of contrast medium at the tumor border. Recent studies have adapted high field strength intraoperative MRI (iMRI) scanner for operating room usage, and showed that, iMRI could improve the extent of brain tumor resection up to 60% [35], increase the number of patients having complete tumor resection by 40% [36], and achieve moderate specificity (75%) with low sensitivity (55%) in detecting residual tumor in patients harboring a GBM [37]. The main disadvantage of iMRI is that it lengthens the anesthesia and surgical time [38]. Specifically, iMRI neurosurgical procedure requires an additional of 1.6-2 surgical hours due to scanning, imaging transfer and interpretation. Furthermore, iMRI limits the surgical space due to its bulky coil, requires compatible surgical tools for high magnetic field, and increases installation cost for independent operating and scanning sites [40,41]. The cost of a surgical suite with a MRI machine can be within US$3-8 million [36,38].

2.2.3 Intraoperative ultrasound

Cost effective intraoperative ultrasound was first introduced to neurosurgery in 1982 to localize cystic and solid brain tumors, to assist guiding needle during stereotactic biopsy [42]. It was later applied to detect brain shift, and to define brain tumor margins [43-45]. The possibility of using ultrasound as an intraoperative imaging technique has been controversial because the plane of ultrasound imaging is restricted to the available bone window, limiting the scanning area and causing information loss [46]. Recent studies has evaluated the significance of intraoperative ultrasound in accessing the resection degree of brain glioma. For example, Yu *et al.* used an ultrasonic scanner at probing frequency of 3-5 MHz to differentiate 87 glioma tumor residues from 273 samples without residues [47]. Although the technique achieved high specificity (92.8%), it suffered low sensitivity (62.8%) [47]. Coburger *et al.* showed that using a linear array intraoperative ultrasound could achieve a specificity of 75% and sensitivity of 76% in differentiating 52 glioma samples from 16 normal brain samples [37]. Furthermore, it was shown that although GBM was well delineated with ultrasound prior to resection, there was a significant drop of accuracy during resection due to the contribution of cavity wall, debris, air bubble and blood to ultrasound artifacts [48]. More specifically, sensitivity and specificity was both 95% before resection, and was 26% and 88%, respectively after resection [48]. These studies indicated that intraoperative ultrasound might not improve the accuracy of brain tumor detection that was established with preoperative MRI.

2.3.4 Contrast enhanced fluorescence imaging

The use of 5-aminolevulinic acid (5-ALA) contrast enhanced fluorescence imaging is one of the most advanced imaging techniques for surgical resection of malignant brain tumor [49]. In principal, oral administration of 5-ALA can cause over-production of a fluorophore called protoporphyrin IX (PpIX) in malignant tumor cells [50]. On the other hand, in non-cancerous cells, exogenous application of 5-ALA results in the production of PpIX which is rapidly metabolized to non-fluorescent heme. Because PpIX strongly absorbs blue light (at wavelength of 400 nm) and emits red light (at wavelength of 640 nm), optical techniques for detection of PpIX's fluorescence signal have diagnostic values. Roberts *et al.* showed that although 5-ALA fluorescence-guided surgery can achieve a sensitivity of 75% and a specificity of 71% in differentiating glioma, the method suffers high false negative rate (74%) because of the absence of fluorescence signal in necrotic tumor area [51].

Therefore, it is crucial to develop a more accurate and more cost effective imaging method for tumor detection during intraoperative neurosurgery. Table 2.1 summarizes sensitivity and specificity of conventional imaging techniques for diagnostics of glioma brain tumor.

Table 2.1 Sensitivity and specificity of conventional imaging techniques for diagnostics of gliomas

Methods	Sampling	Systems	Sensitivity	Specificity
Preoperative MRI				
			(margin error of 10 mm)	
FitzGerald *et al* , 1997	11 patients: 8 brain tumors, 1 benign cyst, 1 epilepsy, and 1 cavernous angioma	1.5-T MRI scanner (Signa), T1-weighted images	81%	53%
			(margin error of 20 mm)	
			92%	0%
Pauleit *et al* , 2005	28 glioma suspected cases; 52 biopsy samples: 26 glioma residues, 26 without residues	1.5-T MRI scanner (Sonata), T1-weighted image	96%	53%
Intraoperative MRI				
Coburger *et al* , 2015	20 glioma cases; 68 biosy samples: 52 glioma residues, 16 without residues	1.5-T iMRI (Magnetom Espree), T1-weighted image	55%	75%
Intraoperative ultrasound				
Yu et *al* , 2015	120 glioma suspected cases; 340 biopsy samples: 87 with glioma tumor residues, 273 without residues	colour US scanner (Aloka), small convex array probe at 3-6 MHz	93%	63%
Coburger *et al* , 2015	20 glioma cases; 68 biosy samples: 52 glioma residues, 16 without residues	linear array US, probed at 7-15 MHz	76%	75%
		conventional US (Philip), probed at 2-7 MHz	24%	96%
			(during resection)	
Ry *et al* , 2008	19 GBM patients; 186 biopsy samples (10 frozen)	SonoWand US, probed at 5 MHz	87%	42%
			(after resection)	
			26%	88%
Intraoperative protoporphyrin IX fluorescence				
Roberts *et al* , 2011	11 GBM patients, 124 biopsy specimens: 86 red fluoresence and 38 non-fluoresence	surgical microscope (Carl Zeiss Surgical GmbH) with excitation at 400 nm, bandpass filter (620–710 nm)	75%	71%

2.3 Overview of tissue optics

2.3.1 Basic interaction of light with tissues

Upon incidence with tissue surface, light can be either absorbed or not. The light that is not absorbed, can either return back to the source (remission) or is transmitted through or out of the tissue (transmission). Within the tissue, light can either travel straight or change its direction via interaction with the scatterers present in tissues (through scattering process). If the light is absorbed in the tissue (through absorption process), the absorbed energy can be re-emitted as light (emission process) or can be converted into heat. The interaction of light with tissue is determined by the properties of light source (i.e. wavelength, power), tissue optical properties (i.e. absorption and scattering coefficients), and tissue fluorescence properties (i.e. emission peaks and fluorescence life-time) [52,53].

2.3.1.1 Remission and diffuse reflection

Remission is the process in which light is reflected from the tissue surface or is scattered within the tissue, leaving tissue and propagating toward the source. For example, if we consider a laser beam being delivered to tissue surface from air [Fig. 2.7(a)], according to Fresnel's law, a portion of laser beam will be reflected at the surface due to the difference in index of refraction, n, between air (n =1) and tissue ($n \approx 1.33$) [52]. The amount of reflected light depends on the incident angle and the difference between the two refractive indices [Fig. 2.7(b)]. The dependence of specular reflection (R_s) on incidence angle and refraction angle can be described by Fresnel's law (Eq.2.1).

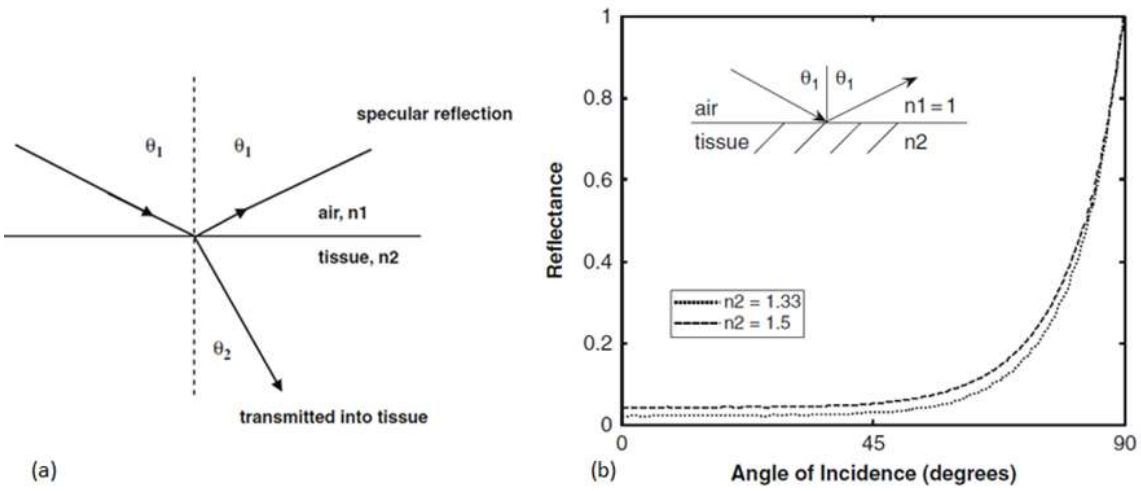

Fig. 2.7 (a) A ray of light incident on an interface between air with refractive index n_1 and tissue with refractive index n_2, (b) Specular reflection of a ray of light using Eq. (1.1) for non-polarized light considering $n_2 = 1.33$ and 1.5. Note that the angle of incidence (θ_1) is related to the angle of refraction (θ_2) by the index of refraction in Snell's law ($n_1 \sin\theta_1 = n_2 \sin\theta_2$). Reprinted from ref [52]. Copyright © 2010, Springer Science and Business Media B.V. Reprinted with permission.

$$R_s(\theta_1) = \frac{1}{2}\left[\frac{\tan^2(\theta_1-\theta_2)}{\tan^2(\theta_1+\theta_2)} + \frac{\sin^2(\theta_1-\theta_2)}{\sin^2(\theta_1+\theta_2)}\right] \qquad (2.1)$$

When the surface is flat, all the reflected light leaves the surface at the same angle, in the same direction and the process is called specular reflectance [Fig. 2.8(a)]. In reality, tissue surface is not optically flat but is rough, causing variation in the angle of incidences and in the intensity reflected light across tissue surface. The process in which the reflected light leaves the surface in various directions is called diffuse reflectance [Fig. 2.2(b)]. In addition to reflectance at the surface, the portion of light propagating within the tissue can

be scattered (scattering process), and then propagates back to the surface to be detected by the detector.

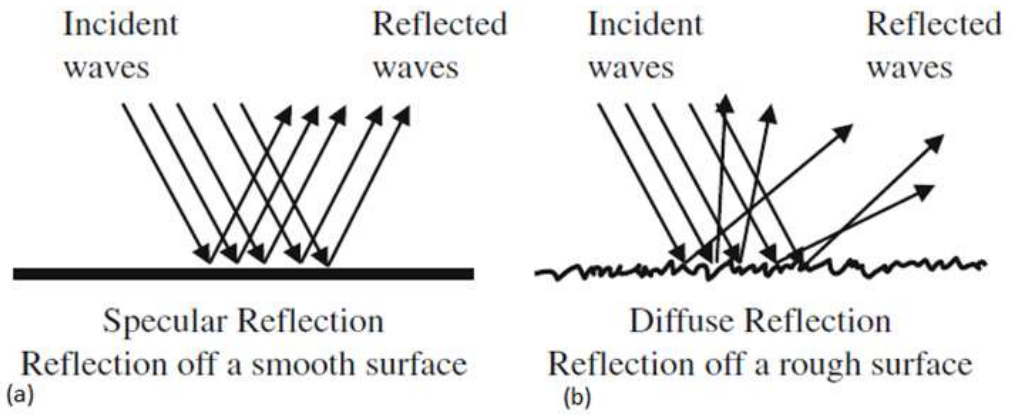

Fig. 2.8 (a) Specular reflection occurs when light reflects off an optically smooth surface, (b) Diffuse reflection occurs when light reflects off an optically rough surface. Reprinted from ref [53]. Copyright © 2010, Springer Science and Business Media B.V. Reprinted with permission.

2.3.1.2 Scattering

Scattering is the process in which the propagation light change its direction upon interaction with tissue. There are two types of scattering: elastic scattering and inelastic scattering [53]. In elastic scattering, the wavelength of light does not change during the scattering process. In inelastic scattering (Raman scattering), there is a change in wavelength of light due to the transfer of the small amount of photon energy to molecules in tissue, leading to the excitation of molecules. The spatial fluctuation of refractive index within tissue is responsible for scattering of light in tissue. If the spatial fluctuation occurs on a scale smaller than wavelength of light (size of particle is smaller than wavelength), the

scattering process is called Rayleigh scattering. If the spatial fluctuation occurs on a scale larger than wavelength of light (size of particle is larger than wavelength), the scattering process is called Mie scattering. Mie scattering and Rayleigh scattering (both are elastic scattering) are the two primary forms of scattering in biological tissues [54]. Although Mie scattering theory applies to spherical particles, studies have been successfully utilizing Mie theory to model light scattering in biological tissues such as brain, muscle and colon tissue [55,56]. Furthermore, Mie theory has been widely used to control scattering properties of polystyrene microsphere in standard optical phantoms [57].

Because scattering arises from the refractive index mismatch, organelles with different refractive indices from their surrounding are major sources of scattering [58]. Although cells may be viewed as sources of small angle scatterers in flow cytometry where cells can be measured individually, the cell as an entity is not as important for *in vivo* scattering diagnostics because it is always surrounded by other cells or tissues of similar refractive index within the extremes of water (n = 1.33) and fat (n = 1.45) [59-61]. Potential organelles functioning as major source of scatterer are mitochondria, lysosome and peroxisome. Diameter of these organelles ranges from 0.5 μm to 1.5 μm. Nucleus is another significant source of scatterer because it is the largest organelles in the cells, and nucleus size can change significantly during neoplastic progression [58-61].

2.3.1.3 Absorption, fluorescence and heating

Upon absorbing light, the absorbing molecules within the tissue can transition from ground state to an excited state, and Jablonski diagram can be used to depict such transitions

(Fig. 2.9) [53]. In Fig. 2.9, the ground, first, second, and third electronic state is depicted as S_0, S_1, S_2, S_3, respectively. Electrons can exist in one of the two states: the singlet state or the triplet state. Singlet spin refers to spin with multiplicity, (2S+1), of 1. *S* is number of electrons multiplying with the spin quantum number which could be +1/2 (spin up) or -1/2 (spin down). A pair of electron usually has opposite spins so that multiplicity is [2(+1/2 + (-1/2)) + 1] = 1 (singlet). When the electrons are both up, then the spin multiplicity is [2(+1/2++1/2) +1] = 3 (triplet).

Molecules at excited state rapidly relax to lower state through a process called internal conversion, which can occur with or without the emission of light. When an internal conversion occurs with the emission of light, then the process of emission is termed fluorescence. Fluorescence can be defined as the singlet-singlet radiative transition between the first excited state (S_1) and the ground state (S_0). Although other type of transition in fluorescence process might occur such as that from S_2 state to S_0 state in free radicals, fluorescence in S_1-S_0 transition is the far most common type in tissue optics. Furthermore, internal conversion usually completes prior to fluorescence because internal conversion generally occurs within 10^{-12} second or less while fluorescence life-time is typically near 10^{-8} second [62]. Hence, fluorescence emission generally results from a thermally equilibrated excited state, that is, the lowest energy vibrational state of S_1.

Fluorophores in the S_1 states can undergo a spin conversion to the first triplet state T_1. The emission from T_1 is called phosphorescence, and the conversion of S_1 to T_1 is called intersystem crossing. Generally, phosphorescence can occur long (seconds to minutes) after the absorption, and is generally shifted to longer wavelengths (lower energy) relative to the

fluorescence. Fluorescence life-time and fluorescence emission spectrum are important characteristics of biological fluorophores. Common fluorophores in human tissues are collagen, nicotinamide adenine dinucleotide (NADH), and flavin adenine dinucleotide (FAD) [63-65]. It has been shown that NADH and collagen concentration increases with dysplasia, and detection of such changes can be used to identify tissue abnormality [65-67]. A summary of life-time and emission wavelength for common fluorophores in human tissues are shown in Table 2.2.

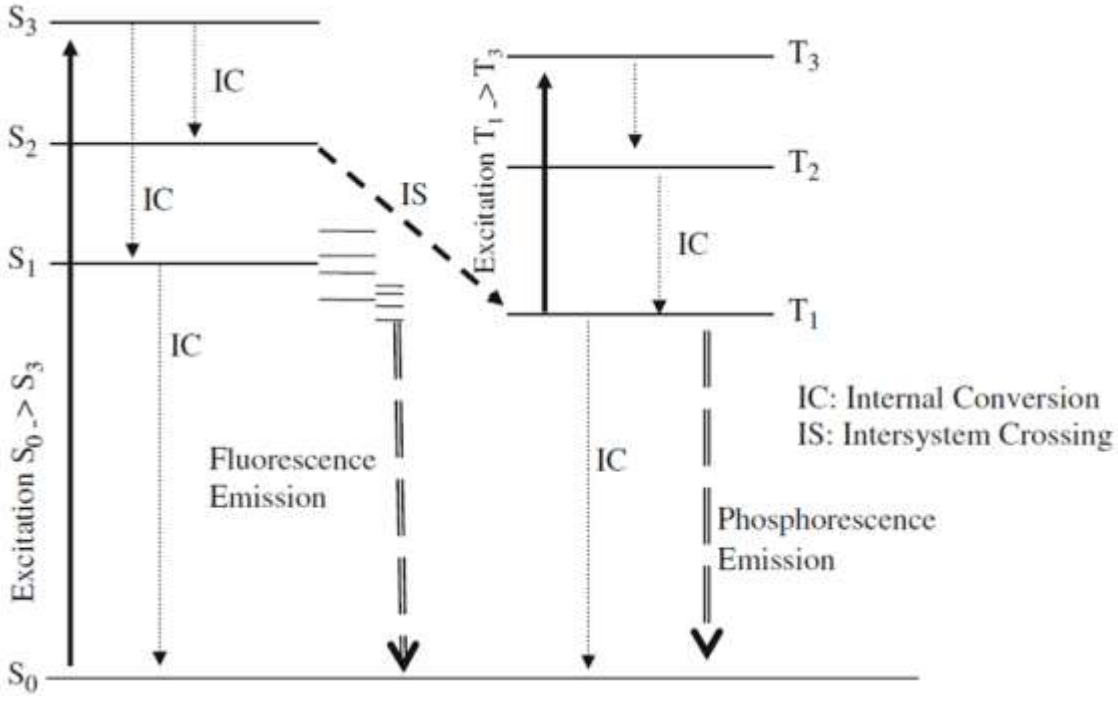

Fig. 2.9 The Jablonski diagram: absorption of light leads to excitation from S0 to S3 after which the absorbed energy can return to the ground state via internal conversions (with or without emission of light) or via an intersystem crossing to the triplet state. An absorption of another photon can lead to excitation in the triplet state. Fluorescence emission is from the lowest rotational level within the lowest vibrational level of the S1 state. Reprinted

from ref [53]. Copyright © 2010, Springer Science and Business Media B.V. Reprinted with permission.

Table 2.2 Summary of fluorescence characteristics of common fluorophores in human tissues

Fluorophore	excitation wavelength (nm)	emission wavelength (nm)	fluorescence life-time (ns)	Ref
NAD(P)H free	300-380	450-500	0.3	[68]
NAD(P)H free protein bound	300-380	450-500	2.0-2.3	[68]
FAD	420-500	520-570	2.91	[69]
flavin mononucleotide (FMN)	420-500	520-570	4.27-4.67	[70]
protoporphyrin IX	400-450	635,710	< 15	[71]
collagen	280-350	370-440	≤5.3	[68]
elastin	300-370	420-460	≤2.3	[72]

Besides the fluorescence process, a large portion of the absorbed energy is converted to heating. In general, temperature rise due to absorption of light is proportional to tissue absorption coefficients and the power of the radiance source. For example, assuming that there is no diffusion (the absorbed energy does not leave the area of the absorption during the optical pulse), temperature rise in tissue due to a short pulse of light is given by Eq. (2.2).

$$\Delta T = \frac{\mu_a H}{\rho c} \qquad (2.2)$$

In Eq. (2.2), μ_a is the absorption coefficient (cm^{-1}), H is the radiant exposure (J. cm^{-2}), ΔT is the temperature rise (^oC), ρ is the tissue density ($g.cm^{-3}$), and c is the specific heat capacity (J. $^oC^{-1}.g^{-1}$). For tissue, $\rho c \approx 4.2$ J. cm^{-3}. $^oC^{-1}$ [53]. For example, a radiant exposure of 1 J.cm^{-2} can result in 12 ^oC rise if μ_a = 50 cm^{-1}. In non-invasive optical diagnosis, temperature of tissue must be kept bellow the damaging temperature or critical temperature T_c [73]. Some of the examples for irreversible tissue damage expected as tissue temperature

rise above T_c are: tissue welding and vaporization at $T > 100$ ^oC, tissue pyrolysis at $T > 350$ ^oC. Both vaporization and pyrolysis are characteristics of laser surgical removal of tissue with thermal ablation [73]. In this thesis, the energy of excitation laser was kept under 3 μJ to avoid the potential thermal damage of biological tissue [74-76].

2.3.2 Measurement of tissue optical properties

The most difficult task of tissue optics is to develop methods that are fast, non-invasive, cost effective to measure optical properties of tissues, including absorption coefficient (μ_a), scattering coefficient (μ_s), and anisotropy (g) [52]. To reduce complexity, μ_s and g are often lumped into a reduced scattering coefficient, $\mu_s' = \mu_s (1-g)$ [77]. Studies have shown that optical properties tight to the concentration of absorbers and scatterers present in the tissue, and can be used to differentiate types of tissue and to detect any abnormal growth. For example, studying light scattering at cellular level, Drezek *et al.* and Arifler *et al.* showed that the level of light scattering increased during dysplastic progression due to changes of nuclei such as nuclear atypia [78,79]. At tissue level, Palmer *et al.* showed that μ_s' in breast tumor was 71% higher than normal breast tissues [80]. Furthermore, angiogenesis is a marker of precancer and cancer [81-83], and might cause an increase in hemoglobin concentration, resulting in an increase in light absorption [84]. Therefore, a quantitative and reliable approach for detecting neoplasm or tumor progression can be resulted from advances in optical properties measurement.

There are many different methods that have been used to measure optical properties of biological tissues. These methods can be divided into two categories: indirect and direct

measurement [85,86]. The advantages and disadvantages of each method is discussed below.

2.3.2.1 Direct measurement of optically thin sections: ex vivo application

Direct measurement refers to a method that can extract optical properties directly without using a model of light propagation. Direct method associates with the preparation of thin sample slides (thickness *d*), and is usually carried out using an integrating sphere. An intensive description of how to measure tissue optical properties using direct method can be found elsewhere [86,87], and can be summarized in Fig. 2.10. Principally, the total attenuation μ_t of the sample can be calculated from the measured transmission T_C using Eq. (2.3). The absorption coefficient μ_a is calculated using Eq. (2.4), where N_0 is the number of photons incident on the sample and N_a is the number of all photons transmitted or scattered by the sample and detected by the detector. In Eq. (2.4) and (2.5), η is the fraction of all photons within the integrating sphere that is detected (because integrating sphere has a highly diffuse reflective coating).

The scattering coefficient μ_s is calculated using Eq. (2.5) where N_s is the number of scattered photons detected. As shown in Fig. 2.10(c), when measuring μ_s, all collimated (unscattered) photons must be allowed to escape and not be detected along with N_s. In order to calculate anisotropy *g* using Eq. (2.6) [86,87], phase scattering function $p(\cos\theta)$ must be determined as illustrated in Fig. 2.10(d).

$$\mu_t = -\frac{1}{d} ln T_C \qquad (2.3)$$

$$\mu_a = -\frac{1}{d} ln\left(\frac{N_a}{\eta N_0}\right) \quad (2.4)$$

$$\mu_s = -\frac{1}{d} ln\left(1 - \frac{N_s}{\eta N_0}\right) \quad (2.5)$$

$$g = \int_{-1}^{1} \mathrm{p}(cos\theta) \cos\theta \, \mathrm{d}(cos\theta) \quad (2.6)$$

Unit of μ_t, μ_a, and μ_s is inverse unit of thickness d. In order to neglect multiple scattering in the thin sample, the sample thickness d must satisfies $d < 1/\mu_s$. Typically, in human tissue μ_s is within the range 20-100 cm^{-1} (g = 0.94 - 0.98) in wavelength range 400-800 nm [88]. This requires the sample thickness within a range of 10-200 μm. For this reason, as described in Chapter 3, direct measurement of Intralipid scattering coefficient with 1-mm thick quartz cuvette was applied only to solution with low lipid content (low scattering). Direct method for measuring tissue optical properties is associated with several disadvantages. The preparation of thin samples via sectioning of frozen tissues can alter optical properties, comparing to intact tissues. For example, 11% decrease in μ_a and 47% increase in μ_s' were observed in soft tissue samples (human aorta and rat jejunum) as the results of cryopreservation at 4 ^oC for 12 hours [89,90]. In addition, the thin sample must be supported by cuvette or glass slides which may introduce scattering artifacts. Due to the complications of sample preparation, direct method does not have potential for *in vivo* application [86,87].

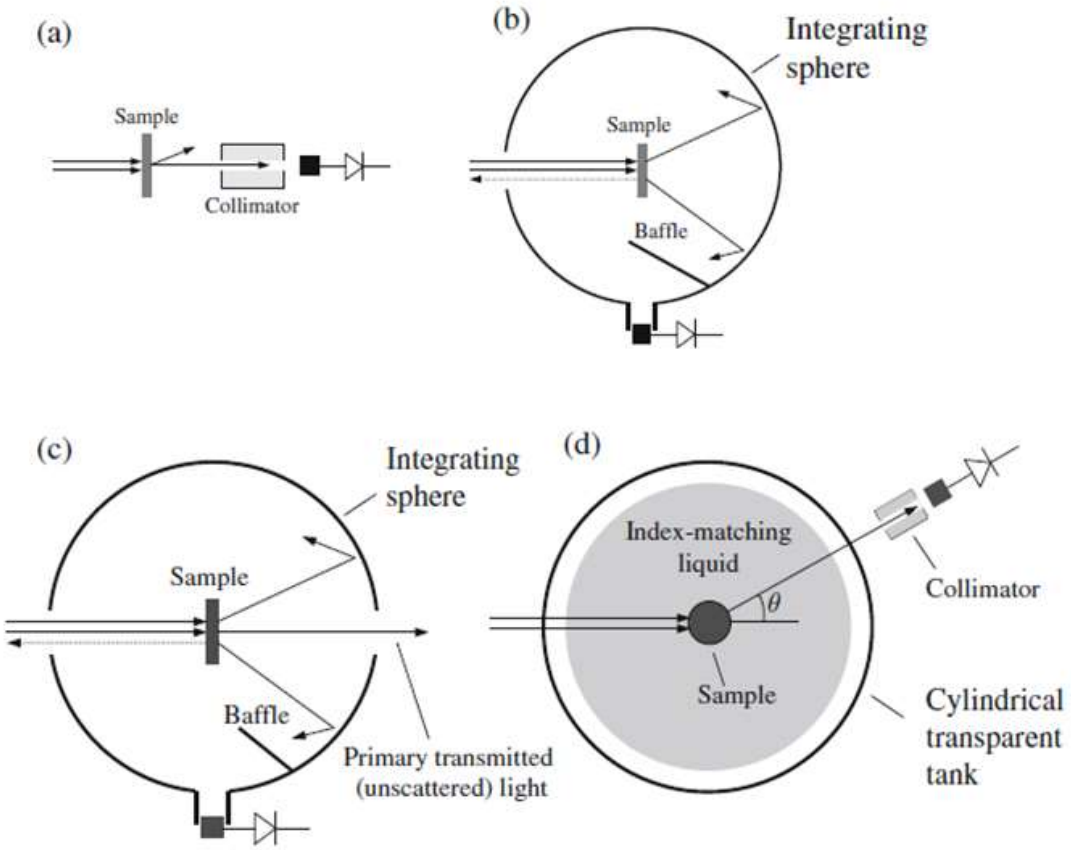

Fig. 2.10 Techniques for direct measuring optical properties with optically thin tissue sections: (a) Total attenuation coefficient μ_t, measuring the pencil beam transmission using a collimated detector. (b) Absorption coefficient μ_a, measuring the transmitted and scattered light using an integrating sphere. The specular reflectance is rejected through the input port, and the baffle prevents light scattered from the sample reaching the detector directly without re-scattering from the sphere. (c) Scattering coefficient μ_s, measuring the total scattered light. The unscattered primary photons exit via a small coaxial port. (d) Scattering phase function $p(\cos\theta)$, measuring the angular distribution of singly-scattered light using a collimated detector mounted on a rotating arm. Reprinted from ref [86]. Copyright © 2010, Springer Science and Business Media B.V. Reprinted with permission.

2.3.2.2 Indirect measurement of bulk tissues

Indirect measurement refers to method that extracts optical properties with the use of a light propagation model to solve the "inverse problem". That is the optical properties are placed into either a light propagation model, and the values of the measured parameters (i.e. diffuse reflectance) are fitted into optical properties [86]. Popular light propagation models used to provide approximate solutions to the radiation transport equation are: diffuse approximation [91,92], Monte Carlo simulations [80,93], and inverse adding-doubling (IAD) model [95-97]. Each of these methods has its own limitations and is discussed below.

2.3.2.2(a) Diffuse approximation

Diffuse approximation to radiative transport equation is valid only when scattering dominates absorption in the media ($\mu_s' \geq 10\mu_a$) [87], and when the point of interest (POI) is far enough from the source with a minimum at four reduced mean free path, $4/(\mu_a+\mu_s')$ [92]. For example, given that the first condition is satisfied at $\mu_a = 0.1$ cm^{-1} and $\mu_s' = 15$ cm^{-1}, a minimum source-POI distance of $4/26 \approx 0.27$ cm = 2.7 mm must also be satisfied. Furthermore, it was established that the ratio of μ_s'/μ_a in human tissues is much less than 8 in visible wavelength range, especially at 540 and 580 nm region of hemoglobin absorption [88,98,99]. Therefore, diffuse approximation only applies to simulation of non-contact illumination set-up, especially with near infrared illumination source (diffusive regime), and does not apply to contact illumination set-up, especially with visible light source (highly absorptive region) [100].

2.3.2.2(b) Adding doubling model

Adding-doubling refers to a numerical method to solve the radiation transport equation. The inverse adding doubling (IAD) solves for the optical properties using the measured transmission and reflectance. IAD starts with an initial guess of optical properties, and calculates the reflectance and transmission [94,95]. This process is repeated until a match is found, and the optical properties resulting in the matched values of transmission and reflectance are assumed to be the optical properties of the sample. IAD have several advantages over the direct method. While both μ_a and μ_s' were obtained from measurement of reflectance and transmission in IAD method, additional measurement for phase function is required in order to estimate g and μ_s' with direct method. In addition, because IAD already accounts for scattering artifact at boundaries (i.e. Fresnel refraction at air-glass surface), IAD is more accurate (with error less than 3%) in measuring of samples within glass slides. Furthermore, IAD is applicable for homogenous turbid slab with any optical thickness while direct method requires sample thickness d to be less than $1/\mu_s$ [52,87]. The main disadvantages of IAD associate with requirements of perfect measurement scenarios. For example, the slab has to be homogenous and uniformly illuminated. In addition, the sample has to be large enough to cover the entrance of integrating sphere, and has to be significantly larger than the beam diameter to avoid light loss to the sample side [96,97]. Light loss to the samples side results in overestimation of absorption coefficient of the sample [97]. Such perfect measurement scenarios usually limits IAD use to *ex vivo* measurement [86,87].

2.3.2.2(c) Monte Carlo simulations

Monte Carlo (MC) is the most common numerical method to solve the radiation transport equation [87]. An important advantage of MC is its capability to simulate a variety of contact and noncontact illumination, and detection setups [100]. Although inverse MC-based models are flexible and can be used to extract optical properties under different conditions such as variety of light sources, tissue types, and illumination geometries, they can be computationally intensive during forward simulations which typically require millions of photon (>> 10^6) to obtain adequate signal-to-noise ratio. While a standard forward MC simulation can reach 100 hours per $4x10^7$ photon launched for high scattering media ($\mu_s' = 100\ cm^{-1}$) [101], some of the fastest MC methods with modern computer power can accomplish a simulation time of less than 10 hours considering a number of photons in the order of 10^8. For example, Wang *et al.* and Le *et al.* used a condensed MC to achieve simulation time of 10 hours per $4x10^8$ photons launched on an IBM 3650 M2, 8 CPUs (each at 2.67 GHz) with 24 GB RAM [101,102], or Fang and Boas's MC achieved a simulation time of approximate 2.4 hours for 10^8 photons launched on G92 graphic processing unit [103]. Note that this is the time for only one single simulation for a pair of input optical properties at one specific wavelength. To develop an accurate MC-based inverse model for broadband white light measurement of optical properties, a reflectance database could be generated from as low as 20,000 pairs of optical properties [104,105]. Therefore, it is very time-consuming to develop a MC based inverse model to extract optical properties.

2.3.2.2(d) Experimental lookup table

A more recent indirect method to measure tissue optical properties relies on an experimental lookup table (LUT) generated from experimental measurement of optical phantoms [106-109]. There are several key advantages of the LUT-method over other indirect methods. LUT method relies solely on measurement of optical phantoms, and does not require any computational models of light propagation to calculate optical properties. Furthermore, LUT can be used to map a broader range of optical properties than permitted with current diffuse approximation methods. For example, diffuse approximation can no longer extract μ_a when $\mu_s'/\mu_a < 4$ while LUT can achieve accuracy of 10% [106]. In general, diffuse approximation works best for a reduced albedo a' larger than 0.9, where $a' = \mu_s' / (\mu_a + \mu_s')$ whereas LUT method valid for a' value as low as 0.35 [106-109], and for a source-detector distance up to 1.48 mm [109]. LUT method has been used to measure optical properties and extract oxygen saturation of skin cancer [106,110,111]. In this thesis, a LUT method was developed to extract optical properties of brain tissue specimen using a fiber optic probe with source-detector distance of 0.23 mm and of 0.59 mm. Detail on the LUT can be found in Chapter 5.

2.3.3 Effect of sampling volume on the detection of fluorescence

In earlier studies, one of the problem encountered when measuring fluorescence from tissue samples is that the sampling volume varies due to the aggregation and micro-environmental changes [112-114]. Such variation could alter the fluorescence quantum yield of the fluorophore, resulting the difference between *in vivo* fluorescence and *ex vivo*

fluorescence intensity. In more recent studies, Pogue *et al*. and Lee *et al*. designed the optical fiber probe which was tested on optical phantoms to study this phenomenon [115,116]. It was concluded that the detected fluorescence signal was not strongly affected by tissue optical properties when sampling volume was smaller in dimension than the average mean free path (~ 100 μm) [115-118]. Furthermore, Pogue *et al*. investigated the spatial variance of the measured fluorescence *in vivo*, and showed that the use of 100 μm fibers could accurately measure the mean fluorescence intensity with a millimeter size scale [119].

References

1. L. V. Kalia, "Anatomy and Physiology of the Brain." Metabolism of Human Diseases: Organ Physiology and Pathophysiology **5** (2014).

2. A. N. Yaroslavsky et al., "Optical properties of selective native and coagulated human brain tissues in vitro in the visible and near infrared spectral range, " Phys Med. Biol. **47**, 2059-2073 (2002).

3. J. F. Beek et al, "In vitro double-integrating-sphere optical properties of tissues between 630 and 1064 nm," Phys. Med. Biol. **42**, 2255-2261 (1997).

4. S. C. Gebhart, W. C Lin, A. Mahadevan-Jansen, "In vitro determination of normal and neoplastic human brain tissue optical properties using inverse adding-doubling." Phys. Med. Biol. **51**, 2011-2027 (2006).

5. Q. T Ostrom, et al. "CBTRUS Statistical Report: Primary Brain and Central Nervous System Tumors Diagnosed in the United States in 2008-2012." Neuro-oncology **17**, iv1-iv62 (2005).

6. R. L. Siegel et al., "Cancer statistics, 2016." CA: A cancer journal for clinicians (2015).

7. A. Agnihotri et al., "Glioblastoma, a brief review of history, molecul ar genetics, animal models and novel therapeutic strategies,"Arch. Immunol. Ther. Exp. **61**, 25-41(2013).

8. D. N. Louis et al., "The 2007 WHO classification of tumours of the central nervous system." Acta neuropathologica **114**, 97-109(2007).

9. E. Hansson, and L. Rönnbäck. "Glial neuronal signaling in the central nervous system." The FASEB Journal 17.3, 341-348 (2003).

10. N. J. Abbott, et al. "Structure and function of the blood–brain barrier." Neurobiology of disease 37.1, 13-25 (2010).

11. K. R. Jessen, "Glial cells." The international journal of biochemistry & cell biology 36, 1861-1867 (2004).

12. S. J. Price, and J. H. Gillard. "Imaging biomarkers of brain tumour margin and tumour invasion." The British journal of radiology (2014).

13. A. Lilja, K. Bergstrom, B. Spannare, Y. Olsson, Reliability of computed tomography in assessing histopathological features of malignant supratentorial gliomas. J Comput Assist Tomogr 5:625–36 (1981).

14. R. G. Selker, H. Mendelow, M. Walker, P. E. Sheptak, J. G. Phillips. Pathological correlation of CT ring in recurrent, previously treated gliomas. Surg Neurol. 17, 251–4 (1982).

15. M. Watanabe, R. Tanaka, N. Takeda. Magnetic resonance imaging and histopathology of cerebral gliomas. Neuroradiology 34, 463–9 (1992).

16. L. D. Lunsford, A. J. Martinez, R. E. Latchaw. Magnetic resonance imaging does not define tumor boundaries. Acta Radiol Suppl 369, 154–6 (1986).

17. Golla H et al. "Glioblastoma multiforme from diagnosis to death: a prospective, hospital-based, cohort, pilot feasibility study of patient reported symptoms and needs," Supportive Care in Cancer **22**, 3341-3352 (2014).

18. D. Ricard et al., "Primary brain tumours in adults." The Lancet **379**, 1984-1996 (2012).

19. A. Behin et al., "Primary brain tumours in adults." The Lancet **361**, 323-331 (2003).

20. P. Kleihues et al., "Histopathology, classification, and grading of gliomas." Glia **15**, 211-221 (1995).

21. T. Homma et al. "Correlation among pathology, genotype, and patient outcomes in glioblastoma." J. Neuropath. Experim. Neurol. **65**, 846-854 (2006).

22. F. J. Rodriguez et al., "Neoplastic cells are a rare component in human glioblastoma microvasculature," Oncotarget **3**, 98-106 (2012).

23. R. Wang et al. "Glioblastoma stem-like cells give rise to tumour endothelium." Nature **468**, 829-833 (2010).

24. A. Veeravagu et al, "Biopsy versus resection for the management of low-grade gliomas," Cochrane Database Syst. Rev. **4**, (2013).

25. A. Olivier, T. Peters, and G. Bertrand, "Stereotactic system and apparatus for use with magnetic resonance imaging, computerized tomography and digital subtraction imaging," Appl. Neurophysiol. **48**, 94-96 (1985).

26. J. Schenck et al., "Superconducting open-configuration MR imaging system for image-guided therapy," Radiology **195**, 805–814 (1995).

27. G. F. Woodworth et al., "Frameless image-guided stereotactic brain biopsy procedure: diagnostic yield, surgical morbidity, and comparison with the frame-based technique," J. Neurosurgery **104**, 233-2372 (2006).

28. V. M. Tronnie et al., "Intraoperative diagnostic and interventional magnetic resonance imaging in neurosurgery," Neurosurgery **40**, 891-902 (1997).

29. L. Walton, A. Hampshire, D. M. C. Forster, and A. Kemeny, "A phantom study to assess the accuracy of stereotactic localization, using T1-weighted magnetic resonance imaging with the Leksell stereotactic system," Neurosurgery **38**, 170-178 (1996).

30. A. Nabavi et al., "Serial intraoperative magnetic resonance imaging of brain shift," Neurosurgery **48**, 787-798 (2001).

31. D. W. Roberts et al., "Intraoperative brain shift and deformation: a quantitative analysis of cortical displacement in 28 cases," Neurosurgery **43**, 749-758 (1998).

32. J. Hu et al., "Intraoperative brain shift prediction using a 3D inhomogeneous patient-specific finite element model," J. Neurosurgery **106**, 164-169 (2007).

33. D. B. FitzGerald et al., "Location of language in the cortex: a comparison between functional MR imaging and electrocortical stimulation," American J. Neuroradiology **18**, 1529-1539 (1997).

34. D. Pauleit et al., "O-(2-[18F] fluoroethyl)-L-tyrosine PET combined with MRI improves the diagnostic assessment of cerebral gliomas," Brain **128**, 678-687(2005).

35. A. Raheja et al., "Initial experience of using high field strength intraoperative MRI for neurosurgical procedures," Journal of Clinical Neuroscience: official journal of the Neurosurgical Society of Australasia **22**, 1326-1331(2015).

36. C. Senft et al., "Intraoperative MRI guidance and extent of resection in glioma surgery: a randomised, controlled trial," The Lancet Oncology **12**, 997-1003 (2011).

37. J. Coburger et al., "Sensitivity and specificity of linear array intraoperative ultrasound in glioblastoma surgery: a comparative study with high field intraoperative MRI and conventional sector array ultrasound," Neurosurgical Review **38**, 499-509(2015).

38. R. Ramina et al., "Optimizing costs of intraoperative magnetic resonance imaging. A series of 29 glioma cases." Acta Neurochirurgica **152**, 27-33(2010).

39. H. Hirschberg et al., "Impact of intraoperative MRI on the surgical results for high-grade gliomas." Minimally Invasive Neurosurgery **48**, 77-84 (2005).

40. Z. Z. Zhang et al., "The Art of Intraoperative Glioma Identification," Frontiers in Oncology **5** (2015).

41. P. L. Kubben et al., "Intraoperative MRI-guided resection of glioblastoma multiforme: a systematic review." The Lancet Oncology **12**, 1062-1070(2011).

42. W. F. Chandler et al., "Intraoperative use of real-time ultrasonography in neurosurgery," J. Neurosurgery **57**, 157-163 (1982).

43. A. Jödicke, T. Springer, and D. K. Boeker, "Real-time integration of ultrasound into neuronavigation: technical accuracy using a light-emitting-diode-based navigation system," Acta Neurochirurgica **146**, 1211-1220 (2004).

44. M. A. Hammoud et al., "Use of intraoperative ultrasound for localizing tumors and determining the extent of resection: a comparative study with magnetic resonance imaging." J. Neurosurgery **84**, 737-741 (1996).

45. V. V. Velthoven, and L. M. Auer, "Practical application of intraoperative ultrasound imaging," Acta Neurochirurgica **105**, 5-13(1990).

46. A Jödicke et al., "Intraoperative three-dimensional ultrasonography: an approach to register brain shift using multidimensional image processing," Minimally invasive neurosurgery **41**, 13-19 (1998).

47. S. Q. Yu et al., "Diagnostic significance of intraoperative ultrasound contrast in evaluating the resection degree of brain glioma by transmission electron microscopic examination," Chinese Medical Journal **128**, 186 (2015).

48. O M. Rygh et al., "Comparison of navigated 3D ultrasound findings with histopathology in subsequent phases of glioblastoma resection," Acta Neurochirurgica **150**, 1033-1042 (2008).

49. E. L. Rosenthal et al., "The status of contemporary image-guided modalities in oncologic surgery," Annals of Surgery **261**, 46-55 (2015).

50. P. Charlesworth, and T. G. Truscott, "The use of 5-aminolevulinic acid (ALA) in photodynamic therapy (PDT)." J. Photochemistry and Photobiology B: Biology **18**, 99-100 (1993).

51. D. W. Roberts et al., "Coregistered fluorescence-enhanced tumor resection of malignant glioma: relationships between δ-aminolevulinic acid–induced protoporphyrin IX fluorescence, magnetic resonance imaging enhancement, and neuropathological parameters," J. Neurosurgery **114**, 595 (2011).

52. A. J. Welch, M. J. C. van Gemert, and W. M. Star, "Definitions and overview of tissue optics," In Optical thermal response of laser irradiated tissue, eds. A J Welch & M J C van Gemert, 2nd edn (Springer Science & Business Media, NY, 2011).

53. J. T. Walsh, "Basic Interactions of Light with Tissue," In Optical thermal response of laser irradiated tissue, eds. A J Welch & M J C van Gemert, 2nd edn (Springer Science & Business Media, NY, 2011).

54. T. J. Huppert, "History of Diffuse Optical Spectroscopy of Human Tissue." Optical Methods and Instrumentation in Brain Imaging and Therapy, ed. A. J. Madsen (Springer, NY, 2013).

55. G. Zonios, L. T. Perelman, V. Backman, R. Manoharan, M. Fitzmaurice, J. V. Dam, and M. S. Feld, "Diffuse reflectance spectroscopy of human adenomatous colon polyps in vivo," Appl. Opt. **38**, 6628 (1999)

56. J. M. Schmitt, and G. Kumar, "Optical scattering properties of soft tissue: a discrete particle model, " Appl. Opt. **37**, 2788 (1998).

57. B. W. Pogue, and M. S. Patterson, "Review of tissue simulating phantoms for optical spectroscopy, imaging and dosimetry," J. Biomed. Opt. **11**, 041102-041102 (2006).

58. J. Mobley, "Optical properties of tissues," In Biomedical Photonics Handbook, ed. Tuan Vo-Dinh (CRC Press LLC, FL, 2003).

59. R. Drezek, A. Dunn, and R. Richards-Kortum, "Light scattering from cells: finite-difference time-domain simulations and goniometric measurements," Appl. Opt. **38**, 3651-3661 (1999).

60. J. R. Mourant et al., "Mechanisms of light scattering from biological cells relevant to noninvasive optical-tissue diagnostics." Appl. Opt. **37**(16), 3586-3593 (1998).

61. J. R. Mourant et al. "Light scattering from cells: the contribution of the nucleus and the effects of proliferative status." BiOS 2000 The International Symposium on Biomedical Optics. International Society for Optics and Photonics, 2000.

62. J. R. Lakowicz, Principles of fluorescence spectroscopy (Springer Science & Business Media, 2013).

63. R. Richards-Kortum et al., "Survey of endogenous biological fluorophores" In Handbook of biomedical fluorescence, pp. 237-264, eds. M. A. Mycek & B. W. Pogue (Marcel Dekker Inc., NY, 2003).

64. A. Dellas et al., "Angiogenesis in cervical neoplasia: microvessel quantitation in precancerous lesions and invasive carcinomas with clinicopathological correlations," Gynecol. Oncol. **67**, 27-33 (1997).

65. R. Drezek, K. Sokolov, U. Utzinger, I. Boiko, A. Malpica, M. Follen, R. Richards-Kortstum, "Understanding the contributions of NADH and collagen to cervical tissue fluorescence spectra: modeling, measurements, and implications." J. Biomed. Opt. 6(4), 385-396 (2001).

66. R. W. Redmond, "Introduction to fluorescence and photophysics," in Handbook of biomedical fluorescence, pp.1-28, eds. M. A. Mycek & B.W. Rogue, (Marcel Dekker Inc., NY, 2003).

67. Z. Volynskaya et al., "Diagnosing breast cancer using diffuse reflectance spectroscopy and intrinsic fluorescence spectroscopy." J. Biomed. Opt. 13, 024012-024012 (2008).

68. K. König, "Clinical multiphoton tomography." J. Biophotonics **1**, 13-23 (2008).

69. B. Koziol et al, "Riboflavin as a source of autofluorescence in Eisenia fetida coelomocytes," Photochemistry and Photobiology **82**, 570-573(2006).

70. H Grajek et al. "Flavin mononucleotide fluorescence intensity decay in concentrated aqueous solutions." Chemical Physics Letters **439**, 151-156(2007).

71. T. Glanzmann et al., "Time-resolved spectrofluorometer for clinical tissue characterization during endoscopy." Review of Scientific Instruments **70**, 4067-4077 (1999).

72. J. M. I. Maarek et al., "Time-resolved Fluorescence Spectra of Arterial Fluorescent Compounds: Reconstruction with the Laguerre Expansion Technique," Photochemistry and photobiology **71**, 178-187 (2000).

73. V. V. Tuchin, "Light-Tissue Interactions," In Biomedical Photonics Handbook, ed. Tuan Vo-Dinh (CRC Press LLC, FL, 2003).

74. L. Marcu, W. S. Grundfest, and J. M. Maarek, "Photobleaching of arterial fluorescent compounds: Characterization of elastin, collagen and cholesterol time-resolved spectra during prolonged ultraviolet irradiation, " Photochem. Photobiol., **69**, 713–721 (1999).

75. American National Standard for Safe Use of Lasers, Laser Institute of America ANSI Z136.1-2007, 2007.

76. J. A. Zuclich, "Ultraviolet-induced photochemical damage in ocular tissues," Health Phys. **56**, 671–682 (1989).

77. W. Wang et al. "Measurement of internal tissue optical properties at ultraviolet and visible wavelengths: Development and implementation of a fiberoptic-based system." Optics Express **16**, 8685-8703 (2008).

78. R. Drezek et al., "Light scattering from cervical cells throughout neoplastic progression: influence of nuclear morphology, DNA content, and chromatin texture, " J. Biomed. Opt. **8**, 7-16 (2003).

79. D. Arifler et al., "Light scattering from normal and dysplastic cervical cells at different epithelial depths: finite-difference time-domain modeling with a perfectly matched layer boundary condition, " J. Biomed. Opt. **8**, 484-494 (2003).

80. G. M. Palmer, M. Gregory, C. Zhu, T. M. Breslin, F. Xu, K. W. Gilchrist, and N. Ramanujam, "Monte Carlo-based inverse model for calculating tissue optical properties. Part II: Application to breast cancer diagnosis, " Appl. Opt. **45**, 1072-1078(2006).

81. F. J. Rodriguez et al., "Neoplastic cells are a rare component in human glioblastoma microvasculature," Oncotarget 3, 98-106 (2012).

82. R. Wang et al. "Glioblastoma stem-like cells give rise to tumour endothelium." Nature **468**, 829-833 (2010).

83. A. Dellas et al., "Angiogenesis in cervical neoplasia: microvessel quantitation in precancerous lesions and invasive carcinomas with clinicopathological correlations," Gynecol. Oncol. **67**, 27-33 (1997).

84. G. Zonios, L. T. Perelman, V. Backman, R. Manoharan, M. Fitzmaurice, J. V. Dam, and M. S. Feld, "Diffuse reflectance spectroscopy of human adenomatous colon polyps in vivo," Appl. Opt. **38**, 6628 (1999)

85. B. C. Wilson, M. S. Patterson, and S. T. Flock, "Indirect versus direct techniques for the measurement of the optical properties of tissues." Photochemistry and photobiology **46**, 601-608 (1987).

86. A. Kim, and B.C. Wilson, " Measurement of ex vivo and in vivo tissue optical properties: methods and theories, " In Optical thermal response of laser irradiated tissue, eds. A J Welch & M J C van Gemert, 2nd edn (Springer Science & Business Media, NY, 2011).

87. S. J. Madsen, and B. C. Wilson, "Optical properties of brain tissue," In Optical methods and instrumentation in brain imaging and therapy, ed. S. J. Madsen (Springer, NY, 2013).

88. S. L. Jacques, "Optical properties of biological tissues: a review," Physics in Medicine and Biology **58**, R37 (2013).

89. I. F. Çilesiz, and A. J. Welch, "Optical properties of human aorta: are they affected by cryopreservation?," Lasers Surg. Med. **14**, 396-402 (1994).

90. E. Chan, T. Menovsky, and A. J. Welch," Effects of cryogenic grinding on soft-tissue optical properties," Appl. Opt. **3**, 4526-4532 (1996).

91. T. J. Farrell, M. S. Patterson, and B. C. Wilson, "A diffusion theory model of spatially resolved, steady-state diffuse reluctance for the non-invasive determination of tissue optical properties in vivo," Med. Phys. **19**, 879-888 (1992).

92. D. J. Cuccia, F. Bevilacqua, A. J. Durkin, F. R. Ayers, and B. J. Tromberg, "Quantitation and mapping of tissue optical properties using modulated imaging," J. Biomed. Opt. **14**, 024012-024012(2009).

93. G. M. Palmer, and N. Ramanujam, "Monte Carlo-based inverse model for calculating tissue optical properties. Part I: Theory and validation on synthetic phantoms," Appl. Opt. **45**, 1062-1071 (2006).

94. S. C. Gebhart, W. C Lin, A. Mahadevan-Jansen, "In vitro determination of normal and neoplastic human brain tissue optical properties using inverse adding-doubling," Phys Med Biol 51, 2011-2027 (2006).

95. S. A. Prahl, M. J. van Gemert, and A. J. Welch, "Determining the optical properties of turbid media by using the adding–doubling method," Appl. Opt. **32**, 559-568(1993).

96. S. Prahl, "Optical property measurements using the inverse adding-doubling program." [Online document], http://omlc. ogi. edu/pubs/pdf/man_iad. pdf, Accessed 3 08 (1999).

97. J. W. Pickering, S. A. Prahl, N. van Wieringen, J. F. Beek JF, H.J.C.M. Sterenborg, M.J.C. van Gemert, "Double-integrating-sphere system for measuring the optical properties of tissue,"Appl. Opt. **32**, 399-410 (1993).

98. W. Cheong, S. Prahl, and A. Welch, "A review of the optical properties of biological tissues," IEEE journal of Quantum Electronics **26**(12), 2166-2185 (1990).

99. R. M. P. Doornbos, R. Lang, M. C. Aalders, F. W. Cross, and H. J. C. M. Sterenborg, "The determination of in vivo human tissue optical properties and absolute chromophore concentrations using spatially resolved steady-state diffuse reflectance spectroscopy," Phys. Med. Biol. **44**, 967-981 (1999).

100. C. Zhu, and Q. Liu, "Review of Monte Carlo modeling of light transport in tissues." J. Biomed. Opt. **18**, 050902-050902(2013).

101. Q. Wang, A. Agrawal, N. S. Wang, and T. J. Pfefer, "Condensed Monte Carlo modeling of reflectance from biological tissue with a single illumination–detection fiber," Selected Topics in Quantum Electronics, IEEE Journal of, **16**, 627-634(2010).

102. V. N. Du Le, Q. Wang, T. Gould, J. C. Ramella-Roman, and T. J. Pfefer, "Vascular contrast in narrow-band and white light imaging," Appl. Opt. **53**, 4061-4071(2014).

103. Q. Fang, and D. A. Boas, "Monte Carlo simulation of photon migration in 3D turbid media accelerated by graphics processing units," Optics Express **17**, 20178-20190 (2009).

104. Q. Wang, K. Shastri, and T. Joshua Pfefer, "Experimental and theoretical evaluation of a fiber-optic approach for optical property measurement in layered epithelial tissue," Appl. Opt. **49**, 5309-5320 (2010).

105. Q. Wang, V. N. Du Le, J. Ramella-Roman, and J. Pfefer, "Broadband ultraviolet-visible optical property measurement in layered turbid media," Biomedical Optics Express **3**, 1226-1240 (2012).

106. N. Rajaram, T. H. Nguyen, and J. W. Tunnell, "Lookup table–based inverse model for determining optical properties of turbid media," J. Biomed. Opt. **13**, 050501-050501 (2008).

107. T. A. Erickson, A. Mazhar, D. Cuccia, A. J. Durkin, and J. W. Tunnell, "Lookup-table method for imaging optical properties with structured illumination beyond the diffusion theory regime, " J. Biomed. Opt. **15**, 036013-036013 (2010).

108. N. Rajaram, T. J. Aramil, K. Lee, J. S. Reichenberg, T. H. Nguyen, and J. W. Tunnell, "Design and validation of a clinical instrument for spectral diagnosis of cutaneous malignancy," Appl. Opt. **49**, 142-152 (2010).

109. B. S. Nichols, N. Rajaram, and James W. Tunnell. "Performance of a lookup table-based approach for measuring tissue optical properties with diffuse optical spectroscopy." J. Biomed. Opt. **17**, 0570011-0570018 (2012).

110. L. Lim et al., "Probe pressure effects on human skin diffuse reflectance and fluorescence spectroscopy measurements." J. Biomed. Opt. **16**, 011012-011012(2011).

111. N. Rajaram et al., "Pilot clinical study for quantitative spectral diagnosis of non-melanoma skin cancer," Lasers Surg. Med. **42**, 876-887 (2010).

112. G. J. Smith, "The effects of aggregation on the fluorescence and the triplet state yield of hematoporphyrin." Photochemistry and photobiology 41.2 (1985): 123-126.

113. B. Aveline, T. Hasan, and R.W. Redmond. "photophysical and photosensitizing properties of benzoporphyrin derivative monoacid ring a (bpd-ma)." Photochemistry and photobiology 59.3 (1994): 328-335.

114. J. Moan, A. Helle, and Q. Peng, "A transient reduction of the fluorescence of aluminium phthalocyanine tetrasulphonate in tumours during photodynamic therapy." J. Photochemistry and Photobiology B: Biology 5 115-119 (1990).

115. B. W. Pogue, and G. Burke. "Fiber-optic bundle design for quantitative fluorescence measurement from tissue." Applied Optics 37, 7429-7436(1998).

116. C. C. Lee, B.W. Pogue, R. R. Strawbridge, K. L. Moodie, L. Bartholomew, G. C. Burke, P. J. Hoope, "Comparison of Photosensitizer (AlPcS2) Quantification

Techniques: In Situ Fluorescence Microsampling Versus Tissue Chemical Extraction". Photochemistry and Photobiology 74, 453-460 (2001).

117. B. W. Pogue, and T. Hasan, "Fluorophore quantitation in tissue-simulating media with confocal detection." IEEE Journal of Selected Topics in Quantum Electronics 2, 959-964 (1996).

118. C. Sheng, B. W. Pogue, E. Wang, J. E. Hutchins, P. J. Hoopes, "Assessment of Photosensitizer Dosimetry and Tissue Damage Assay for Photodynamic Therapy in Advanced-stage Tumors," Photochemistry and Photobiology 79(6), 520-526 (2004).

119. B. W. Pogue, et al. "Analysis of sampling volume and tissue heterogeneity on the in vivo detection of fluorescence." J. Biomed. Opt. 10, 041206-041206 (2005).

Chapter 3: Paper I - Measurements of Extrinsic Fluorescence in Intralipid and Polystyrene Microspheres

Vinh Nguyen Du Le[1*], Zhaojun Nie[2], Joseph E. Hayward[1], Thomas J. Farrell[1] and Qiyin Fang[2,3]

[1]Medical Physics and Applied Radiation Sciences, McMaster University, Hamilton, Ontario, Canada

[2]School of Biomedical Engineering, McMaster University, Hamilton, Ontario, Canada

[3]Department of Engineering Physics, McMaster University, Hamilton, Ontario, Canada

Received 5 Mar 2014; revised 27 May 2014; accepted 16 Jul 2014; published 22 Jul 2014

Published in Biomedical Optics Express, **5**(8), 2726-2735(2014)

Introduction to paper I

In this paper, the investigation of materials to produce optical phantoms for fluorescence studies was performed. To validate the measured fluorescence life-time and intensity, it is important that the observation of fluorescence from the target fluorophore is separated from that of back-ground fluorescence. Intralipid has been widely used in research to simulate optical phantoms for diffuse reflection and fluorescence studies with the assumption that lipid's fluorescence is minor and can be ignored. However, experimental validation of Intralipid extrinsic fluorescence has not been the subject of extensive study in the biomedical optics literature. As the result, a widespread ignorance of Intralipid's fluorescence has occurred without rigorous validation. Although it was suggested that lipid content is likely to fluoresce visible radiation when illuminated with ultraviolet radiation, supportive data was not available. In order to elucidate Intralipid fluorescence in a quantitative manner, this paper measured Intralipid fluorescence intensity and life-time as a function of lipid concentrations and scattering coefficients. A similar analysis for polymer microsphere was also performed, and compared.

In this paper, I developed the phantom models and Mie calculator, and carried out all experimental measurements and data analysis. Zhaojun Nie helped me with initial system trouble-shooting.

The manuscript was written by me, and edited by Drs. Farrell, Hayward, and Fang. Zhaojun did not contribute in the writing of the manuscript.

The manuscript has been slightly altered to confront the style of the thesis as whole, such as font, spacing, numbering of pages, equations, and figures and tables.

Contents of Paper I

3.1 Abstract

The fluorescence of Intralipid and polystyrene microspheres with sphere diameter of 1 μm at a representative lipid and microsphere concentration for simulation of mucosal tissue scattering has not been a subject of extensive experimental study. In order to elucidate the quantitative relationship between lipid and microsphere concentration and the respective fluorescent intensity, the extrinsic fluorescence spectra between 350-650 nm (step size of 5 nm) were measured at different lipid concentrations (from 0.25% to 5%) and different microsphere concentrations (0.00364, 0.0073, 0.0131 spheres per cubic micrometer) using laser excitation at 355 nm with pulse energy of 2.8 μJ. Current findings indicated that Intralipid has a broadband emission between 360-650 nm with a primary peak at 500 nm and a secondary peak at 450 nm while polystyrene microspheres have a single peak at 500 nm. In addition, for similar scattering properties the fluorescence of Intralipid solutions is approximately three-fold stronger than that of the microsphere solutions. Furthermore, Intralipid phantoms with lipid concentrations ~ 2% (simulating the bottom layer of mucosa) produce up to seven times stronger fluorescent emission than phantoms with lipid concentration ~ 0.25% (simulating the top layer of mucosa). The fluorescence decays of Intralipid and microsphere solutions were also recorded for estimation of fluorescence lifetime.

3.2 Introduction

Mucosal tissues in the oral cavity, pharynx, esophagus, and digestive system are targets of mucosal cancer, which is responsible for approximately 200,000 deaths annually in the United States [1]. Optical spectroscopic methods have been investigated as potential minimally-invasive techniques for early diagnosis and treatment [2-4]. In these studies, phantoms simulating key tissue optical properties (e.g. absorption and scattering coefficients) are extensively used in developing theoretical models [2-4]. Mucosal tissues have two distinguished layers – the epithelium on top of the stromal layer [5,6]. The reduced-scattering coefficients (μ_s') of the stromal layer is about 6-fold higher than that of the epithelium [5,6]. The epithelial layer thickness is approximately 300 μm [7], which is only a small fraction of the bottom layer thickness [7,8]. Therefore, simulating scattering of the stromal layer of the mucosa is important to mimic mucosal tissues.

Intralipid® 10% (defined as: 10 grams of lipids per 100 ml of suspension solution) is commercially available from Fresenius Kabi (Uppsala, Sweden) and Kabivitrum (Stockholm, Sweden) [9]. Dilution of stock Intralipid has been used to simulate tissue scattering in optical phantoms due to the resemblance of its reduced scattering spectrum to that of human tissues, its low absorption [10-13], and low cost [14]. In many studies, the fluorescence of Intralipid was assumed to be small or negligible in the visible region (350-650 nm) [11-13]. On the other hand, Pogue and Patterson [14] suggested that the lipid content of Intralipid phantoms is likely to fluoresce in the visible region when illuminated with ultraviolet excitation. Anand *et al*. reported that the fluorescence of Intralipid with lipid concentration as low as 0.25 % *v/v* is significant between 390-420 nm when they

attempted to use Intralipid as the background scattering to measure the time-resolved fluorescent spectrum of tyrosine dye (emission peak at 290 nm) [15]. Therefore, the endogenous fluorescence of Intralipid is likely to interfere with diffuse reflection measurements in phantom studies and thus influence the prediction of optical properties. However, because of the low concentration of lipid (below 0.25%, notation "v/v" is omitted in further discussion of Intralipid) used in the previous study [15], the simulated scattering of the phantoms was much lower than scattering of human tissue, especially the mucosal tissues. In order to produce Intralipid phantoms simulating mucosal scattering, lipid concentrations of above 1.5% (1.5 grams of lipids per 100 ml of suspension solution) should be used.

Polybead microsphere with sphere diameter of 1 μm is the other common choice for simulating tissue scattering [16-19]. These spheres were preferred not only due to their similar scattering to that of tissues but also their well-controlled size and index of refraction, and their excellent agreement of scattering properties with Mie's theory [16-18]. A previous study using fiber optics spectroscopy claims that fluorescence of microsphere (diameter of 1 μm) phantoms with concentration of 0.72% (defined as 0.72 gram of particles per 100 ml suspension solution, corresponding to approximately 0.0131 spheres per cubic micron) after mixing with hemoglobin solution is small and negligible [19]. However, hemoglobin strongly absorbs photons in the visible region, and fluorescence signal from this region might not be detected.

While matching Intralipid and polystyrene microspheres scattering to tissue scattering is certainly a key requirement in the fabrication of optical phantoms for fluorescence and

diffuse reflectance studies, the assumption that their fluorescence is small and can be neglected has not been rigorously validated. The purpose of this study is to establish the fluorescence profile of both Intralipid and polystyrene microspheres in optical phantom studies for the broadband spectral region 360-650 nm by separately evaluating the fluorescent intensity of the Intralipid and microsphere phantoms at concentrations that mimic tissue scattering. This was achieved by performing fluorescence spectroscopy of the phantoms using an optical fiber coupled with a spectrometer. In addition, the fluorescence decays of these phantoms were measured with a time-resolved fluorescence spectroscopy system and the average fluorescence lifetime was retrieved for comparison with that of other fluorescent dyes of biological importance.

3.3 Methods

3.3.1 Intralipid phantoms

Three sets of seven Intralipid phantoms (total of 21 phantoms) with concentrations of 0.25%, 0.5%, 1%, 1.5%, 2%, 3% and 5% were created for fluorescence measurements. These phantoms were prepared by diluting the concentrated Intralipid® 20% solution (manufactured by Fresenius Kabi, Uppsala, Sweden and distributed by Baxter Healthcare Corp., Deerfield, IL) in de-ionized water. The volume of each phantom was 10 ml which was contained within 12 ml test tubes. A separate set of phantoms with much lower lipid concentration 0.05% - 0.25% was also prepared for transmission measurements using a collimated xenon lamp light source from a spectrometer (Ultraspec 3000, Pharmacia Biotech Inc., NJ). The transmission data (T) were used to calculate scattering coefficients

(μ_s) by applying the relationship $\mu_S = -\ln(T)/L$, where L = 1 mm is the path length of the quartz cuvette used [20]. The measurements allowed extrapolation of μ_s for phantoms with higher lipid concentration

3.3.2 Microsphere phantoms and Mie theory

Three microsphere phantoms with concentrations of 0.72 %, 0.4%, 0.2% solids *w*/*v* aqueous suspension were prepared by diluting the 2.5% (the notation of *w*/*v* is omitted in further discussion of microspheres) stock solution of 1 μm diameter polystyrene microspheres (Polysciences Inc., Warrington, PA). The corresponding number of spheres per cubic micrometer in these phantoms is 0.0131, 0.0073, 0.00364 which were found by applying the relationship in Eq. (3.1). In this equation, N is number of spheres per cubic micrometer, x is particle concentration in gram per milliliter (x = 0.0072, 0.004, 0.002 *g*/ml , respectively), y = 1.05 *g*/*ml* is the density of polystyrene [21,22], and d = 1 μm diameter of sphere in micrometers.

$$N = \frac{6x}{y\pi d^3} \qquad (3.1)$$

Mie theory was used to calculate the scattering coefficients of the microsphere phantoms in the wavelength region 350-650 nm. The numerical calculations for the Mie theory was performed using MATLAB® (Mathworks, Natick, MA) routine which was described elsewhere [23]. This particular script can only perform single wavelength calculations; however, a simple modification was added to enable multi-wavelengths calculations by incorporating the wavelength dependent characteristics of the index of refraction of water

and of the microspheres. The index of refraction of water, n_{water} was calculated using Eq. (3.2) which was derived in previous studies [24, 25]. In Eq. (3.2), λ is the wavelength in nanometers.

$$n_{water}(\lambda) = 1.313 + \frac{15.762}{\lambda} - \frac{4382}{\lambda^2} + \frac{1145500}{\lambda^3} \qquad (3.2)$$

The index of refraction of the polystyrene microspheres, n_{sphere}, was calculated using the Cauchy dispersion relation as shown in Eq. (3.3) [26]. In Eq. (3.3), λ is the wavelength in micrometers.

$$n_{sphere}(\lambda) = 1.5725 + \frac{0.0031080}{\lambda^2} - \frac{0.00034779}{\lambda^4} \qquad (3.3)$$

As a verification of the program, the reduced scattering coefficients for microsphere phantom 0.72% were also calculated with Prof. Prahl's Mie calculator [27]. Since Prof. Prahl's calculator can only perform single wavelength calculations, the comparison with current program was performed at wavelengths with step of 25 nm.

3.3.3 Instruments

Fluorescence measurements of the Intralipid phantoms were performed using an excitation pulsed laser at 355 nm (PNV-001525-140, Teem Photonics, Meylan, France), a single optical fiber with core diameter of 600 μm and numerical aperture of 0.12 for illumination and detection, a calibrated spectrometer (UV-NIR-200, StellarNet Incorporation, Tampa, FL) to record fluorescence at a broadband wavelength range 350-650 nm, and a calibrated acousto-optic-tunable-filter (AOTF) -based time-resolved

spectrometer for estimation of lifetime and verification of fluorescence signals. Details of the time-resolved system can be found elsewhere [28,29]. The advantage of using excitation wavelength at 355 nm in tissue is that most of biological fluorophores such as NADH, collagen, and elastin, etc. can be excited at this wavelength to emit light in visible region.

In all phantom measurements, the fiber tip was held perpendicular to the phantom surface and was immersed within the phantoms at a depth of approximately 2 mm from the surface. The laser power was set at approximately 2.8 μJ and the integrating time of the spectrometer was set at 0.75 second. These values were chosen to maintain good signal for observation while avoiding spectrometer saturation. Background fluorescence was also taken into account by subtracting fluorescence of the phantoms from that of test tube filled with only de-ionized water.

3.4 Results

3.4.1 Scattering of phantoms compared to mucosal tissues

The linear relationship between lipid concentration and μ_s with R-squared values within range of 0.97 and 0.99 was obtained for all wavelengths within 350-650 nm. Figure 3.1 shows examples of linear regressions at 450 nm and 500 nm with R-squared values of 0.98.

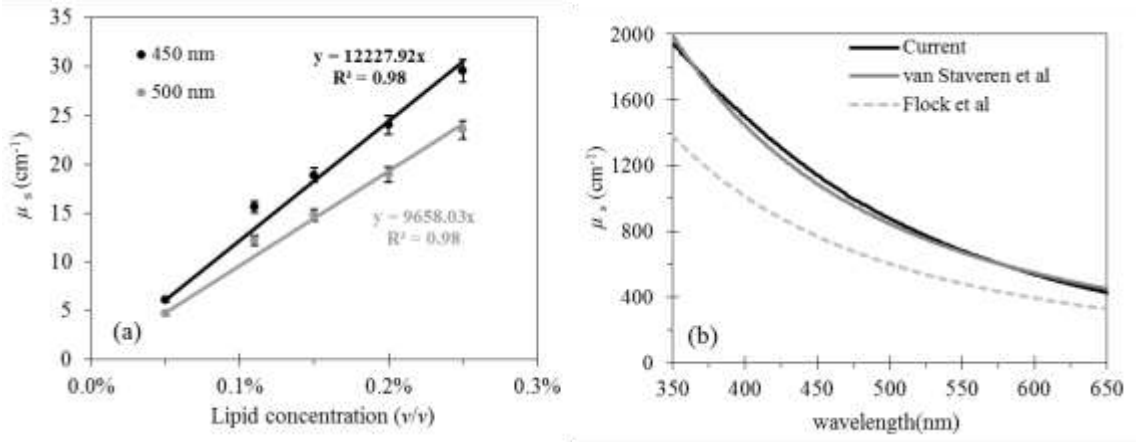

Fig. 3.1 (a) Scattering coefficients (μ_s) as a function of lipid concentration at 450 nm and 500 nm, (b) Predicted μ_s of Intralipid 10%: extrapolated data (current) *vs.* previous literature data by van Staveren *et al.* [30] and Flock *et al.*[31].

The μ_s values of Intralipid 10% was extrapolated using the linear regression method and was compared to previous data reported by van Staveren *et al*.[30] and by Flock *et al*. [31] (Fig. 3.2). As shown in Figure 1b, an agreement (within 10% error) in μ_s values between extrapolated data and the data from van Staveren *et al.* [30] was obtained. Our method of measuring Intralipid's scattering coefficients is quite similar to that of van Staveren *et al*. [30]. The main difference is that the current transmission measurement was performed over broadband wavelength range 350-650 nm with 1-mm-thick quartz cuvette while van Staveren *et al.*'s transmission measurement was performed with lasers (457.9, 514.5, 632.8 and 1064 nm) and 3.55-mm-thick glass cuvette. Therefore, the current method did not require fitting assumption to obtain the scattering spectrum and was able to measure transmission of solution with higher lipid concentration. The current prediction of μ_s of Intralipid 10% was also in agreement with Aernout *et al.*'s prediction which applied invert

adding doubling (IAD) method to predict bulk optical properties from the integrating sphere measurement of total transmission and total reflection from thin slabs [32]. In van Staveren's study, anisotropy (g) was calculated as g = 1.1 - (0.00058) λ, where λ is wavelength in nanometers [30]. In this study, a similar calculation was applied to obtain μ_s' values for Intralipid phantoms from the measured and extrapolated μ_s values.

Comparing with previously reported μ_s' values of mucosal tissue [5,6], it was shown that Intralipid phantoms with lipid concentrations between 0.25% and 0.5% are best for simulation of epithelial scattering while those with lipid concentration between 1.5% and 2% are best for simulation of stromal scattering (Fig. 3.2). Phantoms with lipid concentration 3% and 5% were also produced to further observe the fluorescence trend at high μ_s' values.

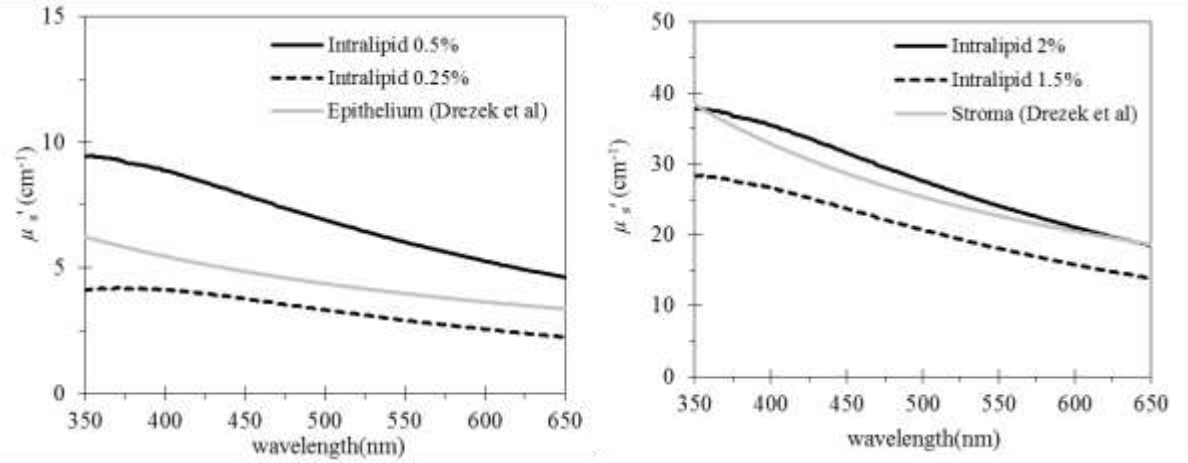

Fig. 3.2 Reduced-scattering coefficients (μ_s'): Intralipid phantoms at different lipid concentration versus literature data [2]

Figure 3.3 compares the current numerical calculation to Prof. Prahl' calculator for scattering coefficients μ_s of microsphere phantom 0.72% (Fig. 3.3a) and the sphere's

anisotropy values g (Fig. 3.3b). An excellent agreement between the two programs with average percentage error less than 0.1% was obtained. As shown in Figure 3b, the anisotropy of 1 μm microsphere is within range of 0.88-0.93 with the peak at around 475 nm.

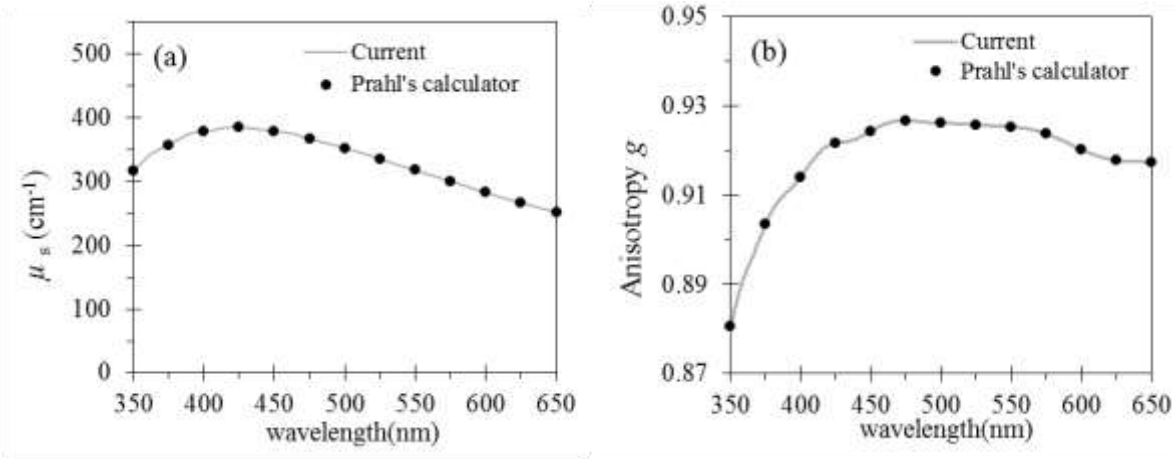

Fig. 3.3 Numerical calculation of Mie theory using current program compared to Prahl's calculator [27]: (a) scattering coefficients of 0.72% microsphere phantom, (b) anisotropy

Figure 3.4 shows the calculated reduced scattering coefficients μ_s' for all microsphere phantoms used. The μ_s' values for mucosal tissues were also plotted in the same graph for comparison. As shown in Fig. 3.4, microsphere 0.72% is optimum for simulation of stromal scattering. The resulted spectrum also agrees with previous experimental measurements with optical fiber spectroscopy and neural networks [19]. The advantage of the current approach over Prof. Pralh's calculator is the ability to calculate broadband spectrum of μ_s and anisotropy g with single input of sphere concentration and sphere diameter. Therefore,

the current method was able to perform fast calculation of μ_s' of the microsphere phantoms over broadband wavelength range 350-650 nm without using fitting approach (Fig. 3.4).

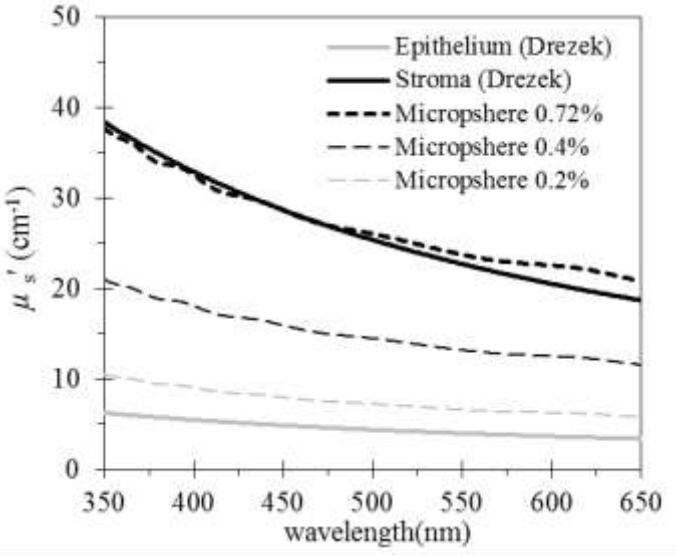

Fig. 3.4 Calculated reduced scattering coefficients (μ_s') of microsphere phantoms versus μ_s' of mucosal tissues.

3.4.2 Fluorescence of Intralipid and Microsphere phantoms

The fluorescent intensity spectrum of Intralipid phantoms collected with the spectrometer between 360-650 nm was shown in Figure 3.5. Background fluorescence was taken into account by subtracting fluorescence of the phantoms to that of test tube filled with only de-ionized water. All error bars shown in these graphs were obtained from standard deviation calculation of measurements of different phantoms with respect to a specific lipid concentration. As shown in Figure 3.5, the fluorescence generally increases gradually from 360 nm to 450 nm with a peak at around 450 nm, and increases more rapidly from 477 nm to 500 nm with a peak at 500 nm. Fluorescence decreases quickly from 525

nm to 650 nm (Fig. 3.5). In these results, the excitation wavelength is not seen because dichroic mirror and filter were used to block back scattered excitation light [28,29].

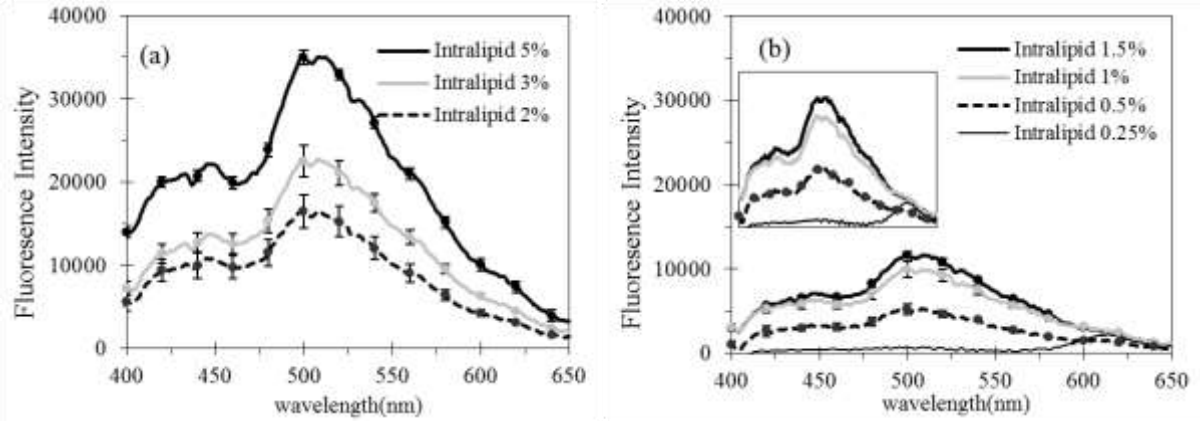

Fig. 3.5 Fluorescent intensity of Intralipid phantoms with different lipid concentrations: 2%, 3%, 5% (a), 0.25%, 0.5%, 1%, and 1.5% (b). The inset in (b) shows auto-scales of the same curves.

Figure 3.5 also shows that increasing lipid concentration from 0.25% to 2% increases fluorescent signals up to seven-fold (14-fold for lipid concentrations up to 5%). To validate the results from the spectrometer, the AOTF time-resolved fluorometer was also used to obtain fluorescent spectra of the lipid phantoms in the wavelength range 400-480 nm. As shown in Fig. 3.6, the trends in the fluorescence emission spectrum from the time-resolved fluorometer is in good agreement with the spectrometer measurements so that lipid 5% produced maximum fluorescent intensity, followed by lipid 3%, 2% and so on .

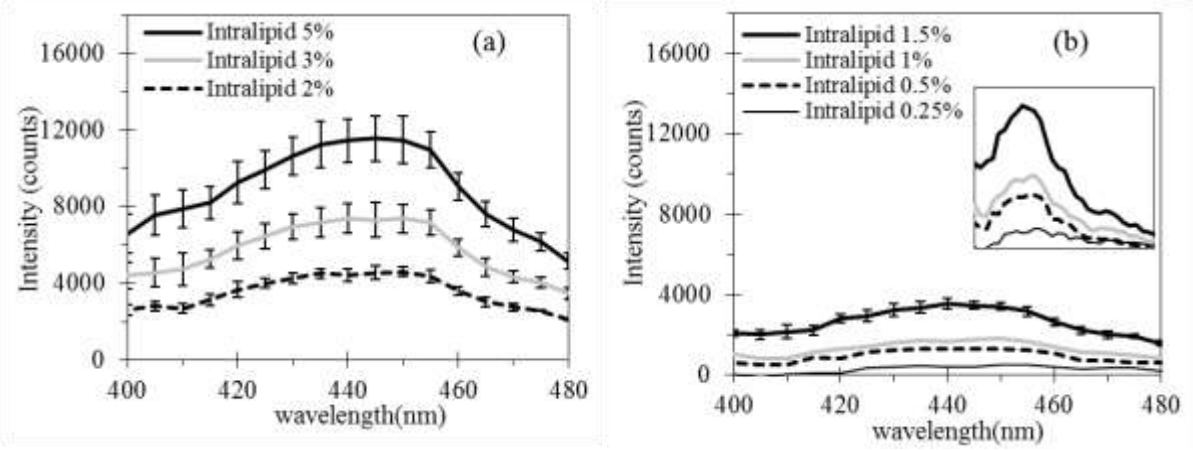

Fig. 3.6 Fluorescent intensity of Intralipid phantoms with different lipid concentration: 2%, 3%, 5% (a), 0.25%, 0.5%, 1%, 1.5% (b). The inset in (b) shows auto-scales of the same curves. Data was collected with a time-resolved fluorometer.

Fluorescent intensity at 450 nm as function of lipid concentration (or reduced scattering coefficients) collected with both systems is plotted on the same graph in Figure 3.7 for demonstration. In Figure 3.7, the fluorescent intensity at 450 nm of the Intralipid phantoms was normalized to that of the Intralipid 5% phantom when using the spectrometer and the AOTF time-resolved fluorometer, respectively. Figure 3.8 shows the fluorescent intensity of the microsphere phantoms measured with the spectrometer [Fig. 3.8(a)] and with the time-resolved fluorometer [Fig. 3.8(b)]. Again, a trend agreement was obtained with both methods so that maximum fluorescent intensity was observed with microsphere concentration of 0.72% (0.0131 sphere per cubic micron), followed by microsphere concentration of 0.4% (0.0073 sphere per cubic micron). The main peak in microsphere fluorescence was seen at 500 nm and was more pronounced at the sphere concentration at 0.72% [Fig. 3.8(a)].

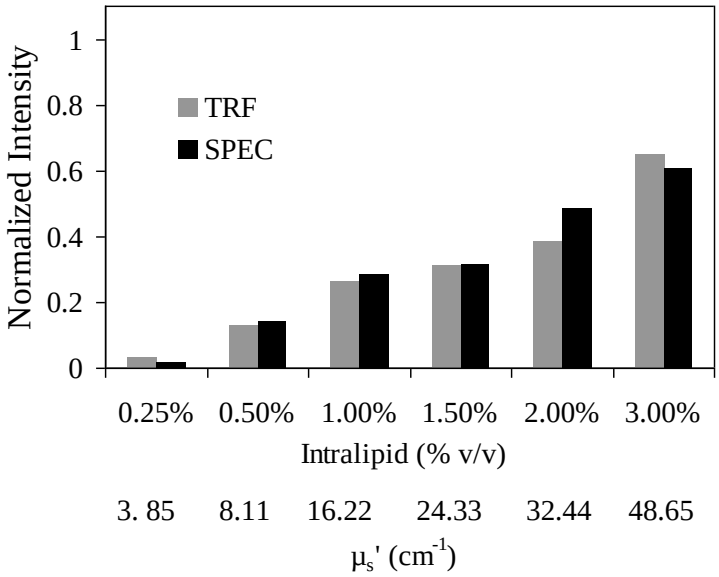

Fig. 3.7 Fluorescent intensity collected with a time-resolved fluorometer (TRF) and spectrometer (SPEC) at 450 nm as a function of lipid concentration or μ_s' values at 450 nm. Intensity of phantoms in each case was normalized to that of phantom with lipid concentration 5%.

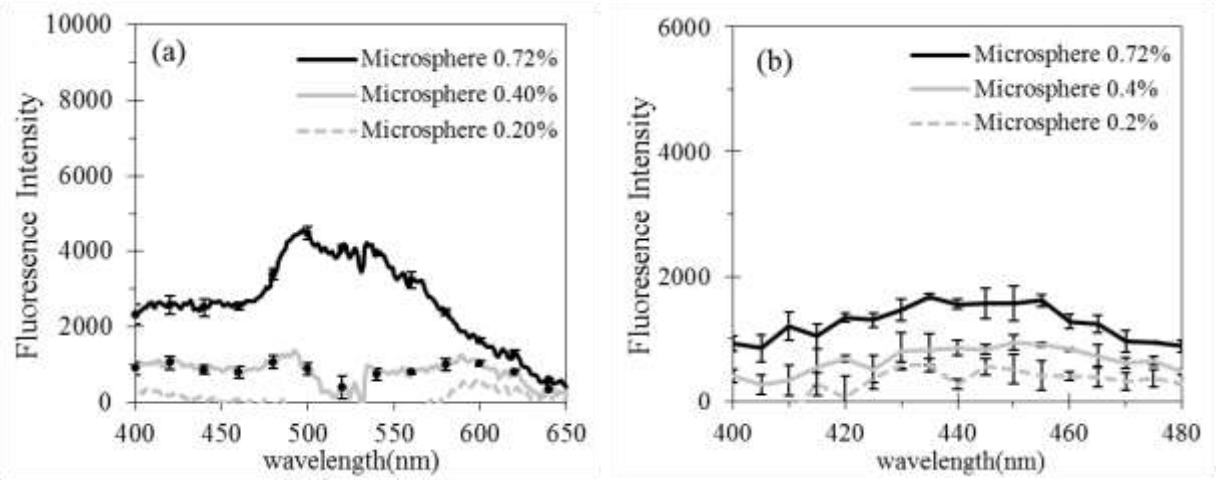

Fig. 3.8 (a) Fluorescence of microsphere phantoms using a spectrometer, and (b) a time-resolved fluorometer.

However, the fluorescent intensity of the 0.72% microsphere phantom is much smaller than that of the 2% Intralipid phantom (Fig. 3.9) while both have similar scattering to that of the stromal layer (Fig. 3.2 and Fig. 3.4). On average, fluorescence of the 2% Intralipid phantom was approximately 3 times stronger than that of the 0.72% microsphere phantom (Fig. 3.9). As shown in Figure 3.9, even the 1.5% Intralipid phantom which has lower scattering than the 0.72% microsphere, 1.5% Intralipid phantom produces fluorescence signals with intensity approximately twice as strong as the 0.72% microsphere phantom (Fig. 3.9).

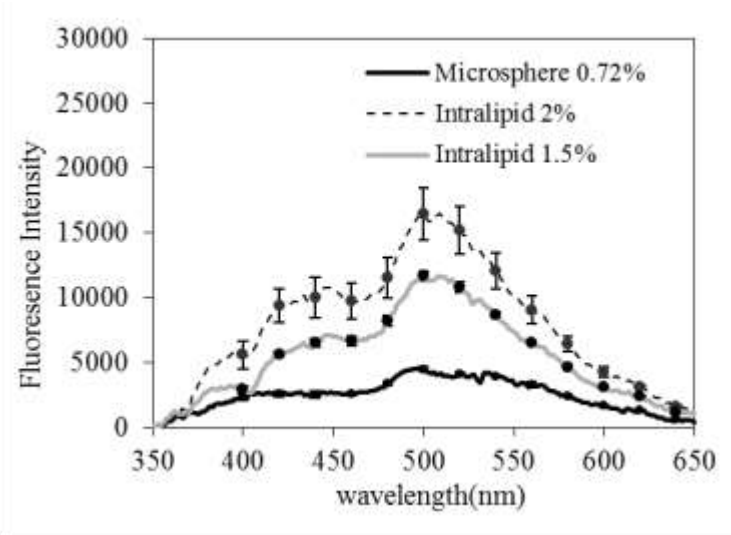

Fig. 3.9 Fluorescence of Intralipid compared to microspheres: The measurements were performed with a spectrometer.

3.4.3 Fluorescence decays of Intralipid and of Polystyrene Microsphere

Fluorescence decays of Intralipid and microsphere phantoms were also recorded with the digitizer for estimation of lifetime. Figure 3.10 shows examples of the normalized fluorescence decays for phantoms with lipid concentration 2% and microsphere 0.72% at

emission peak 455 nm. A bi-exponential deconvolution method was used to retrieve the intrinsic response function from measured fluorescence signals [33]. Based on the fractional contribution of each component [33], an average lifetime of 4.53±0.21 ns and 1.81±0.1 ns was obtained for Intralipid and microspheres, respectively. Similar decays were obtained for phantoms with other lipid and microsphere concentrations. The calculated lifetime (τ) of Intralipid is in the similar range of the lifetime of other visible-emission-dyes used in various fluorescent studies such as Fluorescein (τ = 4 ns), Pyrene (τ = 2.97 ns), 4',6-Diamidino-2-phenylindole or DAPI (τ = 2.78 ns), Rhodamine 123 (τ = 3.97 ns), Alexa 532 (τ = 2.53 ns), and FAD (τ = 2.91 ns) [34]. Therefore, the possibility for Intralipid to interfere with fluorescence measurements of these dyes is high if used together in a tissue phantom.

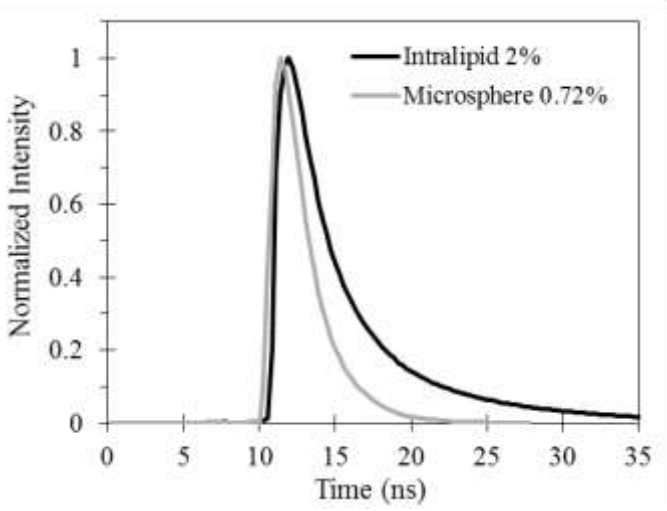

Fig. 3.10 Normalized fluorescence decays of Intralipid phantoms with lipid concentration of 2% and microsphere phantom with sphere concentration of 0.72%.

3.5 Conclusions

These measurements have provided a quantitative measurement of fluorescence of Intralipid and polystyrene microspheres (diameter of 1 μm) in the wavelength range 360-650 nm with consideration of microsphere and lipid concentrations that match μ_s' of human mucosal tissue. It has been shown that Intralipid phantoms have a primary emission peak at 500 nm and a secondary emission peak at 450 nm while microspheres appear to have a single peak around 500 nm. The fluorescence intensity of Intralipid is significantly stronger (average approximately 3-fold) than that of microspheres considering lipid and microsphere concentration at levels which simulate tissue scattering. In addition, the calculated fluorescence lifetime of Intralipid is approximately 2.5 times longer than that of microspheres (4.53 ns vs. 1.81 ns). Most fluorescence dyes used in research strongly fluoresce in region 450-600 nm and have the average life time as close as that of Intralipid. For example, Fluorescein and Rhodamine 123 has strong emission at around 450-500 nm and 520-600 nm, respectively and average life-time of 4 ns and 3.97 ns, respectively [34]. Consequently, the probability for fluorescence of Intralipid to interfere with fluorescence of the studied fluorophore is much higher than that of microspheres. Therefore, the fluorescence of microsphere phantoms might be neglected in optical phantom studies. However, the same assumption may not be accurate in the case of Intralipid phantoms.

In fluorescence studies, background medium consists of pure absorber and pure scatterer which do not fluoresce so that the fluorescence of fluorophore can be studied independently [11-13, 35]. Furthermore, in diffuse reflectance studies the reflected light from the phantoms is usually subtracted to background signal collected from DI water or

instrument's noise [8,19]. However, this method might introduce error if Intralipid is used as scatterer because it fluoresces strongly, and its fluorescence intensity might not be negligible as previously claimed [31]. Therefore, a careful data processing method such as subtraction of average fluorescence response to raw signal [36] is necessary to correctly analyze optical properties and intrinsic fluorescence of the target fluorophore. Although mimicking tissue scattering with low-cost materials is a key factor in the use of Intralipid phantoms, our measurements indicate that fluorescence of Intralipid with lipid concentrations to mimic stromal scattering (1.5 % and 2%) is significant and should not be ignored.

Acknowledgements

The authors would like to thank Prof. Leyla Soleymani of the Department of Engineering Physics at McMaster University for access to her laboratory during phantom fabrication. This project is supported in part by the Natural Sciences and Engineering Research Council (NSERC) of Canada, Canada Foundation for Innovation (CFI), Ontario Ministry of Research and Innovation (MRI), and Canada Canadian Cancer Society Research Institute (CCSRI). QF holds the Canada Research Chair in Biophotonics.

References

1. R. Siegel, E. Ward, O. Brawley, and A. Jemal, "Cancer statistics, 2011: the impact of eliminating socioeconomic and racial disparities on premature cancer deaths," CA Cancer J. Clin. **61**(4), 212–236 (2011).

2. M. Müller and B. H. Hendriks, "Recovering intrinsic fluorescence by Monte Carlo modeling," J. Biomed. Opt. **18**(2), 027009 (2013).

3. K. Vishwanath and M. A. Mycek, "Time-resolved photon migration in bi-layered tissue models," Opt. Express **13**(19), 7466–7482 (2005).

4. Q. Wang, K. Shastri, and T. J. Pfefer, "Experimental and theoretical evaluation of a fiber-optic approach for optical property measurement in layered epithelial tissue," Appl. Opt. **49**(28), 5309–5320 (2010).

5. R. Drezek, K. Sokolov, U. Utzinger, I. Boiko, A. Malpica, M. Follen, and R. Richards-Kortum, "Understanding the contributions of NADH and collagen to cervical tissue fluorescence spectra: modeling, measurements, and implications," J. Biomed. Opt. **6**(4), 385–396 (2001).

6. S. K. Chang, D. Arifler, R. Drezek, M. Follen, and R. Richards-Kortum, "Analytical model to describe fluorescence spectra of normal and preneoplastic epithelial tissue: comparison with Monte Carlo simulations and clinical measurements," J. Biomed. Opt. **9**(3), 511–522 (2004).

7. Y. Chen, A. D. Aguirre, P.-L. Hsiung, S. Desai, P. R. Herz, M. Pedrosa, Q. Huang, M. Figueiredo, S. W. Huang, A. Koski, J. M. Schmitt, J. G. Fujimoto, and H. Mashimo, "Ultrahigh resolution optical coherence tomography of Barrett's esophagus: preliminary descriptive clinical study correlating images with histology," Endoscopy **39**(7), 599–605 (2007).

8. V. N. Du Le, Q. Wang, J. C. Ramella-Roman, and T. J. Pfefer, "Monte Carlo modeling of light-tissue interactions in narrow band imaging," J. Biomed. Opt. **18**(1), 010504 (2013).

9. K. Hazen, J. Welch, S. Malin, T. Ruchti, A. Lorenz, T. Troy, S. Thennadil, and T. Blank, "A Human Tissue Surrogate," WIPO Patent 2001058344 (2001).

10. A. K. Dunn, V. P. Wallace, M. Coleno, M. W. Berns, and B. J. Tromberg, "Influence of optical properties on two-photon fluorescence imaging in turbid samples," Appl. Opt. **39**(7), 1194–1201 (2000).

11. J. Swartling, J. Svensson, D. Bengtsson, K. Terike, and S. Andersson-Engels, "Fluorescence spectra provide information on the depth of fluorescent lesions in tissue," Appl. Opt. **44**(10), 1934–1941 (2005).

12. S. H. Chung, A. E. Cerussi, S. I. Merritt, J. Ruth, and B. J. Tromberg, "Non-invasive tissue temperature measurements based on quantitative diffuse optical spectroscopy (DOS) of water," Phys. Med. Biol. **55**(13), 3753–3765 (2010).

13. G. Wagnières, S. Cheng, M. Zellweger, N. Utke, D. Braichotte, J. P. Ballini, and H. van den Bergh, "An optical phantom with tissue-like properties in the visible for use in PDT and fluorescence spectroscopy," Phys. Med. Biol. **42**(7), 1415–1426 (1997).

14. B. W. Pogue and M. S. Patterson, "Review of tissue simulating phantoms for optical spectroscopy, imaging and dosimetry," J. Biomed. Opt. **11**(4), 041102 (2006).

15. B. S. Suresh Anand and N. Sujatha, "Effects of Intralipid-10% in fluorescence distortion studies on liquid-tissue phantoms in UV range," J. Biophotonics **4**(1-2), 92–97 (2011).

16. N. Rajaram, T. H. Nguyen, and J. W. Tunnell, "Lookup table-based inverse model for determining optical properties of turbid media," J. Biomed. Opt. **13**(5), 050501 (2008).

17. N. Rajaram, T. J. Aramil, K. Lee, J. S. Reichenberg, T. H. Nguyen, and J. W. Tunnell, "Design and validation of a clinical instrument for spectral diagnosis of cutaneous malignancy," Appl. Opt. **49**(2), 142–152 (2010).

18. Q. Liu, C. Zhu, and N. Ramanujam, "Experimental validation of Monte Carlo modeling of fluorescence in tissues in the UV-visible spectrum," J. Biomed. Opt. **8**(2), 223–236 (2003).

19. Q. Wang, D. Le, J. Ramella-Roman, and J. Pfefer, "Broadband ultraviolet-visible optical property measurement in layered turbid media," Biomed. Opt. Express **3**(6), 1226–1240 (2012).

20. S. L. Jacques, "Optical properties of biological tissues: a review," Phys. Med. Biol. **58**(11), R37–R61 (2013).

21. M. Godin, A. K. Bryan, T. P. Burg, K. Babcock, and S. R. Manalis, "Measuring the mass, density, and size of particles and cells using a suspended microchannel resonator," Appl. Phys. Lett. **91**(12), 123121 (2007).

22. S. Stankovich, D. A. Dikin, G. H. Dommett, K. M. Kohlhaas, E. J. Zimney, E. A. Stach, R. D. Piner, S. T. Nguyen, and R. S. Ruoff, "Graphene-based composite materials," Nature **442**(7100), 282–286 (2006).

23. L. V. Wang and H. I. Wu, *Biomedical Optics: Principles and Imaging* (Wiley, 2007), Chap. 2.

24. P. D. T. Huibers, "Models for the wavelength dependence of the index of refraction of water," Appl. Opt. **36**(16), 3785–3787 (1997).

25. X. Quan and E. S. Fry, "Empirical equation for the index of refraction of seawater," Appl. Opt. **34**(18), 3477–3480 (1995).

26. X. Ma, J. Q. Lu, R. S. Brock, K. M. Jacobs, P. Yang, and X. H. Hu, "Determination of complex refractive index of polystyrene microspheres from 370 to 1610 nm," Phys. Med. Biol. **48**(24), 4165–4172 (2003).

27. S. A. Prahl, "Mie Scattering Calculator". *http://omlc.ogi.edu/calc/mie_calc.html*

28. Z. Nie, R. An, J. E. Hayward, T. J. Farrell, and Q. Fang, "Hyperspectral fluorescence lifetime imaging for optical biopsy," J. Biomed. Opt. **18**(9), 096001 (2013).

29. Y. Yuan, J.-Y. Hwang, M. Krishnamoorthy, J. Ning, Y. Zhang, K. Ye, R. C. Wang, M. J. Deen, and Q. Fang, "High throughput AOTF-based time-resolved fluorescence spectrometer for optical biopsy," Opt. Lett. **34**(7), 1132–1134 (2009).

30. H. J. van Staveren, C. J. Moes, J. van Marie, S. A. Prahl, and M. J. van Gemert, "Light scattering in Intralipid-10% in the wavelength range of 400-1100 nm," Appl. Opt. **30**(31), 4507–4514 (1991).

31. S. T. Flock, S. L. Jacques, B. C. Wilson, W. M. Star, and M. J. van Gemert, "Optical properties of Intralipid: a phantom medium for light propagation studies," Lasers Surg. Med. **12**(5), 510–519 (1992).

32. B. Aernouts, E. Zamora-Rojas, R. Van Beers, R. Watté, L. Wang, M. Tsuta, J. Lammertyn, and W. Saeys, "Supercontinuum laser based optical characterization of Intralipid® phantoms in the 500-2250 nm range," Opt. Express **21**(26), 32450–32467 (2013).

33. J. R. Lakowicz, *Principles of Fluorescence Spectroscopy* (Springer, 2006), Chap. 4.

34. M. Y. Berezin and S. Achilefu, "Fluorescence lifetime measurements and biological imaging," Chem. Rev. **110**(5), 2641–2684 (2010).

35. A. Kienle, L. Lilge, M. S. Patterson, R. Hibst, R. Steiner, and B. C. Wilson, "Spatially resolved absolute diffuse reflectance measurements for noninvasive determination of the optical scattering and absorption coefficients of biological tissue," Appl. Opt. **35**(13), 2304–2314 (1996)

36. M. Gao, G. Lewis, G. M. Turner, A. Soubret, and V. Ntziachristos. "Effects of background fluorescence in fluorescence molecular tomography." Appl. Opt **44**, (26): 5468-5474 (2005).

Chapter 4: Paper II - Experimental Recovery of Intrinsic Fluorescence and Fluorophore Concentration in the Presence of Hemoglobin: Spectral Effect of Scattering and Absorption on Fluorescence

Vinh Nguyen Du Le,[a*] Michael S. Patterson,[a,b] Thomas J. Farrell,[a,b] Joseph E. Hayward,[a,b] and Qiyin Fang[c]

[a]McMaster University, Department of Medical Physics and Applied Radiation Sciences, Hamilton, Ontario L8S 4L8, Canada

[b]Juravinski Cancer Centre, Hamilton, Ontario L8V 5C2, Canada

[c]McMaster University, Department of Engineering Physics, Hamilton, Ontario L8S 4L8, Canada

Received Aug. 1, 2015; accepted for publication Nov. 12, 2015; published online Dec. 22, 2015

Published in Journal of Biomedical Optics, **20**(12), 127003- 127003 (2015)
Printed with permission

Introduction to paper II

This paper presented an experimental method that allows rapid retrieval of intrinsic fluorescence and fluorophore concentration. During tissue measurement, fluorescence is likely to be distorted by the presence of absorbers and scatterers in the tissue. This distortion can result in either a change in intrinsic fluorescence intensity or fluorescence spectral shape. Intrinsic fluorescence is an important parameter that may allow the concentration of fluorophore to be determined.

The experimental ideas presented in this paper were inspired by an earlier theoretical study to compensate the effect of hemoglobin absorption in the measured fluorescence. The proposed method was tested on a series of hemoglobin-based phantoms with polystyrene microspheres as background scatterers. The results demonstrated that this method could achieve similar results to previous Monte Carlo based methods. In addition, the manuscript investigated how spectral shape of scatterers and absorbers affect spectral shape of fluorescence. Concentration of Fluorescein was also recovered.

In this paper, I developed the phantom models and carried out all experimental measurements and data analysis. The manuscript was written by me, and edited by Drs. Patterson, Farrell, Hayward, and Fang.

The manuscript has been slightly altered to confront the style of the thesis as whole, such as font, spacing, numbering of pages, equations, and figures and tables.

Contents of paper II

4.1 Abstract

The ability to recover the intrinsic fluorescence of biological fluorophores is crucial to accurately identify the fluorophores and quantify their concentrations in the media. Although some studies successfully retrieved fluorescence spectral shape of known fluorophores, the techniques used usually came with heavy computation cost, and did not apply for strongly absorptive media while the intrinsic fluorescence intensity and fluorophore concentration was not recovered. In this communication, an experimental approach was presented to recover intrinsic fluorescence and concentration of Fluorescein in the presence of hemoglobin (Hb). The results indicated that the method was efficient in recovering the intrinsic fluorescence peak and fluorophore concentration with an error of 3% and 10%, respectively. The results also suggested that chromophores with irregular absorption spectra (e.g. Hb) have more profound effects on fluorescence spectral shape than chromophores with monotonic absorption and scattering spectra (e.g. black India ink, polystyrene microspheres)

Keywords: intrinsic fluorescence signal; hemoglobin; optical properties; diffuse reflectance; fluorescence quantum yield

4.2 Introduction

Many biological fluorophores in human mucosal tissues such as collagen, nicotinamide adenine dinucleotide (NADH), and flavin adenine dinucleotide (FAD) can absorb light at shorter wavelengths (e.g. in the ultraviolet region) and emit fluorescence at longer wavelengths (i.e. in the visible region) [1]. Their fluorescence properties (e.g. intensity and lifetime) and relative concentration can be used to obtain the status of the studied tissues [2-9]. For example, the fluorescence of NADH and FAD may increase as cells become dysplastic due to the disruption of extracellular matrix [2,3] while collagen density or concentration increases during tumor progression [4]. However, during in vivo measurements, background absorbers and scatterers strongly distort the intrinsic fluorescence and make it difficult to obtain the correct concentration of the fluorophore. The term "intrinsic fluorescence signal" (IFS) was adapted by different research groups to describe the fluorescence without the interference of other absorbers and scatters [10-12]. Details of the physical definition of IFS can be found in section 2.3 of the manuscript. In soft tissues, typical absorbers are hemoglobin (primary absorber), collagen crosslinks, NADH and FAD (secondary absorbers) while scatterers include cell nuclei, organelles and collagen fibers [5]. The fluorophore concentration can be extracted only if the effect of absorption and scattering is compensated and the IFS is retrieved.

Many studies have attempted to retrieve the IFS using theoretical modeling, experimental approaches, or a combination of both. For example, Palmer and Ramanujam developed a Monte-Carlo (MC) method incorporated with Mie's theory and a non-linear optimization algorithm to recover the IFS of Furan dye within 10% error [13]. Kanick *et*

al. extended MC algorithms to investigate the effect of absorption on the measured fluorescence intensity but the information regarding intrinsic fluorescence and fluorophore concentration was not recovered [14]. MC algorithms were also used to calculate the optical fiber's calibration factor, which was later used to recover the IFS from the measured diffuse reflectance [12]. Although the MC based method is flexible for different illumination-collection geometries, it requires intensive computation during forward modeling even if modern computational power is applied [15-21]. Therefore, it is necessary to develop a simpler approach that can perform fast recovery of fluorescence and can be adapted to different systems. In Diamond *et al*.'s studies, the fluorophore concentration was extracted by applying diffusion theory for the measured fluorescence and diffuse reflectance [22]. However, optical properties extraction based on the diffusion approximation may not be accurate for tumorous tissues with high angiogenesis (such as glioblastoma) or for intraoperative surgery where bleeding is unavoidable. In such case, absorption level usually dominates scattering level and diffuse approximation becomes inapplicable [23].

Finlay and Foster used a forward adjoint model of fluorescence to recover the shape of intrinsic fluorescence spectra and hemoglobin absorption with the prior knowledge of concentration of known absorbers, and of known fluorophore [24]. The approach, however, was not able to retrieve the absolute fluorescence intensity and fluorophore concentration [24]. In studies by Kim *et al*., an analytical method was developed to correct the fluorescence line shape and fluorophore concentration based on the assumption that fluorescence is in a linear relationship with diffuse reflectance at emission wavelengths [25]. However, such an assumption is valid only if an excitation wavelength within 380-

450 nm is used so that the migration path of emitted photons is approximately the same as that of reflected photons [25]. Furthermore, previous phantom studies considered Furan 2 as the fluorophores [12] and red marking dye as the background absorber [16]. Such materials are not relevant to most of tissues investigations and the fluorescence intensity and fluorophore concentration was not recovered. For example, Furan 2 has an emission peak at 400-420 nm while many endogenous fluorophores such as NADH, FAD, and elastin have emission peaks at longer wavelengths (450-550 nm) [1]. Hoy *et al.* attempted to recover intrinsic fluorescence line shape of Fluorescein based on the recovered optical properties with the single fiber fluorescence (SFF) technique [26]. However, the fluorescence intensity and fluorophore concentration were not recovered for comparison. Moreover, the validation of SFF was performed on phantoms with high concentration of Intralipid while using 365 nm as the excitation source [26]. A recent report has shown that Intralipid fluoresces strongly at this concentration and has longer fluorescence lifetime (4.5 ns) if compared to Fluorescein (4.8 - 4 ns) [1,27]. Therefore, its fluorescence properties should not be ignored. Although different studies were able to recover the intrinsic fluorescence and concentration of Protoporphyrin IX (PpIX) in the human skin using excitation light at longer wavelengths from 600-800 nm [28-30], many fluorophores in human mucosa and brain such as NADH, FAD, and collagen absorb light at shorter wavelengths from 350-500 nm [1]. Therefore, additional evaluations on phantoms or tissues with hemoglobin as the dominant absorber are necessary if these approaches [28-30] are to be applied to image mucosal tissues or brain tissues.

In this paper, we explored the ability of a simpler approach [31] for fast recovery of fluorescence peaks and fluorophore concentration in highly absorptive media using excitation wavelength at 355 nm. The approach was validated on tissue-simulating phantoms using Fluorescein as fluorophore, polystyrene microspheres as background scatterers, and black India ink and Ferrous-stabilized hemoglobin as background absorbers.

4.3 Methods

4.4.1 Tissue simulating phantoms

Stock solution of Fluorescein with a concentration of 10^{-3} M was prepared by dissolving Fluorescein powder (46955-100G-F, Sigma-Aldrich, MO) in concentrated ethanol 95% (Commercial Alcohols, GreenField Specialty Alcohol Inc., ON). Fluorescein concentrations of 10^{-4} and 10^{-5} M were prepared by simply diluting the stock solution in DI water. The absorption and emission spectra of Fluorescein are extremely sensitive to the alcohol residue and careful sample preparation is necessary to obtain accurate measurements [27]. To simulate tissue scattering, polystyrene microspheres with diameter of 1 μm (07310-15, Polysciences Inc., PA) were used. These spheres were preferred because their scattering properties are similar to biological tissues, their well-controlled size and index of refraction [17,18,32], and accurate estimation of scattering properties calculated using Mie theory [33-35]. To investigate the effect of scattering on fluorescence, six phantoms (S1 to S6) with six different concentrations of microspheres (from 0.05 % to 0.72% w/v) were created. These concentrations were obtained by diluting the original concentration of 2.65% w/v in deionized water [27].

To simulate tissue absorption, both black India ink (Higgins Ink, Chartpak Inc., MA) and hemoglobin (H0267, Sigma-Aldrich, MO) were used. Black India ink is widely used to simulate absorbers in tissue optics because of its similar exponential decrease of absorption with wavelength as that of NADH and FAD, its low cost, spectral stability, and low-fluorescence activity [2,5,36-40]. Applying the same assumption made by previous studies [38,40], the current study treated India ink as a pure absorber. Absorption and scattering coefficients of black India ink and microspheres are shown in section 4.4.2. Ferrous-stabilized hemoglobin was selected because its absorption spectrum is close to that of human blood [18], and due to its high and stable oxygen saturation (~ 100%) [33,41]. Absorption coefficients of hemoglobin phantoms are shown in section 4.4.1. A stock solution with hemoglobin concentration of 30 mg/ml was prepared by diluting Hb powder in DI water.

To observe the effect of hemoglobin absorption on fluorescence, three phantoms with hemoglobin concentration of 3.5, 10 and 20 mg/ml (Hb3.5, Hb10, Hb20) and microsphere concentration of 0.4% *w/v* were produced. To investigate the effects of secondary absorbers on fluorescence, five phantoms (I1 to I5) with various India ink concentrations (0.05% to 0.6%) and microsphere concentration of 0.72% *w/v* were created. In all phantoms, optical properties were controlled and calculated by applying Beer-Lambert's Law to the absorbance of pure solute absorbers (Fluorescein, India ink or Hemoglobin) measured with a spectrophotometer (Ultraspec 3000, Pharmacia Biotech Inc., NJ) for absorption coefficient (μ_a) and Mie theory for reduced scattering coefficient (μ_s'). Scattering anisotropy (g) of polystyrene microsphere can be found in previous study [27]. Volume

and depth of each phantom was 6 ml and 5.5 cm, respectively. Each phantom was contained in a test tube with diameter of about 12 mm.

4.4.2 Instrumentation

Diffuse reflectance (DR) signal from the phantoms was generated using a broadband light source (Dolan-Jenner MI-150, Edmund Optics, NJ) for illumination while steady state fluorescence (SSF) signal was generated using a solid-state laser (PNV-001525-140, Teem Photonics, Meylan, France) at 355 nm with 300 ps full width at half maximum (FWHM) for excitation. Measurements of both DR and SSF signals were performed with the same customized optical probe [42]. Fig. 4.1 shows the geometry of optical probe, including a diffuse reflectance /steady-state fluorescence (DR/SSF) source fiber, different DR/SSF detection fibers bundled into three groups at three source-detector distances (SDD) of 0.23, 0.59, and 1.67 mm, and a center fiber for time-resolved fluorescence (TRF) measurement. Three spectrometers (UV-NIR-200, StellarNet Incorporation, Tampa, FL) were used to record the reflectance signal and steady state fluorescence signal and were controlled by a moderately equipped computer (IBM Core 2 Duo L7500, 2 GB RAM). The position of the fiber probe was unchanged during both measurements. This enabled the correction of fluorescence using the diffuse reflectance measured at the same location.

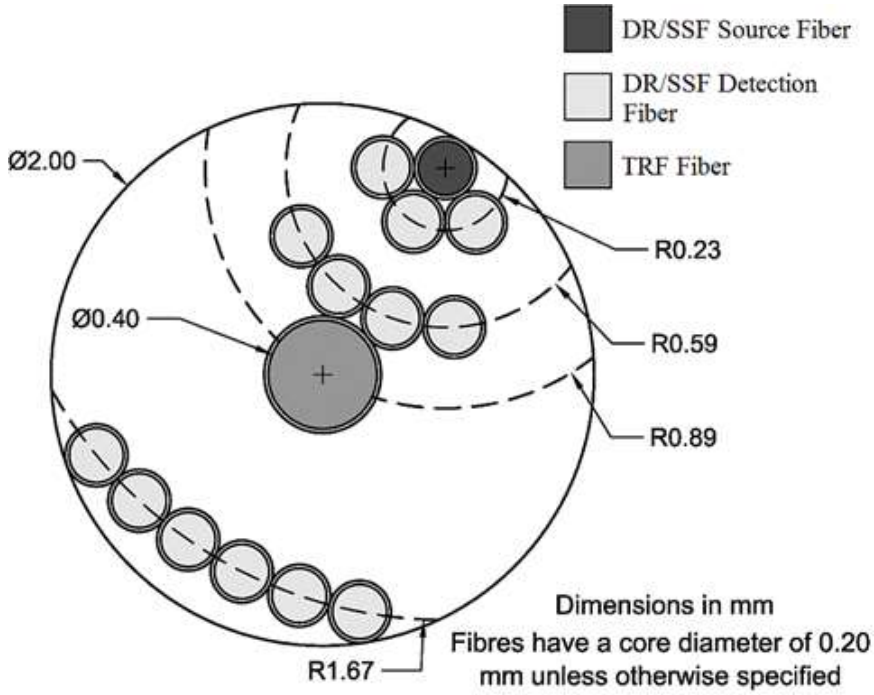

Fig. 4.1 Schematics of the fiber probe geometry. Diffuse reflectance/steady-state fluorescence (DR/SSF) detection fibers are bundled together into three groups, each at the indicated distance (0.23, 0.89, 1.67 mm) from the DRS/SSF source fiber (measured from the centers of each fiber). In addition, a central fiber was used for time-resolved fluorescence (TRF) spectroscopy measurements. Diameter of DR/SSF fibers is 200 μm and of the TRF fiber is 400 μm

Later, the fluorescence lifetime of Fluorescein in each phantom was recorded using center optical fiber with core diameter of 400 μm and numerical aperture of 0.12 (Fig. 4.1), and a calibrated acousto-optic-tunable-filter (AOTF)-based time-resolved spectrometer [43]. Details of the time-resolved system can be found elsewhere [43,44]. In all measurements, the fiber-optic probe was held perpendicular to the phantom surface and slightly touched the phantoms. The time-resolved measurements merely served as a secondary verification of the stability and the consistency in fluorescence properties of

Fluorescein in all phantoms (the primary verification was spectrometer measurement of absorbance spectra), and had no role in retrieving Fluorescein concentration. In the current study, experimental measurements with India ink and microspheres were performed on different days with different batches and concentrations of Fluorescein. Therefore, a consistency in our time-resolved measurements would also ensure that the use of additional absorbers and scatterers does not alter the chemical structure of Fluorescein, and that the same alcohol concentration was present in all the phantoms.

4.4.3 Retrieving of intrinsic fluorescence

When the excitation light with intensity I_x was used to illuminate the sample, fluorescence was emitted with a spectral distribution $f_{xm}(\lambda_m)$. However, due to absorption and scattering in the tissue sample, only a fraction of f_{xm}, defined as $F_{xm}(\lambda_m)$, was collected. The subscripts x and m indicate the dependence of the quantity on excitation and fluorescence emission wavelengths (λ_x and λ_m), respectively. Hence, F_{xm} and f_{xm} represents the measured fluorescence and intrinsic fluorescence at emission wavelength m due to excitation wavelength x, respectively. Müller *et al.* and Zhang *et al.* defined f_{xm} as the total fluorescence intensity of a thin slab of thickness l (cm) of a material that does not absorb nor scatter photons while containing the same concentration of fluorophores [12,16,31]. In a closed form, f_{xm} can be written in terms of Eq. (4.1) where μ_{afx} is the absorption coefficient (cm^{-1}) due only to the slab's fluorophore at excitation wavelength x, and ϕ_{xm} (dimensionless) is the fluorescence quantum yield [12,16,31].

$$f_{xm} = \frac{\lambda_x}{\lambda_m} I_x l \mu_{afx} \phi_{xm} \qquad (4.1)$$

In Eq. (4.1), ratio λ_x/λ_m corrects for the difference in photon energy at excitation and emission wavelength while the product $l\mu_{afx}$ (<< 1) represents the probability of a photon at excitation wavelength λ_x to be absorbed by the fluorophore, and ϕ_{xm} represents the probability of a photon at emission wavelength λ_m to be generated after the absorption event at λ_x. Because μ_{afx} can be defined as $c\varepsilon\ln(10)$ where c is fluorophore molar concentration (M) and ε extinction coefficient ($cm^{-1}. M^{-1}$) at λ_x. Because f_{xm} directly relates to c, Eq. (4.1) can be re-written in form of Eq. (4.2) with a consideration of a mixture of i fluorophores:

$$f_{xm} = \frac{\lambda_x}{\lambda_m} I_x l \ln(10) \sum_i \varepsilon_i c_i \phi_{xm}^i \qquad (4.2)$$

By using the escape probability distribution function (ρ), the phase-function dependence of the scattering was separated from the scattering and absorption coefficients, and the diffuse reflectance (R) and the measured fluorescence (F_{xm}) can be modeled using Eq. (4.3) and (4.4) [12,31].

$$R = \sum_{n=1}^{\infty} \rho_n w_n \qquad (4.3)$$

$$F_{xm} = \frac{\lambda_x}{\lambda_m} I_x \sum_{n=1}^{\infty} \sum_{i=0}^{n-1} \rho_{ni} w_{ni} \qquad (4.4)$$

, where $w_n = a^n = \left(\frac{\mu_s}{\mu_a + \mu_s} \right)^n$, $w_{ni} = a_x^{i+1} \frac{f_{xm}}{l\mu_{sx}} a_m^{n-i-1}$ and $\rho_n = R_0 (e^{S(1-g)} - 1) e^{-nS(1-g)}$

In Eq. (4.3) and (4.4), n is the number of scattering events (dimensionless), S is a constant calibration factor for each individual fiber (dimensionless), w is the photon weight (dimensionless), a is the albedo (dimensionless), μ_a is the absorption coefficient (cm^{-1}), μ_s is the scattering coefficient (cm^{-1}), g is the anisotropy parameter (dimensionless), and R_0 is the diffuse reflectance from a standard sample containing only scattereres (dimensionless).. By combining the expressions of R and F_{xm} into Eq. (4.1), a relationship between f_{xm} and F_{xm} can be written as Eq. (4.5).

$$f_{xm} = \frac{\mu_{sx} * l * F_{xm}}{\left(\frac{R_{0x}R_{0m}}{\left(e^{S(1-g_x)}-1\right)\left(e^{S(1-g_m)}-1\right)}\right)^{1/2} \frac{R_{tx}}{R_{0x}}\left(\frac{R_{tm}}{R_{0m}} + \left(e^{S(1-g_m)}-1\right)\right)} \qquad (4.5)$$

In Eq. (4.5), R_t is the diffuse reflectance from the targeted samples. In the studied phantoms, μ_s and g were obtained by applying Mie theory for specific microsphere diameter and concentration [27]. To calculate the diffuse reflectance R, the measured reflectance intensity of the sample, $I_{r,sample}$, was normalized to the reflectance intensity of a standard spectralon sample with 99.9% reflectivity, $I_{r,std}$ (Labsphere, Inc., NH, USA) after subtracting the background signal intensity, $I_{r,bg}$. This method is described via Eq. (4.6).

$$R = \frac{I_{r,sample} - I_{r,bg}}{I_{r,std} - I_{r,bg}} \qquad (4.6)$$

The retrieved signal f_{xm} in Eq. (4.5) can be used to recover the concentration of fluorophore for a known value of ϕ_{xm}. In the current study, fluorescence quantum yield of Fluorescein in basic ethanol was assumed to be 0.97 at emission peak [45,46]. In experimental measurement, due to strong intensity of laser a neutral density filter with

optical density of two and a short exposure time (~ 1 ms) was applied when measuring I_x to avoid saturation at spectrometers. Therefore, to enable accurate estimation of c from Eq. (4.2) a correction factor k was applied so that $k = 10^{-2}(1/1130)$, where 1/1130 is the ratio of exposure time used for I_x and that for F_{xm} (or f_{xm}). The concentration c of Fluorescein in the phantom can be experimentally estimated in Eq. (4.7).

$$c = k \frac{f_{xm}\lambda_m}{I_x \lambda_x l \varepsilon \phi_{xm} \ln(10)} \qquad (4.7)$$

To obtain the calibration factors l and S in Eq. (4.5), the least squares fitting routine fminsearch() in MATLAB® was used to fit the measurement of f_{xm} (from the reference non-scattering phantom), F_{xm} and R_{xm} of calibration phantoms into Eq. (4.5). This optimization method is based on the Nelder-Mead simplex algorithm and has been used widely for spectral analysis in spectral imaging [47-49]. In the fitting routine, the ideal intrinsic fluorescence f_{xm} was measured directly on a phantom consisting solely of Fluorescein 10^{-4} M (in DI water) while F_{xm} and R_{xm} were measured with phantoms consisting of Fluorescein 10^{-4} M and various India ink and microsphere concentrations. To simplify the fitting routine, l was set at 1 cm. Fitting routines for known spectra of f_{xm} , F_{xm} and R_{xm} yielded values of 54.6, 45.5 and 48.2 for fibers with an SDD of 0.23, 0.59 and 1.67 mm, respectively. These S values were later used to retrieve f_{xm} in hemoglobin phantoms.

Similar to previous methods [12,31], the current method utilized the ideas that enabled the retrieving of intrinsic fluorescence from the measured diffuse reflectance. The main difference lies upon the calibration approaches. The current method incorporated the system characteristics such as light source intensity and position of the fiber probe into the

calibration. Therefore, the current method enabled recovery of absolute fluorescence intensity via Eq. (4.5) and of fluorophore concentration via Eq. (4.7) while the previous methods could recover only the relative fluorescence intensity and spectral shape.

4.4 Results

4.4.1. Effect of hemoglobin absorption on fluorescence

Fig. 4.2 shows μ_a of hemoglobin (Hb) and Fluorescein, as well as μ_s' of polystyrene micropsheres used in the hemoglobin-based phantoms (Hb3.5, Hb10, Hb20). In these phantoms, the concentration of Fluorescein and microspheres remained the same while hemoglobin concentration was varied. The inset of Fig. 4.2(b) shows that the measured μ_a was in excellent agreement with reference μ_a values for Fluorescein 10^{-4} M in alcohol [45,50]. The reference μ_a was calculated by multiplying Fluorescein concentration to that of its tabulated molar extinction coefficients [50]. As indicated elsewhere, a hemoglobin concentration of 3.5 mg/ml best simulates back-ground absorption in mucosal tissue [18]. In addition, a microsphere concentration of 0.4% w/v (~ 0.0073 spheres per cubic micrometer) was used to simulate background scattering.

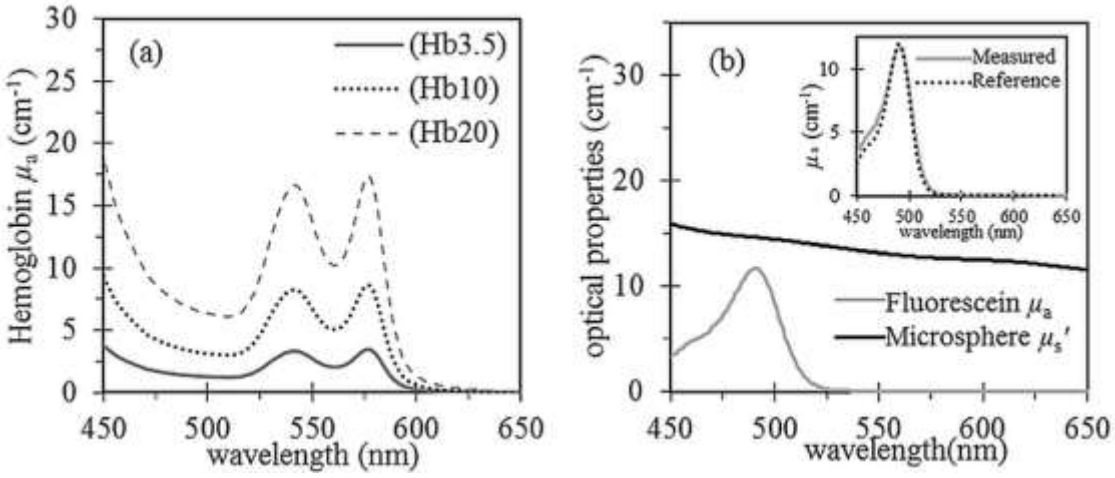

Fig. 4.2 (a) Absorption coefficients μ_a of hemoglobin phantoms (Hb3.5: 3.5 mg/ml), (Hb10: 10 mg/ml), (Hb20: 20 mg/ml) as a funcion of wavelength, and (b) reduced scattering coefficients μ_s' of polystyrene microspheres and μ_a of Fluorescein as a function of wavelength. In these phantoms, the concentration of microsphere and Fluorescein was kept constant at 0.4% w/v and 10^{-4} M, respectively. The inset in (b) compares μ_a of Fluorescein 10^{-4} M measured in the current study ("Measured") to that extracted from the literature ("Reference") [50]

Fig. 4.3(a) shows the measured steady state fluorescence (F_{xm}) from three phantoms using SDD of 0.59 mm. Due to the similarity in the measured fluoresence spectra at different fibers, only the signal at one fiber is shown [Fig. 4.3(a)]. In general, increasing absorption (from 4.5 to 20 mg/ml) decreases the measured fluorescence intensity due to the decrease in the number of emitted photons escaping to the tissue surface. To compare the spectral shapes, the fluorescence spectrum of Fluorescein in DI water (instrinsic) and in hemoglobin and microspheres (distorted) is shown in the same graph [Fig. 4.3(b)]. As shown in Fig. 4.3(b), the spectral shape of the measured fluorescence was highly distorted in the wavelength regions where hemoglobin strongly absorbs photons (540 nm and 580

nm). Fig. 4.3(c) shows examples of the absorption dependence of the measured fluorescence at the Fluorescein emission peak of 520 nm.

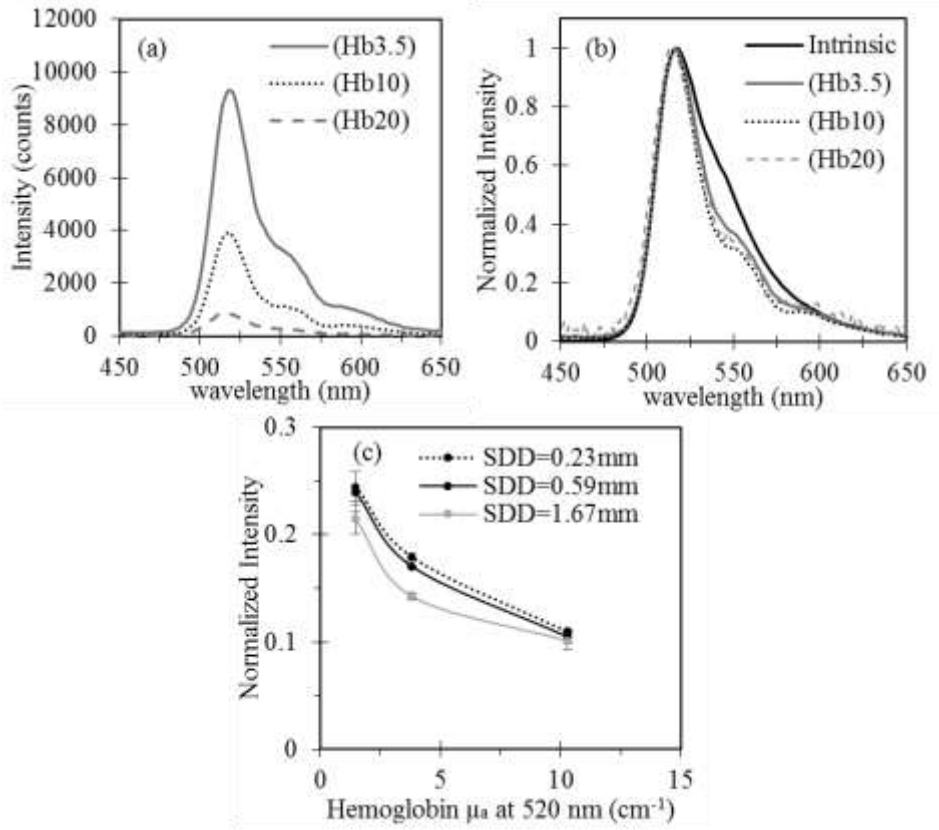

Fig. 4.3 (a) Measured fluorescence (F_{xm}) of phantoms (Hb3.5), (Hb10) and (Hb20), (b) normalized emission spectra, (c) and normalized intensity as a function of μa at the emission peak 520 nm for all three collection distances. In (c), the intensity at the emission peak of phantoms was normalized to that of the sample consisting solely of Fluorescein 10^{-4} M in DI water (intrinsic). In all cases, the concentration of Fluorescein was 10^{-4} M and microsphere was 0.4% *w/v*, respectively, and SDD of 0.59 mm was used.

Despite the distortion in the measured steady-state fluorescence, it was observed that average lifetime in the phantoms remains unchanged, indicating that lifetime was not affected by background absorption (Fig. 4.4). A bi-exponential deconvolution method was

used to obtain the lifetime information of the measured fluorescence signals [43]. Fig. 4.4(a) shows that fluorescence lifetime is consistent at the emission wavelength for a phantom with Hb concentration of 3.5 mg/ml. In addition, Fig. 4.4(b) shows that the fluorescence lifetime of Fluorescein in hemoglobin phantoms agreed with that of intrinsic signal within one standard deviation. In Fig. 4.4(b), the fluorescence lifetime was averaged over six repeated measurements, and standard deviations were calculated and shown as error bars.

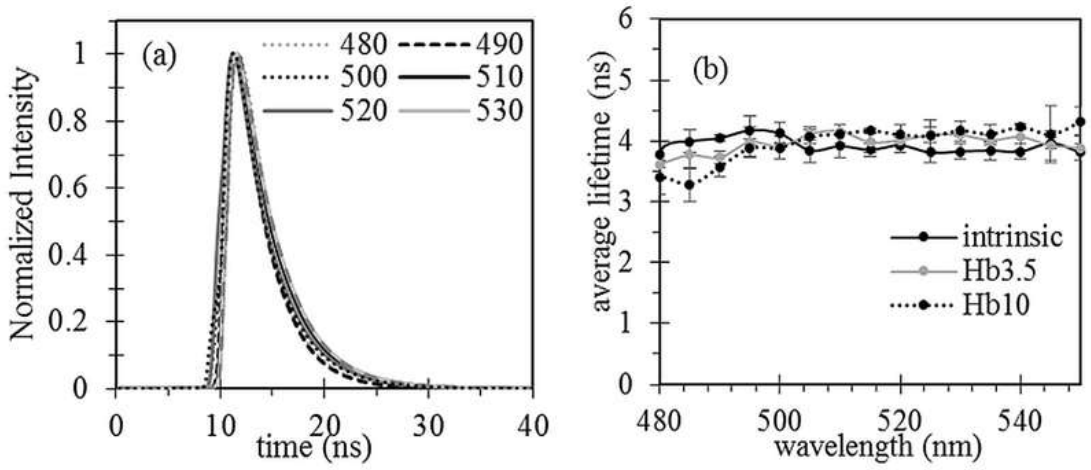

Fig. 4.4 (a) Fluorescence lifetime for phantom (Hb3.5) at selected emission wavelengths and (b) average fluorescence lifetime of the phantoms (Hb3.5) and (Hb10). The intrinsic signal was collected using Fluorescein 10^{-4} M in diluted ethanol without additional scatterer or absorber.

Figure 4.5(a) shows the corresponding diffuse reflectance of three hemoglobin-based phantoms using SDD of 0.59 mm. In general, the drops of reflectance at 540 nm and 580 nm regions were due to hemoglobin absorption in these regions [Fig. 4.2(a)] while the drop at 470-520 nm was mainly due to Fluorescein absorption [Fig. 4.2(b)]. Fig. 4.5(b) and Fig. 4.5(c) compare the measured fluorescence (F_{xm}) to that of recovered and intrinsic

fluoresence for a phantom with Hb concentration of 3.5 mg/ml using SDD of 0.59 mm. The recovered fluoresence (f_{xm1}) is fluorescence signal calculated using Eq. (4.5). The least square fitting routine fminsearch() was also applied to fit f_{xm1} to the shape of the intrinsic spectrum (ideal) and obtain the fitted spectrum , f_{xm2}, of f_{xm1}. The square errors between f_{xm1} and f_{xm2} were used to optimize the results of the fitting. Figure 4.5(d) compares the percentage difference between F_{xm}, f_{xm1} and f_{xm2} with respect to the ideal intrinsic fluorescence for phantom Hb3.5 (hemoglobin concentration of 3.5 mg/ml).

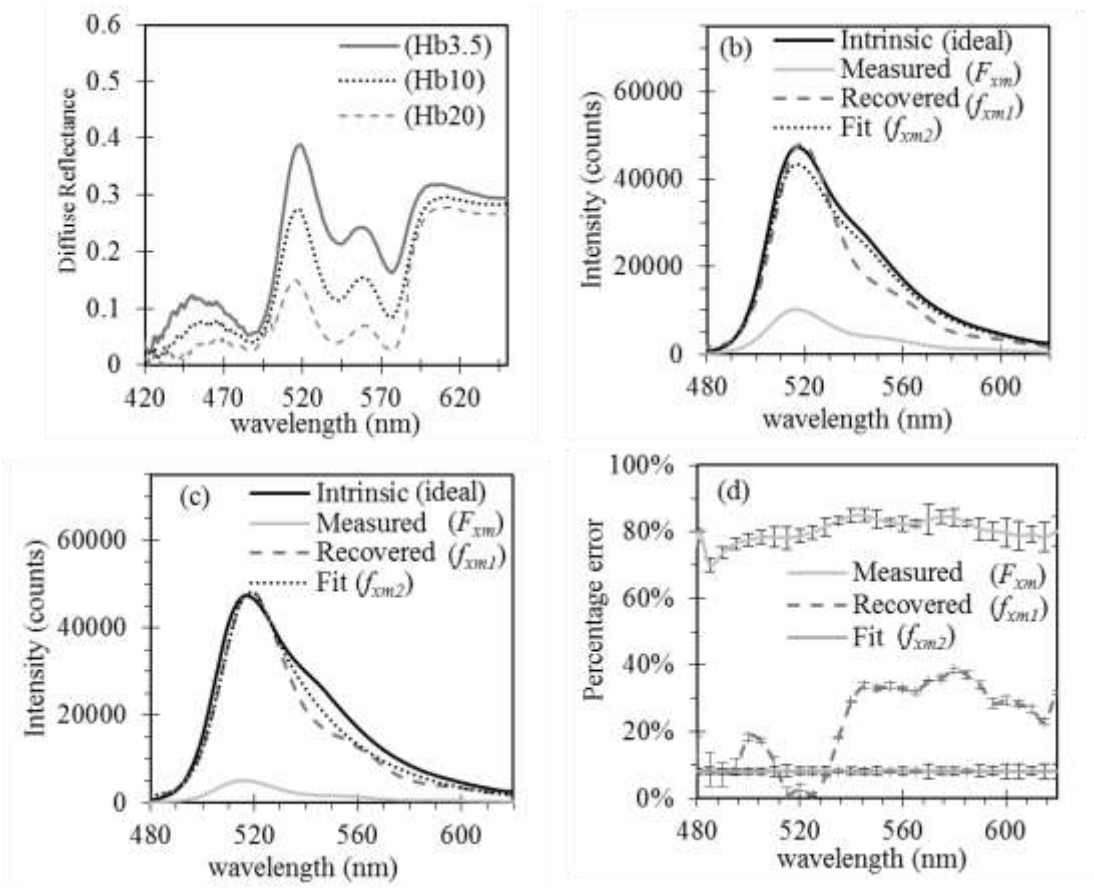

Fig. 4.5 (a) Diffuse reflectance of the phantoms (Hb3.5), (Hb10) and (Hb20); (b) Measured fluorescence (F_{xm}), the retrieved fluorescence (f_{xm1}), the fitted fluorescence (f_{xm2}) and the ideal intrinsic fluorescence for phantom with Hemoglobin concentration of 3.5 mg/ml, and (c) of 10 mg/ml; (d)

Absolute percentage difference in signal intensity with respect to the ideal intrinsic signal for Hb3.5 phantom. In all cases, Fluorescein concentration of 10^{-4} M, microsphere concentration of 0.4% *w/v*, and SSD of 0.59 mm was used. In (b and c), F_{xm} is fluorescence under influence of hemoglobin absorption and microsphere scattering while f_{xm1} is the recovered fluorescence using Eq. (4.5), f_{xm2} is the fitted spectrum of f_{xm1}, and the intrinsic signal is the signal measured in ideal conditions in which the phantom consists solely of Fluorescein 10^{-4} M in DI water.

On average over 480-620 nm, the percentage error was approximtely 81%, 24% and 8% for F_{xm} , f_{xm1} and f_{xm2}, respectively. These numbers were (91%, 26%, 9%) and (99%, 30%, 13%) for phantom Hb10 and Hb20, respectively (Table 4.1). On average over 480-620 nm, the accuracy of the signal was improved by 70% without fitting and by 90% with fitting. Considering only peak emission at 522 nm, percentage errors of F_{xm}, f_{xm1} and f_{xm2} are 79%, 3% and 8%, respectively. The recovered fluorescence at 522 nm was used to calculate the concentration of Fluorescein using Eq. (4.7). With x of 355 nm (excitation peak) and m of 522 nm (emission peak), the value of I_{355} and of $f_{355,522}$ is 61225 counts and 45093 counts, respectively. Extinction coefficient ε_{355} of Fluorescein was assumed to be 0.04 cm^{-1}. M^{-1} [50], and $\phi_{355,522}$ was assumed to be 0.97 [45]. Therefore, *c* value of $1.07*10^{-4}$ M was estimated using Eq. (4.7). Table 4.2 summarizes the extracted concentration of Fluorescein in three Hb phantoms. On average, the extracted concentration was within 10% of the controlled value of 10^{-4} M.

Table 4.1 Average percentage difference (AVG) of F_{xm}, f_{xm1}, f_{xm2} with respect to the ideal intrinsic fluorescence over 490-620 nm. Analysis for all three phantoms (Hb3.5, Hb10, Hb20) is shown.

Quantity	Percentage error (%) for each phantom		
	Hb3.5	Hb10	Hb20
F_{xm}	80.8±2.7	91.3±1.8	98.7±0.4
f_{xm1}	24.1±12.4	26.3±11.4	29.6±11.1
f_{xm2}	8.1±1.5	8.5±0.8	12.8±1.1

Table 4.2 The recovered Fluorescein concentration (c) in three hemoglobin phantoms from Eq. (4.5). The controlled concentration of Fluorescein in these phantoms was 10^{-4} M.

Quantity	Phantom		
	Hb3.5	Hb10	Hb20
$f_{355,522}$ (counts)	45,093±786	49,958±232	44,174±317
$F_{355,522}$ (counts)	9472±165	4527±21	557±4
***c* (M)**	**1.07E-04 ±4E-06**	**1.19E-04 ±2.E-6**	**1.05E-04 ±2.E-06**

4.4.2 Effect of India ink absorption on fluorescence

To further investigate the absorption effect on fluorescence, black India ink with increasing concentration from phantom I1 to I5 was used to simulate background absorption while a microsphere concentration of 0.72% was used to simulated background scattering. Fig. 4.6 summarizes the optical properties of the phantoms used in this section. The goal of this subsection is to investigate the effects of a monotonic decreasing

absorption on fluorescence intensity and spectral shape, and to compare it to the hemoglobin cases.

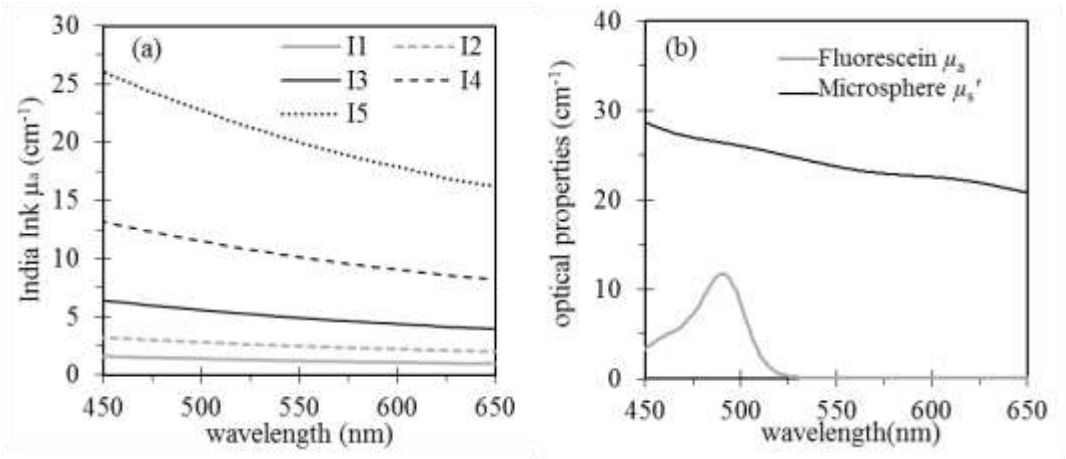

Fig. 4.6 (a) Absorption coefficients, μ_a, of the India ink in phantoms I1 to I5 as a funcion of wavelength, and (b) reduced scattering coefficients, μ_s', of polystyrene microsphere and μ_a of Fluorescein as a function wavelength. In these phantoms, the concentration of India ink increases from phantom (I1) to (I5) while the concentration of microsphere and the Fluorescein was kept constant at 0.72% w/v and 10^{-4} M, respectively

Fig. 4.7(a) summarizes the measured fluorescence (F_{xm}) from phantom I1 to I5 while Fig 4.7(b) compares the spectral shape of F_{xm} and f_{xm} , and Fig 4.7(c) summarizes the corresponding *R*. These data were collected at SDD = 0.59 mm. A similar trend to that of Fig. 4.3(a) was observed in Fig. 4.7(a): steady state fluorescence decreases as absorption increases. However, there is a significant difference between Figs. 4.3(b) and 4.7(b): the spectral shape of the fluorescence for phantoms with ink as background absorber was not distorted and remained similar to that of the intrinsic signal (measured with only Fluorescein in DI water). This can be explained by refering to either the India ink absorption spectra [Fig. 4.6(a)] or the phantom diffuse reflectance spectra [Fig. 4.7(c)]. Similar to the

Hb phantom cases, increasing absorption (from I1 to I5) decreases the reflectance signal collected [Fig. 4.7(c)]. However, in contrast to the Hb phantoms, there are no peaks in the India ink absorption spectra [Fig. 4.6(a)] or diffuse reflectance spectra [Fig. 4.7(c)]. Note that the drop of diffuse reflectance at 500 nm in Fig. 4.7(c) was due to the strong absorption of Fluoresecein at this region. Again, Eq. (4.7) can be applied to extract Fluorescein concentration. An average error of 5% was obtained for the recovered Fluorescein concentration (Table 4.3) .

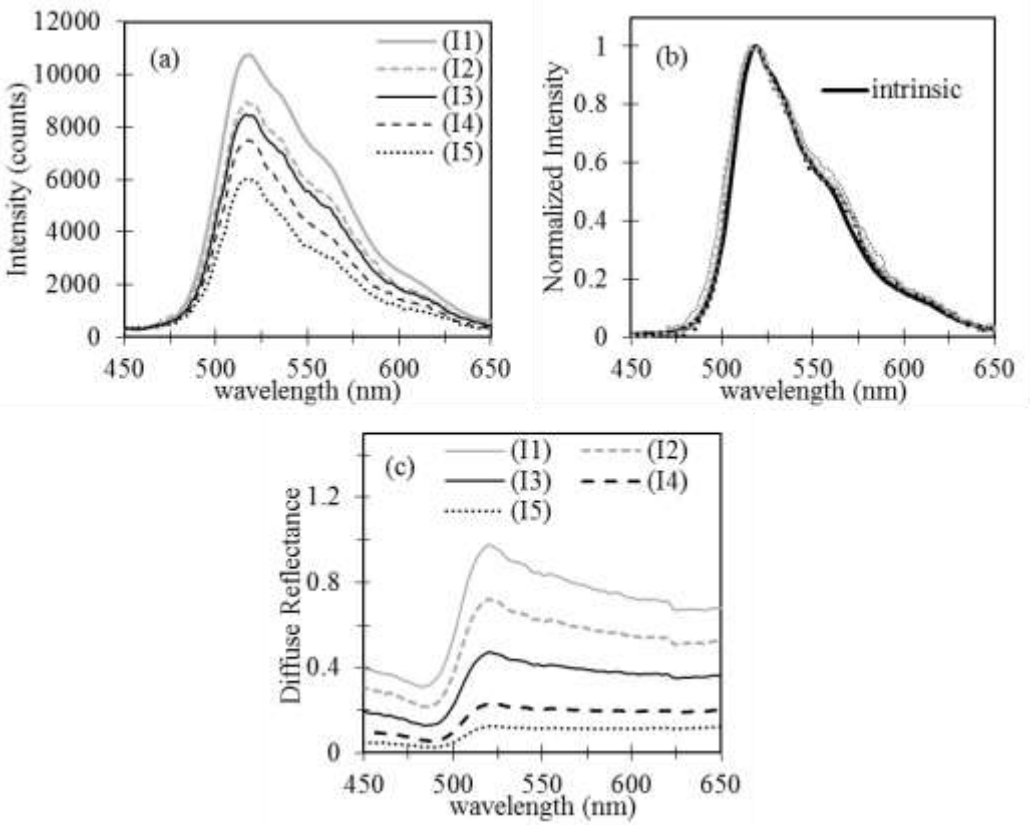

Fig. 4.7 (a) Measured fluorescence emission spectra of the phantoms (I1) to (I5), (b) normalized fluorescence emission spectra and (c) the corresponding diffuse reflectance spectra. These data were collected with the fiber at SDD = 0.59 mm. In all phantoms, Fluorescein concentration was 10^{-4} M.

Table 4.3 The recovered Fluorescein concentration in ink-miscrosphere phantoms. The controlled concentration of Fluorescein in these phantoms was 10^{-4} M.

Quantity	Phantom				
	I1	I2	I3	I4	I5
$f_{355,522}$ (counts)	43,652±741	46,230±420	46,589±744	42,442±837	41,342±823
$F_{355,522}$ (counts)	10,479±149	8778±58	8282±112	7281±115	5918±93
***c* (M)**	**1.04E-04 ±3.E-06**	**1.10E-04 ±2.E-6**	**1.11E-04 ±3.E-6**	**1.01E-04 ±3.E-6**	**9.84E-05 ±3.E-6**

Furthermore, the fluorescence lifetime of India ink phantoms remained the same as that of intrinsic signal as expected (Fig. 4.8). Table 4.4 provides a brief summary of the average fluoresence lifetime of Fluorescein in Hb and India ink phantoms over the emission region of 480-550 nm. Overall, the fluoresence lifetime remained constant, and agreed with previously reported values for Fluorescein in diluted alcohol [1].

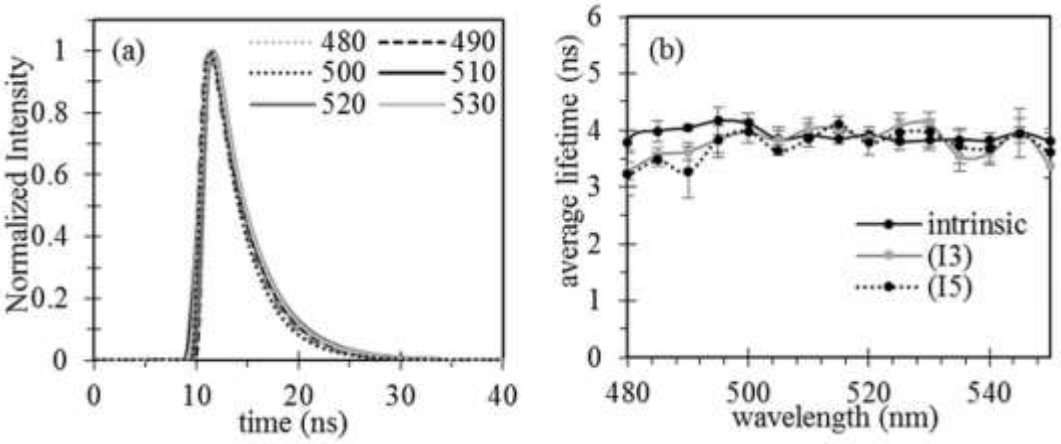

Fig. 4.8 (a) Fluorescence lifetime for phantom (I3) at selected emission wavelengths, and (b) average life time of the phantoms (I3) and (I5) at emission wavelength. The intrinsic signal was collected using Fluorescein 10^{-4} M in diluted ethanol without additional scatterer or absorber.

Table 4.4 Overal average lifetime of Fluorescein in different phantoms (in region 480-550 nm). Concentration of Fluorescein in these phantoms was 10^{-4} M. Concentration of microspheres was 0.4 % w/v and 0.72% w/v in hemoglobin and India ink phantoms, respectively.

Quantity	Phantom						
	intrinsic	Hb3.5	Hb10	Hb20	(I3)	(I4)	(I5)
τ (ns)	4.92±0.12	4.96±0.16	4.97±0.31	4.95±0.32	4.78±0.26	4.84±0.25	4.74±0.26

4.4.3 Effect of microsphere scattering on fluorescence

Fig. 4.9 summarizes the optical properties of phantoms S1 to S6. In these phantoms, microsphere concentration increases from S1 (0.05% *w/v*) to S6 (0.72% *w/v*) [Fig. 4.9(a)] while the concentration of Fluorescein is kept constant at 10^{-5} M. No other absorbers were added. Fig. 4.9(b) shows the μ_a spectrum of Fluorescein 10^{-5} M solution. The goal of this subsection is to inspect the effects of a monotonically decreasing reduced scattering on fluorescence intensity and spectral shape.

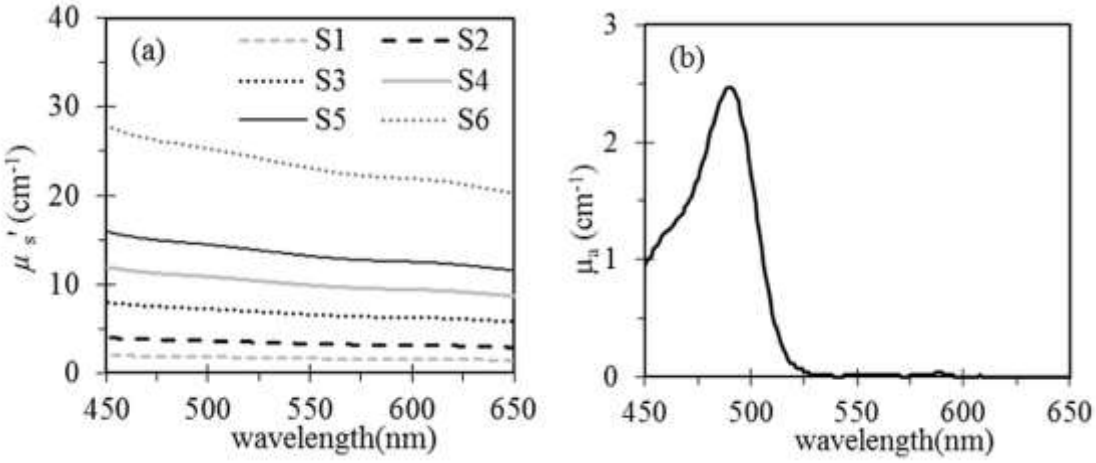

Fig. 4.9 (a) Reduced scattering coefficients μ_s', and (b) absorption coefficients μ_a of phantoms S1 to S6. In these phantoms, the concentration of microspheres increases from phantom S1 to S6 while the concentration of Fluorescein was kept at 10^{-5} M. No other absorbers were added.

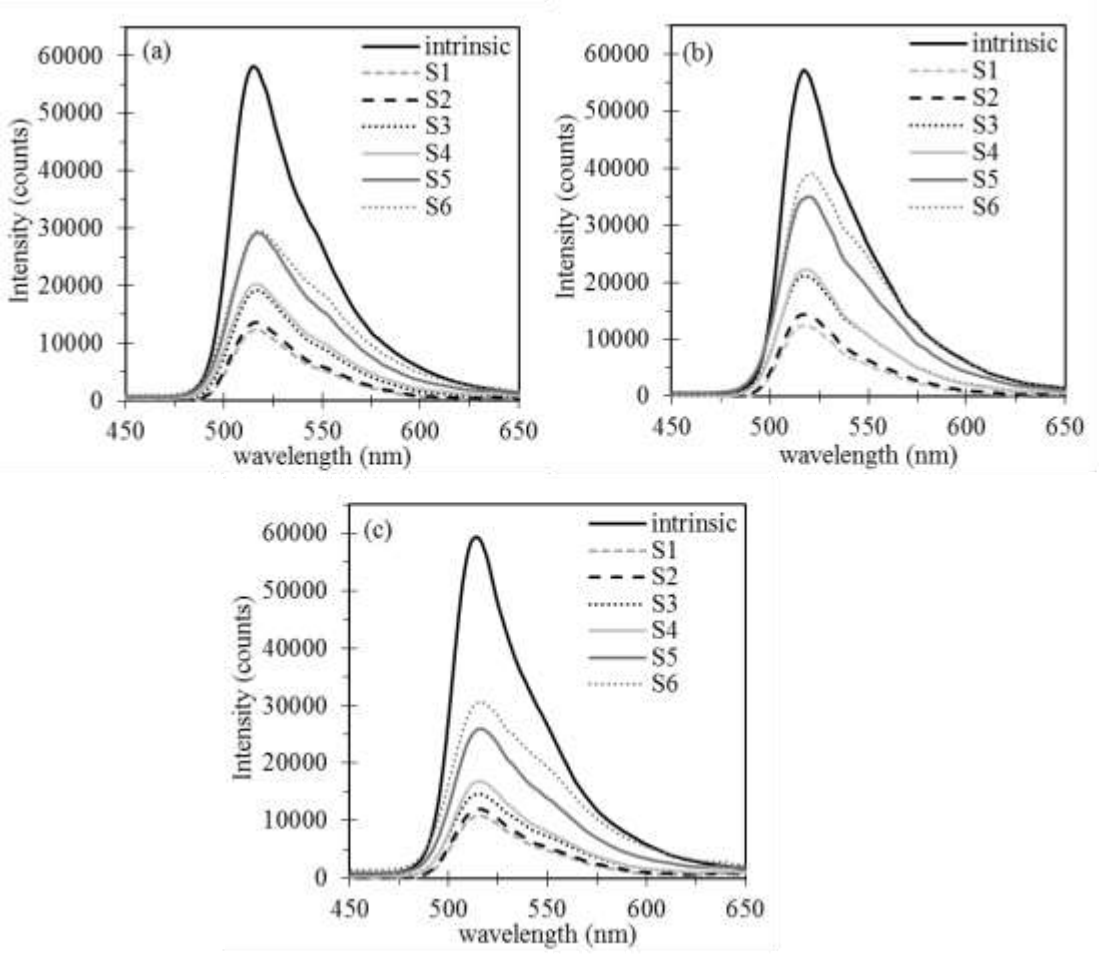

Fig. 4.10 Measured fluorescence emission spectra of the phantoms using (a) SDD = 0.23 mm, (b) SDD = 0.59 mm, and (c) SDD = 1.67 mm. Microsphere concentration increases from sample S1 to sample S6. Fluorescein concentration was kept constant at 10^{-5} M.

The measured steady-state fluorescence of the phantoms is shown in Fig. 4.10 for all collection distances: 0.23 mm [Fig. 4.10(a)], 0.59 mm [Fig. 4.10(b)] and 1.69 mm [Fig. 4.10(c)]. In general, adding microspheres decreased the fluorescence intensity at first due to the effect of scattering (intrinsic versus S1). The fluorescence intensity eventually increased if more microspheres were added from S1 to S6. Fig. 4.11(a) further illustrates

this trend by plotting the normalized intensity at the emission peak as a function of μ_s' (at 520 nm). This phenomenon was consistent with what was reported previously [12]. To compare the intensity trend between SDDs, the fluorescence collected at each SDD was normalized to the intrinsic fluorescence at the same SDD [Fig. 4.11(a)]. The current results indicated that increasing SDD from 0.23 mm to 0.59 mm might increase the fluorescence signal up to 40% in highly scattering media although further increasing of SDD showed the reverse [Fig. 4.11(a)]. The corresponding diffuse reflectance of phantoms for SDD = 0.59 mm is also shown in Fig. 4.11(b) while the normalized measured fluorescence and intrinsic signal are plotted in Fig. 4.11(c).

In general, increasing scattering increases the probability of detection, thus increasing the reflectance intensity to be collected by the detection fiber (Fig. 4.11(b)). This is a reversed trend of increasing absorption in India ink cases (Fig. 4.7(c)). Similar to the India ink cases, the spectral shape of the fluorescence in microsphere phantoms remains unchanged [Fig. 4.11(c)]. India ink absorption coefficient and microsphere reduced scattering coefficient are related to wavelength in the form of $\mu = a\lambda^{-b}$, where a and b are positive fitting coefficients, λ is the wavelengths and μ represents absorption coefficients in the India ink case and reduced scattering coefficients in the microsphere case [34,35]. Therefore, the results shown in Figs. 4.7(b) and 4.11(c) might indicate that exponential decrease of scattering or absorption with increasing wavelengths do not have effects on the fluorescence spectral shape. Eq. (4.7) was applied to retrieve the concentration of Fluorescein in the phantoms S1-S6, considering SDD = 0.59 mm,

exposure time ratio of 1/11700 and I_x value of 63056 counts. As shown in Table 4.5, an average percentage error of 8% was observed in the recovered Fluorescein concentration. In addition, the fluorescence lifetime remained within the standard deviation (Fig. 4.12). Table 4.6 provides an overall summary of the average life-time in region 480-550 nm for phantoms S1 to S6.

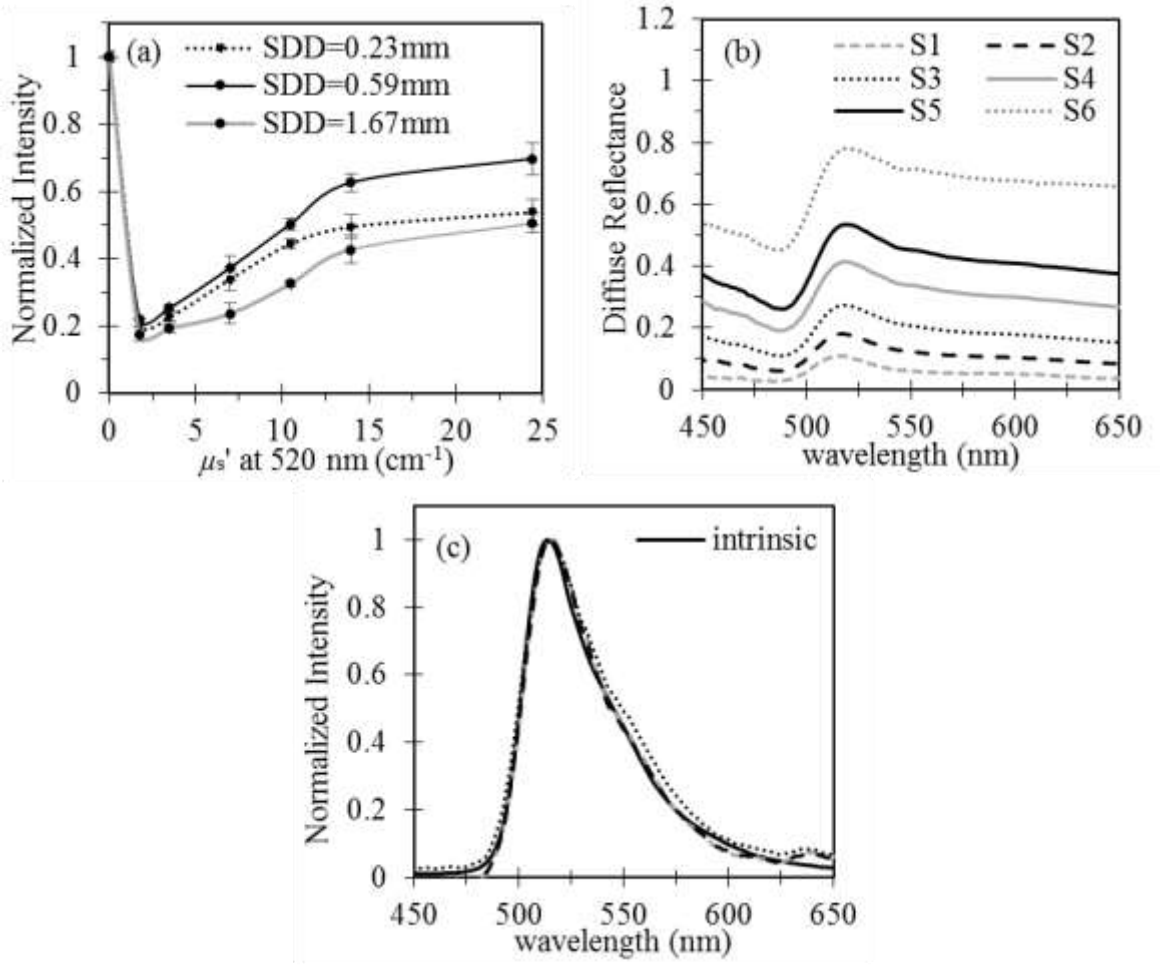

Fig. 4.11 (a) Normalized fluorescence intensity as a function of μ_s' at emission peak of 520 nm for all three SDDs, (b) corresponding total diffuse reflectance spectra at SDD = 0.59 mm, (c) normalized fluorescence intensity. Fluorescein concentration was kept constant at 10^{-5} M.

Table 4.5 The extracted Fluorescein concentration (*c*) in microsphere phantoms from Eq. (4.5). The controlled concentration of Fluorescein in these phantoms was 10^{-5} M.

Quantity	Phantom					
	S1	S2	S3	S4	S5	S6
$f_{355,522}$ (counts)	40,550±1247	51,902±872	43,682±945	54,050±462	49,208±1145	51,367±916
$F_{355,522}$ (counts)	10,036±211	10,998±178	13,493±258	15,688±160	24,617±377	29,294±236
***c* (M)**	**9.05E-06 ±6.E-07**	**1.16E-05 ±4E-07**	**9.75E-06 ±4.E-07**	**1.21E-05 ±2.E-07**	**1.10E-05 ±4.E-07**	**1.15E-05 ±3.E-07**

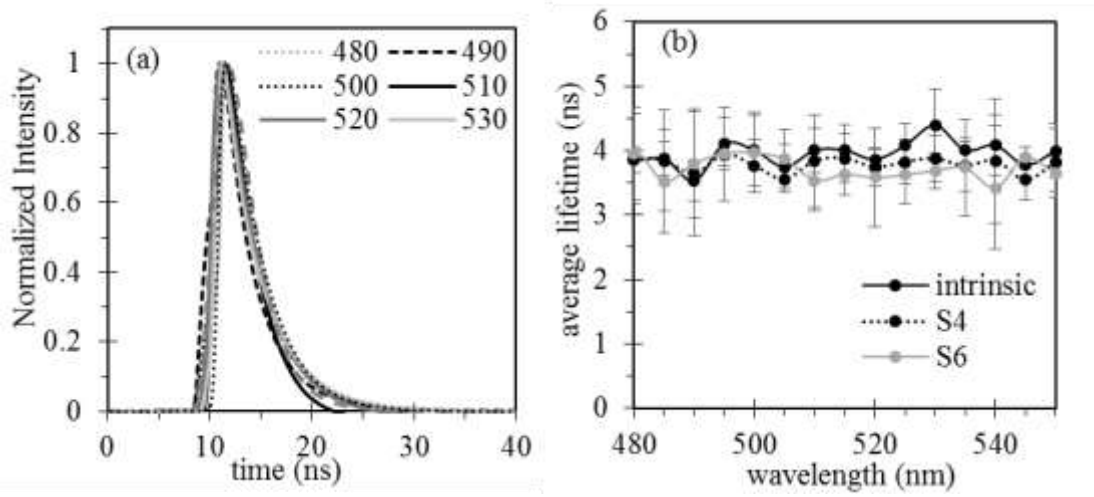

Fig. 4.12 (a) Fluorescence lifetime for phantom S6 at selected emission wavelengths and (b) average lifetime of the phantoms S4 and S6 at emission wavelength. The intrinsic signal was collected using Fluorescein 10^{-5} M in diluted ethanol without additional scatterer or absorber.

Table 4.6 Overal average lifetime in region 480-550 nm of Fluorescein for phantom S1 to S6.

Quantity	Phantom						
	intrinsic	S1	S2	S3	S4	S5	S6
τ (ns)	4.96±0.20	4.85±0.18	4.69±0.20	4.73±0.19	4.81±0.12	4.71±0.21	4.72±0.18

4.5 Discussion and Conclusions

The current study has shown that hemoglobin absorption strongly distorted the fluorescence spectra of Fluorescein at emission wavelength regions near 540 nm and 580 nm. Most endogenous fluorophores in human tissues emit in this wavelength region upon irradiation with ultraviolet light [1]. Using the proposed method and the constructed phantoms with optical property ranges reported for mucosal tissues and brain tissues (μ_a of 1.2-20 cm^{-1} and μ_s' of 1.7-24.5 cm^{-1} at 540 nm) [2,5,18,33-35,51,52], Fluorescein concentration was recovered with an average error of 10% (Fig. 4.5, Table 4.1) considering only the emission peak at 522nm. On average over 450-650 nm, the intrinsic fluorescence intensity of Fluorescein was recovered with an error of 27% (versus 90% with raw signal). While spectral fitting reduced error in recovering fluorescence by 66% on average over 450-650 nm, the percentage error of fitted data was higher than that of non-fitted data at the emission peak 522 nm (3% versus 8%). Although absorption affects fluorescence and diffuse reflectance differently due to the difference in light path shown in Eqs. (4.3) and (4.4), this difference was accounted for in Eq. (4.5).

In addition, the absorption distortion on f_{xm2} line shape was accounted for by the ratio of R_{tm}/R_{0m} in Eq. (4.1) [12]. The proposed method was also efficient in retrieving Fluorescein's concentration in India ink and microsphere phantoms with an average percentage error of 5% and 8%, respectively (Tables 4.3 and 4.5). The current approach used the same concept as previous studies to the extent in which the measured diffuse reflectance was used to compensate the effect of hemoglobin absorption on fluorescence signal [12,31]. What made our approach unique were the ability to recover absolute

fluorescence intensity and to estimate fluorophore concentration via the experimental calibration of individual fibers without the expense of complicated computation. Our ultimate goal is to recover fluorophore concentration using diffuse reflectance and fluorescence measurements and optical properties of the targeted volume. In this manuscript, we demonstrated that the proposed method is feasible to recover fluorophore concentration if optical properties are known. In the next step, an inverse solution is being developed to recover optical properties, and to demonstrate this approach is able to perform real-time tissue measurement. This addition will make the current approach more practical in studying tissue samples.

Although a single fluorophore was used in our study, this should not limit the application of the proposed method in media with multiple fluorophores. As demonstrated in the current study, the recovered intensity at the emission peak is crucial to extract fluorophore concentration. In biological tissues, each fluorophore (NADH, FAD, and collagen) has a known emission peak which can be recovered using Eq. (4.1), allowing extraction of its concentration via Eq. (4.7). Although Muller and Hendriks were unable to recover fluorophore concentration, their studies demonstrated the ability of the proposed method to recover multiple fluorescence peaks via Eq. (4.1) [16].

The current results also show that scattering and absorption materials whose attenuation coefficients decay exponentially with wavelengths (such as black India ink and polystyrene microspheres) have minor effect on the spectral shape of the fluorescence [Figs. 4.7(b) and 4.11(c)]. These observations were made when studying the broadband emission signal of Fluorescein in 500-625 nm. This finding might indicate that absorption and scattering from

NADH, FAD and collagen fibers do not have significant effects on the fluorescence spectral shape because their attenuation coefficients decay exponentially with wavelength, similar to those of India ink or microspheres [2,5,34]. Therefore, hemoglobin is the only absorber of concern. In addition, a consistency in the average fluorescence lifetime measured with the time-resolved system verified that the chemical structure of Fluorescein was not affected by the introduction of India ink, microsphere or hemoglobin.

Furthermore, the current results suggested that increasing SSD from 0.23 mm to 0.59 mm has the potential to increase the fluorescence signal in highly scattering media, especially for S4 to S6 [Fig. 4.11(a)]. Therefore, a small increase in collection distance could increase the probability of detection. However, a larger increase of SDD would decrease the probability for an emitted photon to reach the detection fiber. As a result, fluorescence intensity was high at SDD of 0.59 mm, and low at SDD of 1.67 mm. Additional theoretical analysis is necessary to confirm this result, and to optimize the design to maximize the measured fluorescence signal.

Acknowledgments

The authors would like to thank Professor Leyla Soleymani of the Department of Engineering Physics at McMaster University for access to her laboratory during phantom fabrication. This project was supported in part by the Natural Sciences and Engineering Research Council (NSERC) of Canada and Canadian Cancer Society Research Institute (CCSRI). QF holds the Canada Research Chair in Biophotonics at McMaster University.

References

1. M. Y. Berezin and S. Achilefu, "Fluorescence lifetime measurements and biological imaging," Chem. Rev. **110**(5), 2641-2684 (2010).

2. R. Drezek, C. Brookner, I. Pavlova, I. Boikol, A. Malpica, R. Lotan, M. Follen, and R. Richards-Kortum, "Autofluorescence microscopy of fresh cervical-tissue sections reveals alterations in tissue biochemistry with dysplasia, " Photochem. Photobiol. **73**(5), 636–641 (2001).

3. I. Pavlova, K. Sokolov, R. Drezek, A. Malpica, M. Follen, and R. Richards-Kortum, "Microanatomical and Biochemical Origins of Normal and Precancerous Cervical Autofluorescence Using Laser‐scanning Fluorescence Confocal Microscopy," Photochemistry and photobiology **77**(5) 550-555 (2003).

4. P. P. Provenzano, D. R. Inman, K. W. Eliceiri, J. G. Knittel, L. Yan, C. T. Rueden, J. G. White, and P. J. Keely, "Collagen density promotes mammary tumor initiation and progression," BMC Medicine **6**(11), 11 (2008).

5. S. K. Chang, D. Arifler, R. Drezek, M. Follen, and R. Richards-Kortum, "Analytical model to describe fluorescence spectra of normal and preneoplastic epithelial tissue: comparison with Monte Carlo simulations and clinical measurements," J. Biomed. Opt. **9**(3), 511–522 (2004).

6. D. C. Walker, B. H. Brown, A. D. Blackett, J. Tidy, and R. H. Smallwood, "A study of the morphological parameters of cervical squamous epithelium, " Physiol. Meas. **24**(1), 121–135 (2003)

7. M. H. Johnston, "Technology insight: ablative techniques for Barrett's esophagus: current and emerging trends, " Nature Clin. Prac. Gastro. Hepat. **2**(7), 323–330 (2005).

8. P. V. Butte, Q. Fang, J. A. Jo, W. H. Yong, B. K. Pikul, K. L. Black, L. Marcu, "Intraoperative delineation of primary brain tumors using time-resolved fluorescence spectroscopy, " J. Biomed. Opt., **15**(2), 027008-027008 (2010)

9. L. Marcu, J. A. Jo, Q. Fang, T. Papaioannou, T. Reid, J-H. Qiao, J. D. Baker, J. A. Freischlag, M. C. Fishbein, "Detection of Rupture-Prone Atherosclerotic Plaques by Time-Resolved Laser Induced Fluorescence Spectroscopy", Atherosclerosis, **204**(1), 156-164(2009)

10. J. R. Lakowicz, Joseph R., B. Shen, Z. Gryczynski, S. D'Auria, I. Gryczynski, "Intrinsic fluorescence from DNA can be enhanced by metallic particles," Biochem. Biophys. Res. Com. **286**(5), 875-879 (2001).

11. J. Wu, M. S. Feld, and R. P. Rava, "Analytical model for extracting intrinsic fluorescence in turbid media." Appl. Opt., **32**(19) 3585-3595 (1993).

12. M. G. Müller, I. Georgakoudi, Q. Zhang, J. Wu, and M. S. Feld, "Intrinsic fluorescence spectroscopy in turbid media: disentangling effects of scattering and absorption," Appl. Opt., **40**(25), 4633-4646 (2001).

13. G. M. Palmer and N. Ramanujam, "Monte-Carlo-based model for the extraction of intrinsic fluorescence from turbid media," J. Biomed. Opt. **13**(2), 024017 (2008).

14. S. C. Kanick, D.J. Robinson, H.J.C.M. Sterenborg, and A. Amelink, "Extraction of intrinsic fluorescence from single fiber fluorescence measurements on a turbid medium," Opt. Let., **37**(5), 948-950 (2012).

15. G. M. Palmer, and N. Ramanujam, "Monte Carlo-based inverse model for calculating tissue optical properties. Part I: Theory and validation on synthetic phantoms," Appl. Opt., **45**(5), 1062-1071 (2006).

16. M. Müller, and B. H. Hendriks, "Recovering intrinsic fluorescence by Monte Carlo modeling." J. Biomed. Opt., **18**(2) 027009-027009 (2013).

17. Q. Wang, A. Agrawal, N. S. Wang, and T. Joshua Pfefer, "Condensed Monte Carlo modeling of reflectance from biological tissue with a single illumination–detection fiber," *Selected Topics in Quantum Electronics, IEEE* **16**(3) 627-634 (2010).

18. V. N. Du Le, Q. Wang, T. Gould, J. C. Ramella-Roman, T. J. Pfefer, "Vascular Contrast in Narrow Band and White Light Imaging." Appl. Opt., **53**(18), 4061-4071 (2014).

19. Q. Fang, and D. A. Boas, "Monte Carlo simulation of photon migration in 3D turbid media accelerated by graphics processing units," Optics Express **17**(22), 20178-20190 (2009).

20. J. Chen , Q. Fang, and X. Intes, "Mesh-based Monte Carlo method in time-domain widefield fluorescence molecular tomography," J. Biomed. Opt., **17**(10) 1060091-1060098 (2012).

21. Q. Fang, "Mesh-based Monte Carlo method using fast ray-tracing in Plücker coordinates," Biomed. Opt. Exp., **1**(1), 165-175 (2010).

22. K. R. Diamond, T. J. Farrell, M. S. Patterson, "Measurement of fluorophore concentrations and fluorescence quantum yield in tissue-simulating phantoms using three diffusion models of steady-state spatially resolved fluorescence," Phys. Med. Biol., **48**(24), 4135-49 (2003).

23. D. J. Cuccia, F. Bevilacqua, A. J. Durkin, F. R. Ayers , B. J. Tromberg, "Quantitation and mapping of tissue optical properties using modulated imaging, " J. Biomed. Opt., **14**, 024012-024012.

24. J. C. Finlay, and T. H. Foster, "Recovery of hemoglobin oxygen saturation and intrinsic fluorescence with a forward-adjoint model," App. Opt., **44**(10), 1917-1933 (2005).

25. A. Kim, M. Khurana, Y. Moriyama, and B.C. Wilson, "Quantification of in vivo fluorescence decoupled from the effects of tissue optical properties using fiber-optic spectroscopy measurements," J. Biomed. Opt., **15**(6), 067006-067006 (2010).

26. C. L. Hoy, U.A. Gamm, H.J.C.M. Sterenborg, D.J. Robinson, and A. Amelink, "Method for rapid multidiameter single-fiber reflectance and fluorescence spectroscopy through a fiber bundle, " J. Biomed. Opt., **18**(10), 107005-107005 (2013).

27. V. N. Du Le, Z. Nie, J. E. Hayward, T. J. Farrell, and Q. Fang, "Measurements of extrinsic fluorescence in Intralipid and polystyrene microspheres, " Biomed. Opt. Express, **5**(8), 2726-2735 (2014)

28. T. A. Middelburg, C.L. Hoy, H.A.M. Neumann, A. Amelink, and D.J. Robinson, "Correction for tissue optical properties enables quantitative skin fluorescence measurements using multi-diameter single fiber reflectance spectroscopy, " J. Dermatol. Sci., **79**(1), 64-73(2015).

29. R. B. Saager, D.J. Cuccia, S. Saggese, K.M. Kelly, and A.J. Durkin, "Quantitative fluorescence imaging of protoporphyrin IX through determination of tissue optical properties in the spatial frequency domain," J. Biomed. Opt., **16**(12), 126013-1260135(2011).

30. U. Sunar, D. J. Rohrbach, J. Morgan, N. Zeitouni, and B.W. Henderson, "Quantification of PpIX concentration in basal cell carcinoma and squamous cell carcinoma models using spatial frequency domain imaging, " Biomed. Opt. Exp., **4**(4), 531-537(2013).

31. Q. Zhang, M. G. Müller, J. Wu, and M. S. Feld, "Turbidity-free fluorescence spectroscopy of biological tissue, "Opt. Let., **25**(19),1451-1452 (2000)

32. B. W. Pogue and M. S. Patterson, "Review of tissue simulating phantoms for optical spectroscopy, imaging and dosimetry," J. Biomed. Opt. **11**(4), 041102 (2006).

33. N. Rajaram, T. J. Aramil, K. Lee, J. S. Reichenberg, T. H. Nguyen, and J. W. Tunnell, "Design and validation of a clinical instrument for spectral diagnosis of cutaneous malignancy, " Appl. Opt., **49**(2), 142–152 (2010).

34. Q. Wang, V. N. Du Le, J. Ramella-Roman, J. Pfefer, "Broadband ultraviolet-visible optical property measurement in layered turbid media." Biomed. Opt. Exp., **3**(5), 1226-1240 (2012).

35. N. Rajaram, T. H. Nguyen, J. W. Tunnell, "Lookup Table–based inverse model for determining optical properties of turbid media," J. Biomed. Opt., **13**(5), 050501-050501 (2008).

36. T. R. Wagner, W. G. Houf, F. P. Incropera, "Radiative property measurements for India ink suspensions of varying concentration," Solar Energy **25**, 549-554 (1980).

37. H. Xu and M. Patterson, "Determination of the optical properties of tissue-simulating phantoms from interstitial frequency domain measurements of relative fluence and phase difference," Opt. Exp., **14**(14), 6485-6501 (2006).

38. Q. Liu, C. Zhu, and N. Ramanujam, "Experimental validation of Monte Carlo modeling of fluorescence in tissues in the UV-visible spectrum," J. Biomed. Opt., **8**(2), 223–236 (2003).

39. S. A. Ermilov, T. Khamapirad, A. Conjusteau, M. H. Leonard, R. Lacewell, K. Mehta, T. Miller, A. A. Oraevsky, "Laser optoacoustic imaging system for detection of breast cancer, " J. Biomed. Opt., **14**(2), 024007-024007 (2009).

40. I. Barman, N. C. Dingari, N. Rajaram, J. W. Tunnell, R. R. Dasari, M. S. Feld, "Rapid and accurate determination of tissue optical properties using least-squares support vector machines," Biomed. Opt. Exp., **2**(3), 592-599 (2011).

41. B. Yu, A. Shah, V. K. Nagarajan, D. G. Ferris. "Diffuse reflectance spectroscopy of epithelial tissue with a smart fiber-optic probe." Biomed. Opt. Exp., **5**(3), 675-689 (2014).

42. D. Cappon, T. J. Farrell, Q. Fang, J. E. Hayward. "Fiber-optic probe design and optical property recovery algorithm for optical biopsy of brain tissue." J. Biomed. Opt., **18**(10), 107004-107004 (2013).

43. Z. Nie, R. An, J. E. Hayward, T. J. Farrell, Q. Fang, "Hyperspectral fluorescence lifetime imaging for optical biopsy." J. Biomed. Opt., **18**(9), 096001-096001 (2013).

44. Y. Yuan, J-Y. Hwang, M. Krishnamoorthy, J. Ning, Y. Zhang, K. Ye, R. C. Wang, M. J. Deen, Q. Fang, "High throughput AOTF-based time-resolved fluorescence spectrometer for optical biopsy," Opt. Let., **34**(7), 1132-1134 (2009).

45. P. G. Seybold, M. Gouterman, J. Callis, "Calorimetric, photometric and lifetime determinations of fluorescence yields of fluorescein dyes," Photochem. Photobiol., **9**(3), 229-242 (1969).

46. D. Magde, R. Wong, P. G. Seybold, "Fluorescence quantum yields and their relation to lifetimes of rhodamine 6G and fluorescein in nine solvents: improved absolute standards for quantum yields," Photochem. Photobiol., **75**(4), 327-334 (2002).

47. S. L. Jacques, R. Samatham, N. Choudhury, "Rapid spectral analysis for spectral imaging," Biomed. Opt. Exp., **1**(1) 157-164 (2010).

48. M. S. Twardowski, E. Boss, J. M. Sullivan, P. L. Donaghay, "Modeling the spectral shape of absorption by chromophoric dissolved organic matter," Marine Chemistry **89**(1), 69-88 (2004).

49. X. Zhong, X. Wen, D. Zhu, "Lookup-Table-based inverse model for human skin reflectance spectroscopy: two-layered Monte Carlo simulations and experiments," Opt. Express **22**(2), 1852-1864 (2014).

50. J. M. Dixon, M. Taniguchi, and J. S. Lindsey, "PhotochemCAD. A Computer-Aided Design and Research Tool in Photochemistry and Photobiology," *Photochem. Photobiol.* **81**(1), 212–213 (2005)

51. R. Nachabé, B. H. W Hendriks, M. van der Voort, A. E. Desjardins, H. Sterenborg, "Estimation of biological chromophores using diffuse optical spectroscopy: benefit of extending the UV-VIS wavelength range to include 1000 to 1600 nm," Biomed. Opt. Express **1**(5), 1432-1442 (2010).

52. S. L. Jacques, "Optical properties of biological tissues: a review." Phys. Med. Biol. **58**(11):R37 (2013).

Vinh Nguyen Du Le is a PhD student in the Medical Physics program at McMaster University (Hamilton, ON). He received a B.Sc. degree (2009) and a M.Sc. degree (2010) in Biomedical Engineering from the Catholic University of America (Washington, DC). He was a research engineer at the U. S. Food and Drug Administration from 2010 to 2012.

Michael S. Patterson is the director of medical physics at Juravinski Cancer Centre (Hamilton, ON). He received a B.Sc. degree (1973) from Queen's University, a M.Sc. degree (1976) from McMaster University, and a Ph.D. degree (1984) from the University of Toronto.

Thomas J. Farrell is a Medical Physicist at the Juravinski Cancer Centre and the chair of the Medical Physics department at McMaster University. He received a Ph.D. degree (1990) from McMaster University.

Joseph E. Hayward is a Medical Physicist at the Juravinski Cancer Centre and an Associate Professor of the Medical Physics department at McMaster University. He received a Ph.D. degree (1993) in lasers and electro-optics in Engineering Physics from McMaster University.

Qiyin Fang is an Associate Professor of Engineering Physics and the chair of Biophotonics at McMaster University. He received a B.Sc. degree (1995) in physics from Nankai University, a MSc. Degree (1998) in Applied Physics and a Ph.D. degree (2002) in Biomedical Physics from East Carolina University.

Chapter 5: Paper III - Dual Modality Optical Biopsy of Glioblastomas Multiforme with Diffuse Reflectance and Fluorescence: *Ex Vivo* Retrieval of Optical Properties

Vinh Nguyen Du Le,[1*] John Provias,[2] Naresh Murty,[3] Michael S. Patterson,[4] Zhaojun Nie,[5] Joseph E. Hayward,[4,6] Thomas J. Farrell,[4,6] William McMillan,[4,7] Wenbin Zhang,[8] and Qiyin Fang [5,9]

[1]Radiation Sciences Graduate Program, McMaster University, Hamilton, Ontario, Canada

[2]Department of Anatomical Pathology, McMaster University, Hamilton, Ontario, Canada

[3]Department of Surgery, McMaster University, Hamilton, Ontario, Canada

[4]Juravinski Cancer Centre, Hamilton, Ontario, Canada

[5]School of Biomedical Engineering, McMaster University, Hamilton, Ontario, Canada

[6]School of Interdisciplinary Science, McMaster University, Hamilton, Ontario, Canada

[7]Department of Oncology, McMaster University, Hamilton, Ontario, Canada

[8]Shanghai 9th People's Hospital, Shanghai Jiaotong University Medical School, Shanghai, China

[9]Department of Engineering Physics, McMaster University, Hamilton, Ontario, Canada

Submitted to Journal of Biomedical Optics.

Introduction to paper III

This paper is to evaluate the abilities of the dual optical modality, diffuse reflectance spectroscopy and fluorescence spectroscopy, in differentiating glioblastomas multiforme (GBM) from low grade glioma (LGG) during *ex vivo* measurements of brain tumor specimen. To estimate the sensitivity and specificity of the method, different parameters including diffuse reflectance, optical properties, oxygen saturation, fluorescence properties (emission signal and fluorescence life-time) were used. An experimental model was developed to extract tissue optical properties which were used to access tumor grade. Prior to tissue measurement, the model was evaluated on tissue-simulating phantoms with controlled optical properties. The key novelty of this work is the ability to measure multiple optical parameters of GBM and LGG separately from the primary brain tumor group, and to optimize these parameters for tumor differentiation without relying on heavily computational models of light propagation.

In this paper, I developed the inverse solution model and the optical phantom models, and carried out all the experimental measurements and data analysis. Brain specimen were cut and delivered by Dr. Murty, the neurosurgeon. Histological analysis and tumor grading were done by Dr. Provias, the pathologist. The manuscript was written by me, and edited by Drs. Patterson, Farrell, Hayward, and Fang.

Zhaojun Nie, Wenbin Zhang, William McMillan, Drs. Provias and Murty did not contribute in the writing of the manuscript.

The manuscript has been slightly altered to confront the style of the thesis as whole, such as font, spacing, numbering of pages, equations, and figures and tables.

Contents of paper III

5.1 Abstract

Glioma itself accounts for 80% of all malignant primary brain tumors and glioblastoma multiforme (GBM) accounts for 55% of such tumor. Diffuse reflectance and fluorescence spectroscopy have the potential to discriminate healthy tissues from abnormal tissues and therefore are promising non-invasive methods to improve the accuracy of brain tissue resection. In this study, optical properties were retrieved using an experimentally evaluated inverse solution. On average, the scattering coefficient is 2.4 times higher in GBM than in LGG and absorption coefficient is 48% higher. The results reported here show that the combination of diffuse reflectance and fluorescence spectroscopy could achieve sensitivity of 100% and specificity of 90% in discriminating GBM from low grade glioma (LGG) during *ex vivo* measurements of 22 sites from seven glioma specimens. Therefore, the current technique might be a promising tool to aid neurosurgeons to determine the extent of surgical resection of glioma, improving intra-operative tumor identification for guiding surgical intervention.

5.1 Introduction

Glioma is a term used to describe all tumors arising from glial cells in the brain. There are three subgroups - astrocytoma, oligodendroglioma, and ependymoma - represent 30% of all primary brain tumors and 80% of all malignant primary brain tumors [1]. Glioblastoma multiforme (GBM), the highest tumor grade in astrocytoma, accounts for nearly 55% of such tumors, and affects over 12,000 people in the United States per year [1-4]. GBM prognosis is very poor and its median survival is reported to be from less than 14 months [5] to 2 years [6,7]. Currently, neurosurgeons define the extent of a brain tumor resection using techniques such as brain biopsy [8,9], intraoperative ultrasound [10], or visual inspection with the assistance of pre-operative magnetic resonance (MR) images [11]. Unfortunately, each method has considerable limitations. Brain biopsy is invasive hence limits the number of specimens taken, leading to large sampling errors. Brain tumors frequently resemble normal brain tissues in ultrasound images, causing incomplete removal of margins [12]. In addition, non-rigidity of brain tissues might cause positional shifts during the operation making the defined margins on pre-operative MR images unreliable [13,14]. This problem may lead to either unplanned resection of normal brain or incomplete resection of tumor [15,16]. Therefore, a non-invasive method is desired to allow real-time identification of GBM tissue.

Early studies have shown that diffuse reflectance spectroscopy (DRS) has the potential for non-invasive detection of mucosal abnormalities via differences in tissue optical properties [17-19], and that fluorescence spectroscopy has the ability to detect malignant tissues by analyzing fluorescence characteristics such as emission spectrum [20,21] and

decay lifetime [22,23]. Optical properties including absorption coefficient (μ_a) and reduced scattering coefficient (μ_s') are wavelength dependent quantities that govern light propagation in tissues [24-27]. In human mucosa, the principal absorbers are hemoglobin in blood, collagen crosslinks, nicotinamide adenine dinucleotide (NADH), and flavin adenine dinucleotide (FAD) [28-30]. Meanwhile, density and the morphology of cells are the main source of the scattering signal [31]. Tissue optical properties are tied to the concentration of absorbers and scatterers present in that tissue. For example, a high number density of cells leads to high μ_s' [32] while high blood vessel density suggests high μ_a [33,34]. In Lin *et al*.'s studies, it was shown that DRS alone could be used to discriminate brain tumor from normal brain tissues during *in vivo* measurements of 12 patients with a sensitivity of 95% and a specificity of 66% [35].

Although the emission peaks in the steady-state fluorescence spectrum could be used to identify the principal fluorophores, the fluorescence signal is usually distorted by absorption and scattering of absorbers and scatterers present in the tissue [36,37]. To correct the measured fluorescence, and to enable tissue discrimination using steady-state fluorescence, diffuse reflectance must be used in parallel [36,37]. By combining steady-state fluorescence and diffuse reflectance, Lin *et al*. were also able to identify infiltrating tumor margins from normal brain tissues with a sensitivity of 100% and a specificity of 76% [38]. In similar studies with the integrated system, Toms *et al*. could identify glioma margins of 24 glioma patients with sensitivity of 94% and specificity of 93% [39], and Valdés *et al*. was able to achieve sensitivity and specificity of 94% in differentiating 2 LGG patients and 5 GBM patients [40]. Without using DRS, Butte *et al*. showed that

fluorescence spectroscopy alone had the potential to discriminate low grade gliomas (LGG) with a sensitivity of 100% and a specificity of 98% [22,23]. Unfortunately, the technique suffered low sensitivity (47%) for detection of high grade gliomas (HGG) [22,23]. In these studies, however, the spectral analysis for specific tumor grades, especially for LGG and GBM was not analyzed separately [35,38-40], and the optical properties were not recovered [22,23,35,38,39]. In general, intraoperative differentiation of GBM and LGG can help neurosurgeons determine the extent of neurosurgical resection, which is a significant factor influencing post-surgical recurrence and prognosis [40-42]. Knowledge of optical properties can also be used to calculate oxygen saturation which is expressed as the percentage of oxy-hemoglobin in the total hemoglobin [43-45]. Although Asgari *et al.* were able to show that oxygen saturation was lower for LGG groups (36 ± 21%) and higher for GBM (52 ± 18%) due to the existence of arteriovenous shunts and metabolic shunts in GBM, optical properties were not measured [46]. Whereas attempts to extract optical properties of healthy brain tissues and gliomas were performed *in vitro* by Gebhart *et al.* [47], and *in vivo* by Valdés *et al.* [40], optical properties were averaged for all gliomas, and separated observations for LGG and GBM were not available [40,47].

In this paper, *ex vivo* diffuse reflectance and fluorescence measurements were performed to differentiate GBM from LGG in a total of 22 sites of seven glioma patients. An experimental look-up table (LUT) combined with a fitting routine was used to extract optical properties from 350-700 nm. The approach was validated on liquid tissue-simulating phantoms containing hemoglobin, polystyrene microspheres and India ink.

5.2 Materials and methods

5.2.1. Optical phantoms and the inverse solution

Similar to a previous study [48], the inverse solution to extract optical properties from the measured diffuse reflectance combines an experimental look-up table (LUT) and fitting algorithms. The LUT was generated by measuring the diffuse reflectance from tissue-simulating phantoms with known optical properties. To simulate tissue scattering, polystyrene microspheres with diameter of 1 μm (07310-15, Polysciences Inc., PA) were used. To simulate tissue absorption, black India ink (Higgins Ink, Chartpak Inc., MA) was used. A 6 x 4 matrix of 24 phantoms consisting of 6 different concentrations of black India ink (0.025%, 0.05%, 0.1%, 0.2%, 0.35% and 0.5% of the concentrated ink solution) and 4 different concentration of microspheres (0.2%, 0.45%, 0.7% and 1% *w*/*v*) was created (Fig. 5.1). Within the selected concentrations of India ink and microspheres, a μ_a range of 0.05-47 cm^{-1} and μ_s' range of 5-42 cm^{-1} were covered for wavelength range 430-700 nm (Fig. 5.1b and c). These optical properties were selected based on various reports studying human brain tissues and mucosal tissues [20,29,30,47,49]. To evaluate the LUT, selected phantoms containing ferrous stabilized hemoglobin (H0267, Sigma-Aldrich, MO) and microspheres with different concentrations were created. The diffuse reflectance from these phantoms was measured and the recovered optical properties were compared to target values.

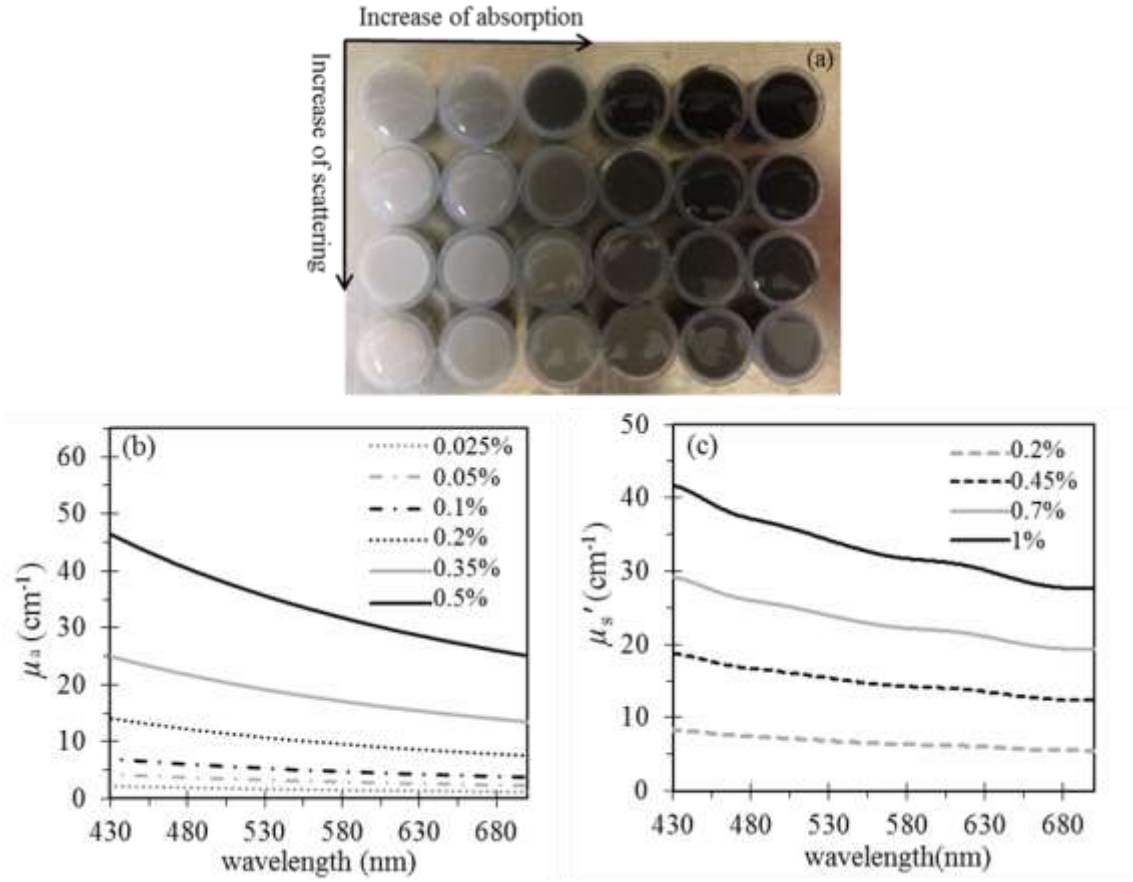

Fig. 5.1 Matrix of optical phantoms for LUT development: (a) Top surface images of 24 phantoms captured with a standard digital camera, (b) absorption coeffients μ_a and (c) reduced scattering coefficients μ_s'. In (a), 6 concentrations of black India ink are 0.025%, 0.05%, 0.1%, 0.2%, 0.35% and 0.5% , and 4 concentrations of microspheres are 0.2%, 0.45%, 0.7% and 1% *w*/*v*. These concentrations correspond to 6 spectra of μ_a in (b) and 4 spectra of μ_s' in (c).

In all phantoms, target optical properties were controlled, and calculated by applying Beer-Lambert's law to the actual absorbance of pure solute absorbers (India ink or hemoglobin) measured with a spectrophotometer (Ultraspec 3000, Pharmacia Biotech Inc., NJ) for μ_a, and by applying Mie theory to microsphere concentration for μ_s' [50]. Hemoglobin H0267 has an absorption spectrum similar to that of human blood with

secondary absorption peaks at 540 nm and 580 nm and stable f_2 [49,51,52]. Polystyrene microspheres with diameter of 1 μm were preferred as scatterers because their scattering anisotropy is in a similar range to that of many biological tissues (g = 0.89-0.93 in UV-Vis), and because their well-controlled size and index of refraction permits accurate calculation of scattering properties using Mie theory [45,50,53]. Black India ink is widely used to simulate secondary absorbers in tissue due to its exponential decrease of absorption with wavelength, its low cost, spectral stability, and low-fluorescence [54-57].

To fit the optical properties, the least squares fitting routine fminsearch() in MATLAB® was used so that the absorption coefficients and the reduced scattering coefficients were constrained in the form of Eq.(5.1) and (5.2). This optimization method is based on the Nelder-Mead simplex algorithm and has been used widely for spectral analysis in spectral imaging [58-60]. The total absorption coefficient, μ_a, accounts for absorption of a primary absorber (human blood) and of secondary absorbers (i.e. NADH, FAD, collagen) [20,28 ,49]. In general, the absorption coefficients of secondary absorbers exponentially decay with wavelength [20,28] while the absorption coefficients of blood are determined by predominantly by those of Hb and HbO_2 [44,61]. A similar fitting method for total absorption coefficients can be found elsewhere [48,61].

$$\mu_a(\lambda) = A \cdot e^{B \cdot \lambda} + \ln(10) \cdot f_1 \cdot [f_2 \cdot \varepsilon_{HbO2}(\lambda) + (1 - f_2) \cdot \varepsilon_{Hb}(\lambda)] \qquad (5.1)$$

In Eq. (5.1), A and B are fitting coefficients determining the contribution of secondary absorber so that A (cm^{-1}) is the amplitude constant while B (nm^{-1}) is the rate constant; λ is wavelength; f_1 ($mol.litre^{-1}$) is the total concentration of hemoglobin, f_2 (dimensionless) is

oxygen saturation, and ε_{HbO2} ($cm^{-1}.M^{-1}$) and ε_{Hb} ($cm^{-1}.M^{-1}$) are molar extinction coefficients of oxygenated and deoxygenated hemoglobin, respectively. In tissue measurements, *A*, *B*, f_1, f_2 were calculated by applying the least squares fitting to the LUT-recovered μ_a, and the known spectra of ε_{HbO2} and ε_{Hb} [62]. In hemoglobin phantoms without collagen and NADH, *A* was set to zero and the extracted f_2 should be nearly 100% due to the nature of ferrous stabilized hemoglobin [52]. In human tissues, μ_s' is monotonically decreasing with wavelength and the fitting equation for μ_s' can be expressed in form of Eq. (5.2) where *a* with unit of cm^{-1} is the factor characterizing magnitude of scattering, *b* (dimensionless) is the factor that characterizes wavelength dependence of scattering, λ is the wavelength in nanometers [30, 44,61].

$$\mu_s'(\lambda) = a \cdot \lambda^{b} \qquad (5.2)$$

5.2.2. Brain tissue samples

Fresh brain specimens were obtained from brain tissue removed during tumor resection surgery. The study protocol is approved by the McMaster/Hamilton Health Science Integrated Research Ethics Board and patients consented to participate. Prior to the DRS measurement, each specimen was washed with saline, and the spectroscopic measurements were performed within 30 minutes of the surgery. A total of 22 sites were measured from specimens of seven patients. At each site, reflectance and fluorescence measurements were repeated four times to allow averaging, and standard deviation calculation. Following the measurements, each site was marked with tissue marking dyes (Davidson Marking system, Bradley Products Inc., Minneapolis, MN) in different colors. After the optical

measurements, the specimens were preserved in Formaldehyde and then cut into 5 μm thick slices with hematoxylin and eosin (H&E) stain. Tumor grade was assigned by a single pathologist (JP), using World Health Organization guidelines [63]. The biopsy results identified four GBM patients (12 sites), and three LGG patients (10 sites). Surface area of tissue samples is at least 5 times larger than the surface area of the optical probe which has a diameter of 3 mm. Thickness of tissue samples is at least 0.5 cm, and is much larger than the optical penetration depth range of 100-300 μm for human brain tumor at visible wavelengths

5.2.3. Instruments

Diffuse reflectance signals between 430-700 nm were generated using a broadband light source (Dolan-Jenner MI-150, Edmund Optics, NJ), while fluorescence signals were generated using a solid-state laser (PNV-001525-140, Teem Photonics, Meylan, France) at 355 nm with 300 ps pulses. Note that optical properties in the 350-430 nm range were extrapolated using the calculated parameters (A, B, f_1, f_2, a, and b) from the fitting results. Measurements of both diffuse reflectance (DR) and steady state fluorescence (SSF) signals were performed with the same customized optical probe consisting of one source fiber and three detection fibers at source-detector collection distances (SDD) of 0.23, 0.59, and 1.67 mm. A schematic and detailed description of the system can be found elsewhere [64-66]. All fibers used in DRS and SSF measurements have a core diameter of 200 μm and numerical aperture of 0.22. After DRS and SSF measurements were performed, the fluorescence decay was recorded using a 400 μm core optical fiber in the bundle [67]. When

observing highly absorbing phantoms, only background noise was collected with the furthest fibers, thus reducing the prediction accuracy of the inverse solution. Therefore, in the current study, only the two detection fibers closest to the source fiber were used to develop the LUT, and to extract optical properties from the measured reflectance. To calculate the diffuse reflectance *R* from the sample, the measured reflectance intensity of the sample was normalized to the reflectance intensity of a reflection standard with 99.9% reflectivity (Labsphere, Inc., NH) after subtracting background [64].

5.3 Results

5.3.1 Validation of the inverse solution

Fig. 5.2(a) shows examples of diffuse reflectance spectra collected from six phantoms with the same microsphere concentration (0.72% *w*/*v*), and different India ink concentrations (from 0.05% to 1%). Fig. 5.2(b) shows the sparse matrix of diffuse reflectance collected from all 24 phantoms at SDD of 0.23 mm and 0.59 mm. The LUT was evaluated with randomly selected phantoms consisting of hemoglobin and microspheres. Fig. 5.3(a) and 5.3(b) compare the extracted and the target optical properties spectra for a selected phantom with microsphere concentration of 0.7% *w/v* and hemoglobin concentration of 3.5 mg/ml. The target optical properties are those calculated with Beer-Lambert's law and Mie theory while the extracted values are those calculated from the inverse solution. As shown in Fig. 5.3(a) and 5.3(b), the method was able to retrieve μ_a and μ_s' with average errors of 6% and 3%, respectively, from 350-700 nm. Additional phantoms consisting of hemoglobin, India ink and microspheres with a total of 1,750 pairs of target

optical properties were also used for further evaluation of the inverse solution (Fig. 5.4). On average, errors of 12% and 6% was observed for μ_a and μ_s', respectively. Furthermore, the fitting approach was able to retrieve f_1 and StO_2 in all hemoglobin phantoms with average errors of 5.8% and 7%, respectively. For example, the recovered f_1 and StO_2 values for the phantom shown in Fig. 5.3 were 3.3 ± 0.3 mg/ml and 96% ± 3 %, respectively, versus target values of 3.5 mg/ml and 100%, respectively.

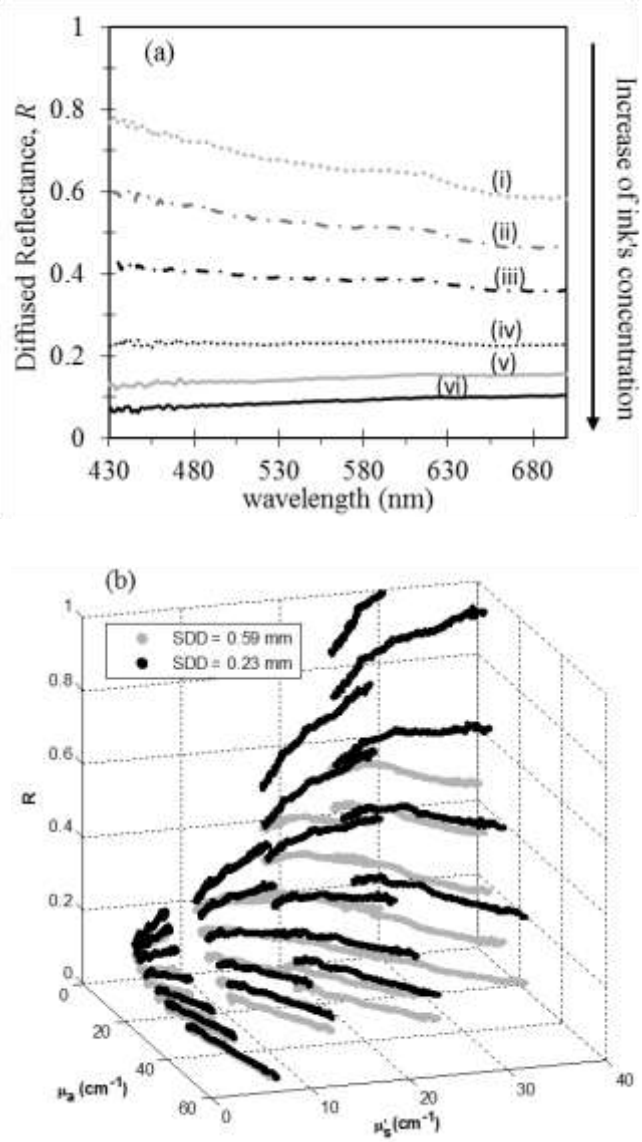

Fig. 5.2 (a) Examples of diffuse reflectance R for six different ink's concentrations while microsphere concentration remains constant and SDD = 0.23 mm, and (b) R as a sparse matrix mapped to optical property space $R(\mu_a(\lambda), \mu_s'(\lambda))$ for SDD = 0.23 mm and 0.59 mm. In (a), concentration of microsphere is 0.7% whereas concentrations of black India ink are 0.025%, 0.05%, 0.1%, 0.2%, 0.35% and 0.5%, corresponding to 6 spectra (i) to (vi). In (b), the sparse matrix represents reflectance data per SDD collected from 24 phantoms (6 ink concentrations x 4 microsphere concentrations).

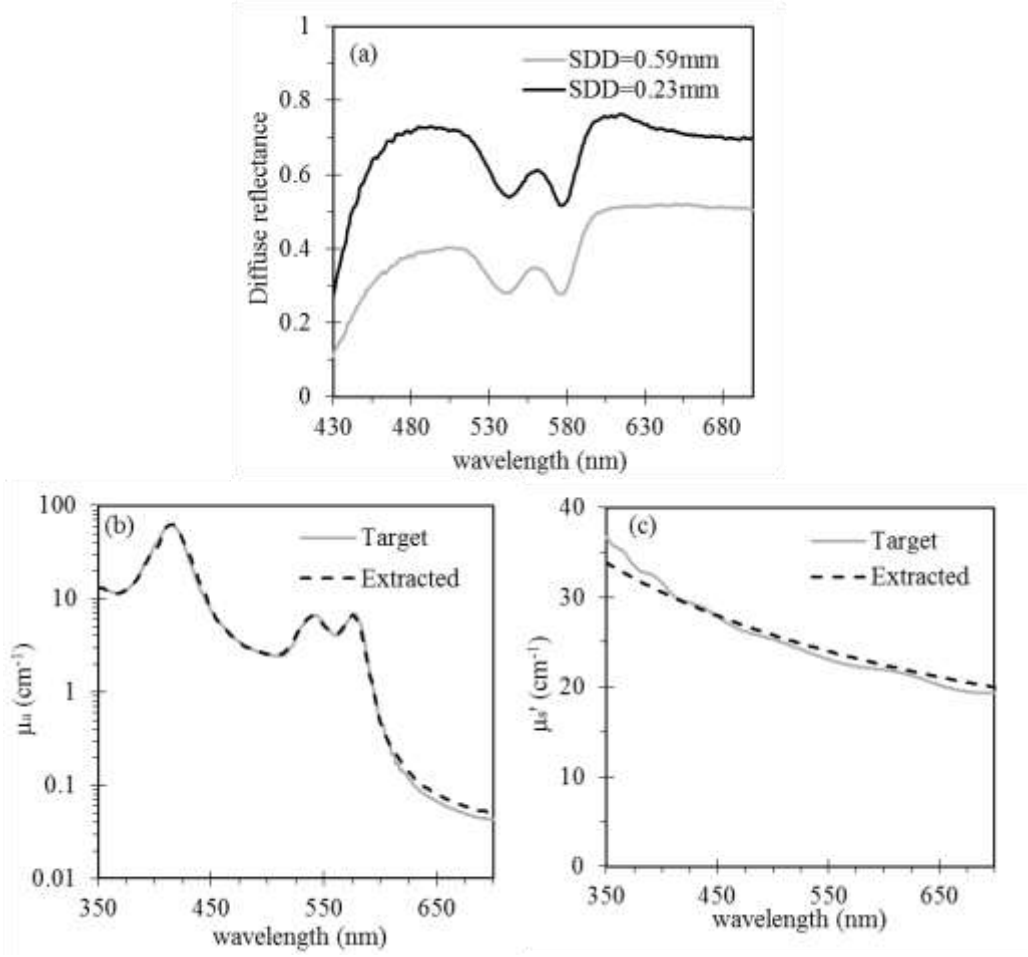

Fig. 5.3 An example of data analysis for a phantom with Hb concentration of 8 mg/ml, microsphere concentration of 0.7%: (a) Diffuse reflectance collected with fiber at SDD of 0.23 nmm and 0.89 mm, (b,c) Theoretical (target) vs. extracted optical properties. Eq. (5.1) and (5.2) were used to extrapolate data in 350-430 nm. In addition, f_1 and f_2 value of 3.3 ± 0.3 mg/ml and 96% ± 3 % was obtained by using Eq. (5.1).

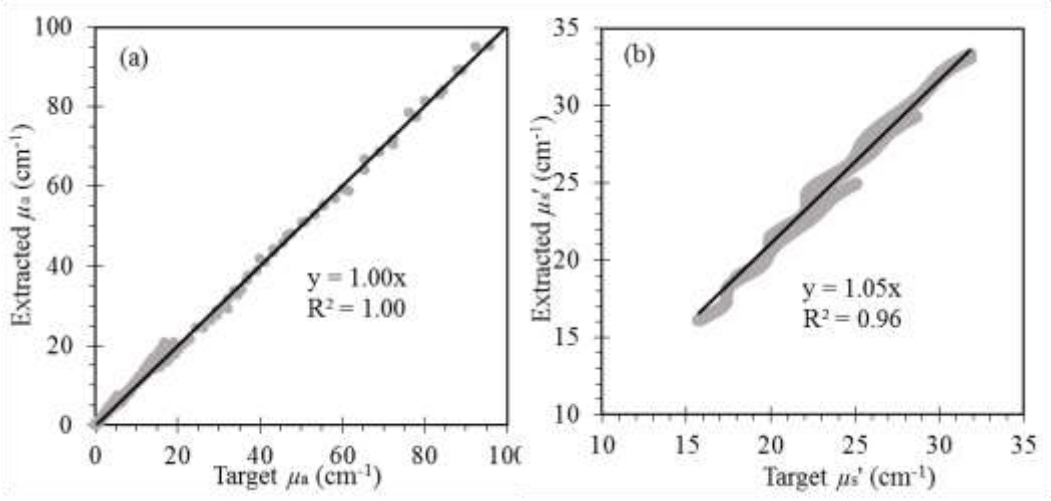

Fig. 5.4 Evaluation of LUT over ten different hemoglobin phantoms. In general, average percentage error of 9% and 6% was obtained for μ_a and μ_s', respectively.

5.3.2 Brain tissue measurements

Fig. 5.5 compares the diffuse reflectance [Fig. 5.5(a)], and optical properties [Fig. 5.5(b) and 5.5(c)] measured for the GBM group and the LGG group. In Fig. 5.5, data were averaged over all 12 GBM sites and 10 LGG sites. On average over the entire spectrum (Fig. 5.5), diffuse reflectance was 3.2 times higher, μ_a was 48% higher, and μ_s' was 140% higher for the GBM group. Data at 650 nm are also shown for comparison (Table 5.1). Note that 650 nm was selected because this is the region where blood absorption is small, and it is less likely that bleeding during surgery will affect tumor discrimination with optical measurement [35-39]. As shown in Table 5.1, at 650 nm diffuse reflectance was 2.8 times higher, μ_a was about 3 times higher, and μ_s' was 2.4 times higher for the GBM group. Fig. 5.6 shows the diffuse reflectance [Fig. 5.6(a)], and optical properties [Fig. 5.6(b)&(c)] at 650 nm for all GBM and LGG sites. If we define sensitivity as the percentage of GBM

sites that were correctly identified as GBM, and specificity as the percentage of LGG sites that were correctly identified as not GBM, the discrimination had a sensitivity of 100% (12/12) and specificity of 80% (8/10) if a cut-off at 20% was applied for diffuse reflectance at 650 nm to optimize the discrimination [Fig. 5.6(a)]. Sensitivity and specificity of 92% and 80% were achieved if a cut-off of 0.6 cm^{-1} was applied to μ_a at 650 nm [Fig. 5.6(b)]. These numbers were 100% and 90% if a cut-off of 10 cm^{-1} was applied to μ_s' at 650 nm [Fig. 5.6(c)]. Although oxygen saturation was calculated at 83.4±17.3% for GBM and 55.4±9.9% for LGG using Eq. (5.1), the results might be affected by long period air exposure of the brain tissue specimen, and were not used to optimize the discrimination for the *ex vivo* measurements.

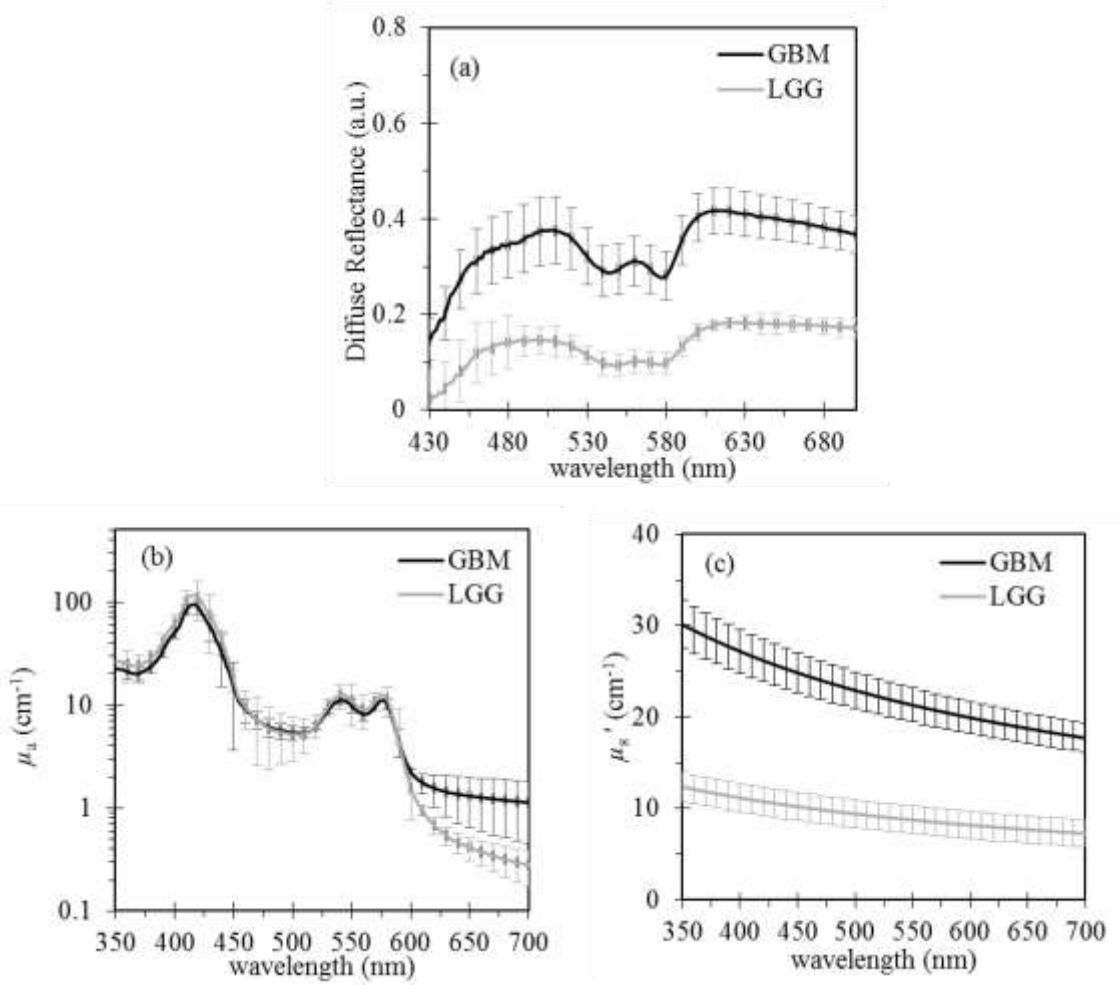

Fig. 5.5 LGG group vs. GBM group average spectral analysis: (a) diffuse reflectance, (b) absorption coefficient μ_a, (c) reduced scattering coefficient μ_s'. Data was averaged over all sites (12 GBM sites and 10 LGG sites) and error bars are the standard deviations.

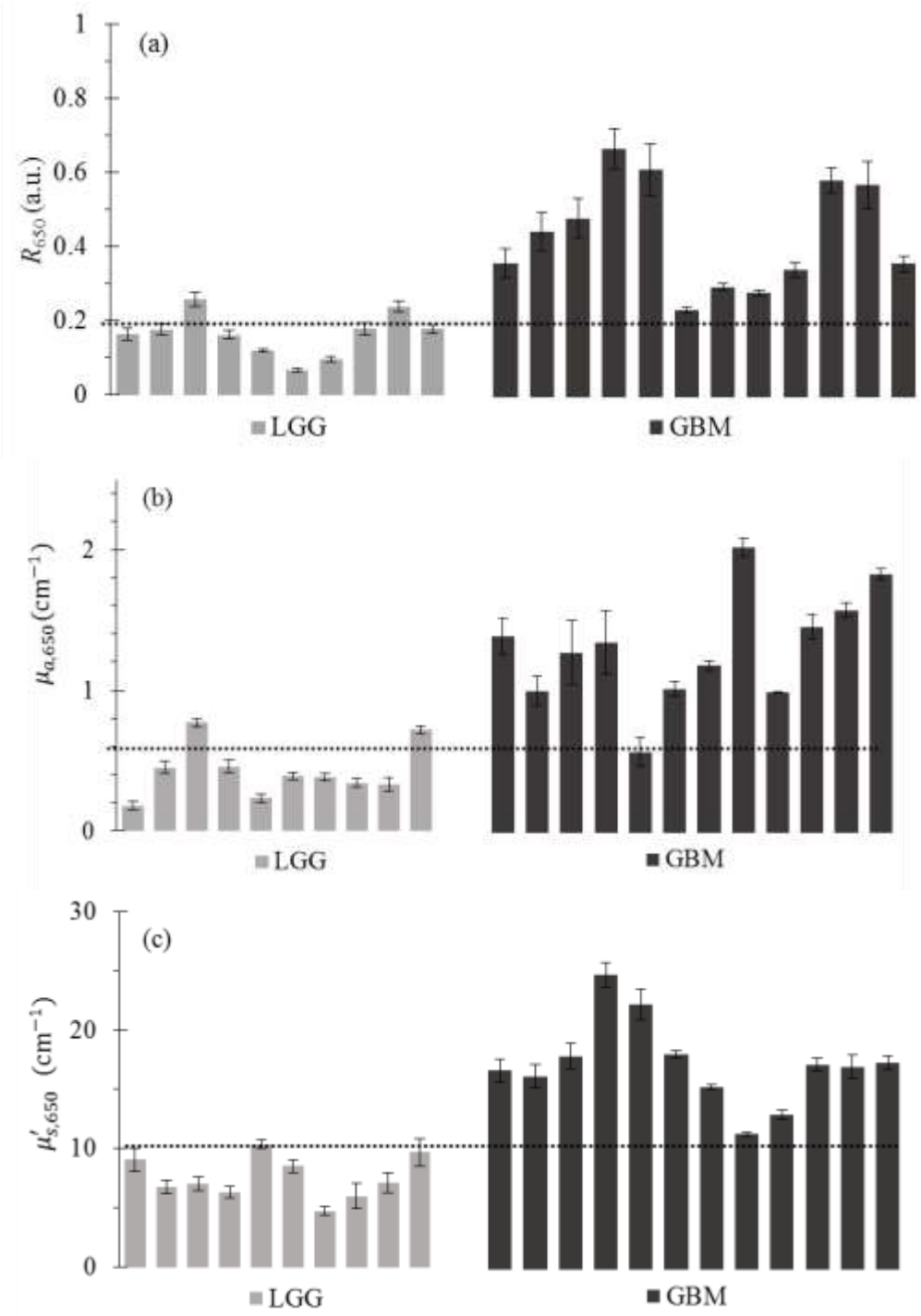

Fig. 5.6 LGG group (10 sites) vs. GBM group (12 sites): (a) Diffuse reflectance at 650 nm (R_{650}), (b) μ_a at 650 nm, and (c) μ_s' at 650nm. Data at 650 nm was selected for due to small blood absorption in this region, and thus it is less likely for blood absorption to affect tumor discrimination.

Fig. 5.7 shows the average fluorescence intensity with an emission peak at 460 nm (Fig. 7a), the average fluorescence lifetime [Fig. 5.7(b)], and the ratio of fluorescence and diffuse reflectance at 460 nm $(F/R)_{460}$ versus diffuse reflectance at 650 nm (R_{650}) for GBM sites and LGG sites. Although the measured fluorescence signal could identify the characteristic emission peak of brain tissues at 460 nm [Fig. 5.7(a)], the measured fluorescence signal alone is not able to discriminate tumor types due to high tissue absorption in this wavelength range. To enable tumor discrimination, a graph of the ratio of fluorescence to diffuse reflectance at the emission peak $(F/R)_{460}$ versus R_{650} was used instead [38,39]. If a cut-off of 20 for F_{460}/R_{460} was applied, sensitivity and specificity of 100% and of 90% was achieved. As shown in Fig. 5.7b and table 5.1, fluorescence lifetime alone was not able to discriminate GBM due to the high variation of life-time values, most likely caused by the low signal-to-noise ratio of the autofluorescence and high degree of heterogeneity in GBM [23]. Fig. 5.8 summarizes sensitivity and specificity when different parameters were used to discriminate GBM from LGG. In general, R_{650}, $\mu_s'_{,650}$ and ratio $(F/R)_{460}$ versus R_{650} could achieve discrimination with sensitivity of 100%. Combining diffuse reflectance and steady-state fluorescence show an increase in specificity from 80% to 90%.

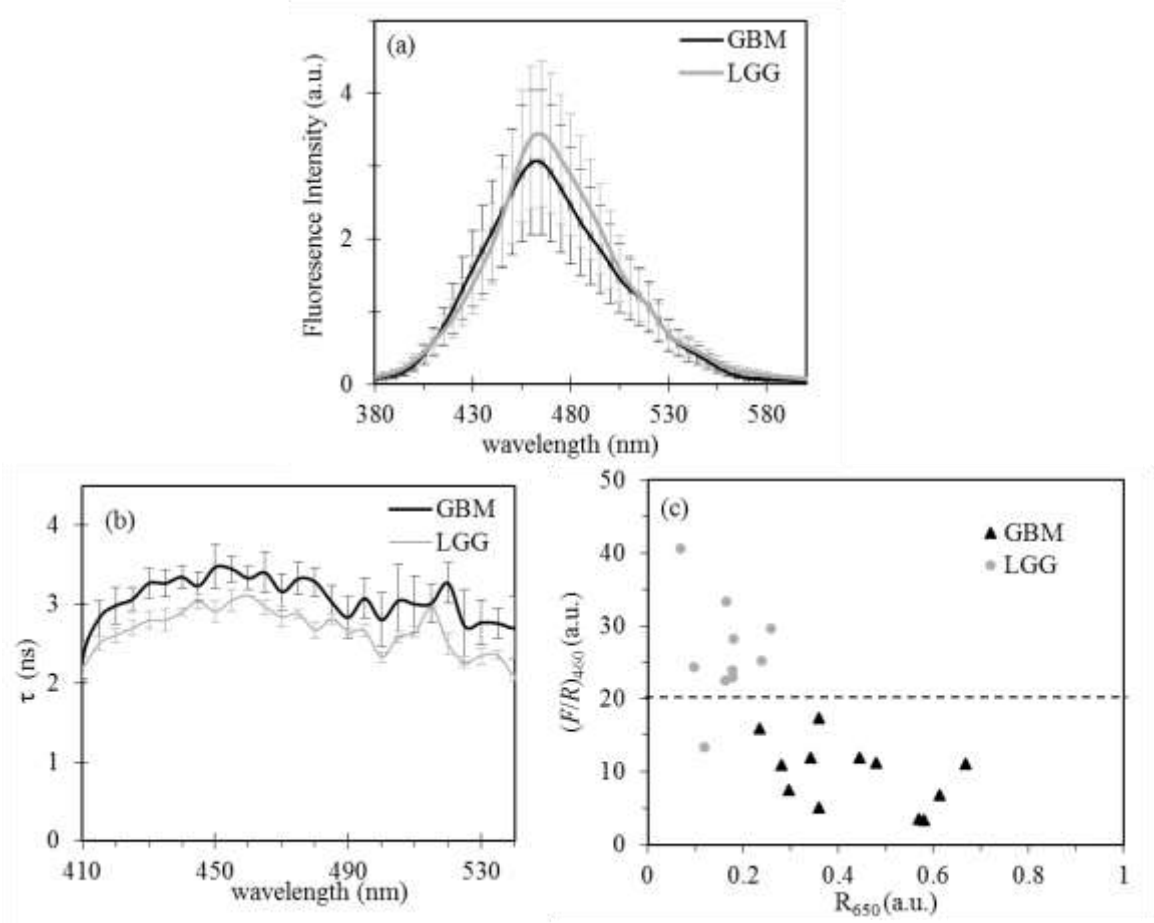

Fig. 5.7 LGG group vs. GBM group: (a) steady state fluorescence spectrum and (b) fluorescence life-time τ spectrum, (c) ratio of fluorescence to reflectance at 460 nm $(F/R)_{460}$ vs. reflectance at 650 nm (R_{650}). Fluorescence intensity has been normalized to integrating time and laser power corresponding to each measurement. In (a) and (b), data was averaged over all sites (12 GBM sites and 10 LGG sites) and error bars are the standard deviations.

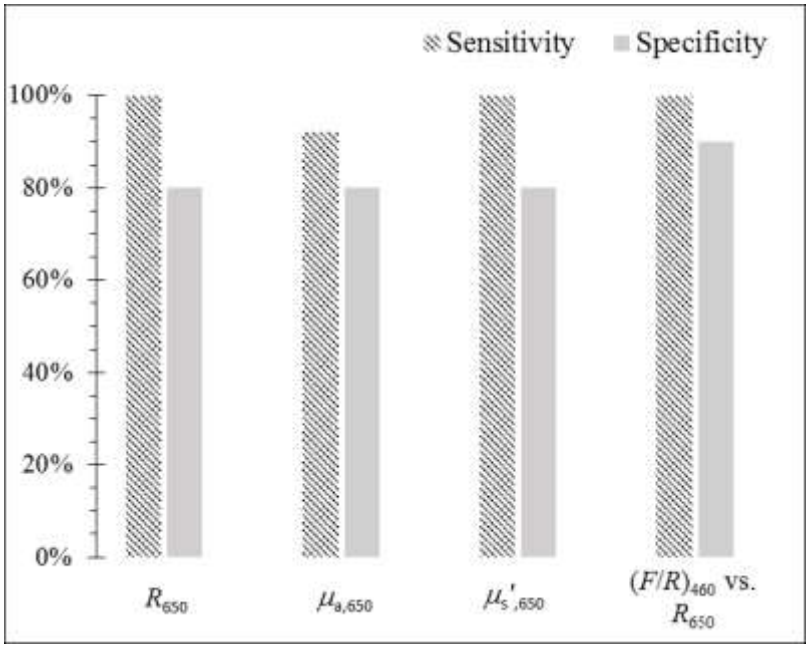

Fig. 5.8 Summary of sensitivity and specificity when using different parameters for GBM discrimination: diffuse reflectance at 650 nm (R_{650}), optical properties at 650 nm ($\mu_{a,650}$ and $\mu_s'_{,650}$), ratio $(F/R)_{460}$ vs. R_{650}

Table 5.1 Average over all GBM and LGG sites: diffuse reflectance at 650 nm (R_{650}), optical properties at 650 nm ($\mu_{a,650}$ and $\mu_s'_{,650}$), ratio of fluorescence to reflectance at 460 nm $(F/R)_{460}$, and fluorescence life-time at 460 nm (τ_{460}).

Parameter	GBM	LGG
R_{650} (a.u.)	0.44±0.03	0.16±0.01
$\mu_{a,650}$ (cm^{-1})	1.31±0.11	0.41±0.07
$\mu_s'_{,650}$ (cm^{-1})	18.8±1.4	7.7±0.7
$(F/R)_{460}$ (a.u.)	9.9±1.2	26.2±2.7
τ_{460} (ns)	3.2±0.3	3.1±0.05

5.4 Discussion and conclusion

Although the current LUT approach was similar to previous ones which aimed to study skin abnormality [**Error! Reference source not found.**], the current LUT covered optical

properties of human brain tissues and mucosal tissues. More specifically, μ_a range of 0.05-47 cm^{-1} and μ_s' range of 5-42 cm^{-1} were covered for wavelength range 430-700 nm. The developed inverse solution was thoroughly evaluated, and was able to retrieve optical properties with an average relative error of 9% for μ_a, and 6% for μ_s' using phantoms with known optical properties. Furthermore, the developed LUT was used to establish broadband optical properties for GBM and LGG (Fig. 5.5 and 5.6). Within the errors of the inverse solution, *ex vivo* measurements showed that μ_s' for GBM was 2.4 times higher than that for LGG [Fig. 5.5(c)]. Because cell density in GBM is two to three times higher than that in LGG [68,69], and because the scattering probability is proportional to cellular density [32], the GBM group is expected to have higher μ_s' than the LGG group. Furthermore, it is believed that GBM is highly vascular due to high degree of angiogenesis [70,71]. This may imply that GBM has higher blood content or higher μ_a. In fact, with the observation at 650 nm, the current study showed that μ_a was about 3 times higher in GBM than that in LGG [Fig. 5.6(b) and Table 5.1]. Combining diffuse reflectance and steady-state fluorescence did not change the sensitivity (100%), but increased the specificity from 80% to 90%. Similar to previous studies [35,38], the current study is limited by the small number of samples due to the limited number of glioma patients enrolled. Nevertheless, the current study has been able to discriminate GBM from LGG by accessing diffuse reflectance, optical properties measurement, and fluorescence (with diffuse reflectance). Although the measured oxygen saturation (f_2) values were higher than that in Asgari *et al.*'s study, they were in an agreeable trend so that GBM has higher f_2 than LGG, specifically 83.4±17.3% for GBM and 55.4±9.9% for LGG. These numbers were vs. 52±18% for GBM

and 36±21% in the previous study [46]. The difference in magnitude of f_2 between the two studies is mainly due to the fact that the current samples have been exposed to air during *ex vivo* measurements while intraoperative measurements were performed in the previous study. Meanwhile, it is believed that arteriovenous shunts and metabolic shunts can cause more oxygen than required in GBM, and are responsible for high oxygen saturation levels in GBM [72]. The preliminary results of the *ex vivo* measurements indicates that the current technique has the potential for *in vivo* discrimination of GBM by accessing the tumor's optical characteristics including diffuse reflectance, steady state fluorescence, optical properties, and possibly oxygen saturation.

Acknowledgements

This project is supported in part by the Natural Sciences and Engineering Research Council (NSERC) of Canada, the Ontario Centres of Excellence, the Ontario Ministry of Research and Innovation, and the Canadian Cancer Society Research Institute (CCSRI). QF holds the Canada Research Chair in Biophotonics at McMaster University.

Vinh Nguyen Du Le is a PhD student in the Radiation Sciences Graduate Program at McMaster University. He received a Bachelor's (2009) and a Master's degree (2010) in Biomedical Engineering from the Catholic University of America (Washington, DC). He was a Research Engineer in the Optical Diagnostics Laboratory at the Center for Devices and Radiological Health of Food and Drug Administration (Silver Spring, MD) from 2010 to 2012.

John Provias received the M.D. degree from McMaster University. He is currently an Associate Professor in the Pathology and Molecular Medicine, McMaster University. His is also the Neuropathologist for Hamilton Regional Cancer Centre.

Naresh Murty received the B.Sc. degree in biology from Dalhousie University and the M.D. degree from Kasturba Medical College (India). He is currently an Associate Professor

in the Division of Neurosurgery, McMaster University. He is also the Head of neurosurgery service at Hamilton General Hospital.

Michael S. Patterson is the director of medical physics at Juravinski Cancer Centre. He received a B.Sc. degree from Queen's University, a M.Sc. degree from McMaster University, and a Ph.D. degree from the University of Toronto.

Thomas J. Farrell is a Medical Physicist at the Juravinski Cancer Centre and the chair of the Medical Physics department at McMaster University. He received a Ph.D. degree from McMaster University.

Joseph E. Hayward is a Medical Physicist at the Juravinski Cancer Centre and an Associate Professor of the Medical Physics department at McMaster University. He received a Ph.D. degree in lasers and electro-optics in Engineering Physics from McMaster University.

Qiyin Fang is an Associate Professor of Engineering Physics and the chair of Biophotonics at McMaster University. He received a B.Sc. degree in physics from Nankai University, a MSc. Degree in Applied Physics and a Ph.D. degree in Biomedical Physics from East Carolina University.

William McMillan is an Associate Professor at McMaster University's Department of Oncology. He received the B.Sc. and M.Sc. degree from McMaster University, a BA from Queen's University and a MB.CHB degree from University College.

References

1. Q. T. Ostrom et al. "American Brain Tumor Association Adolescent and Young Adult Primary Brain and Central Nervous System Tumors Diagnosed in the United States in 2008-2012." Neuro-oncology **18** (1), i1-i50 (2016).

2. J. G. Scott et al., "Aggressive treatment is appropriate for glioblastoma multiforme patients 70 years old or older: a retrospective review of 206 cases, " Neuro-oncology **nor005** (2011).

3. A. Agnihotri et al., "Glioblastoma, a brief review of history, molecular genetics, animal models and novel therapeutic strategies,"Arch. Immunol. Ther. Exp. **61**, 25-41(2013).

4. K. R. Hess et al., "Adult glioma incidence trends in the United States, 1977–2000," Cancer **101** 2293-2299 (2004).

5. Golla H et al. "Glioblastoma multiforme from diagnosis to death: a prospective, hospital-based, cohort, pilot feasibility study of patient reported symptoms and needs," Supportive Care in Cancer **22** 3341-3352 (2014).

6. M. E. Hegi et al., "MGMT gene silencing and benefit from temozolomide in glioblastoma," New England J. Med." **352**, 997-1003 (2005).

7. R Stupp et al., "Radiotherapy plus concomitant and adjuvant temozolomide for glioblastoma New England J. Med.," **352** 987-996 (2005).

8. N. Sanai et al., "An extent of resection threshold for newly diagnosed glioblastomas: clinical article," J. Neurosurg. **115** 3-8 (2011).

9. J. H. Adams, D. I. Graham, and D. Doyle, "Brain biopsy: the smear technique for neurosurgical biopsies" J. Roy. Soc. Med. **75** 61 (1982).

10. A. Alrawi, J. D. Trobe, M. Blaivas, D. C. Musch, "Brain biopsy in primary angiitis of the central nervous system, " Neurology **53** 858 (1999).

11. D. Ricard et al., "Primary brain tumours in adults," The Lancet **379** 1984-1996 (2012).

12. O. Solheim et al., "Ultrasound-guided operations in unselected high-grade gliomas-overall results, impact of image quality and patient selection," Acta neurochirurgica **152** 1873-1886 (2010).

13. P. M. Matthews, M. Wylezinska, T. Cadoux-Hudson, "Novel approaches to imaging brain tumors," Hemat. Clin. North America **15** 609-630 (2001).

14. M Lee et al. "The motor cortex shows adaptive functional changes to brain injury from multiple sclerosis," Annals of Neurology **47** 606-613 (2000).

15. S. Sathornsumetee, J. N. Rich, and D. A. Reardon, "Diagnosis and treatment of high-grade astrocytoma," Neurologic Clinics **25** 1111-1139 (2007).

16. L. M. DeAngelis, "Brain tumors," New England J. Med. **344** 114-123 (2001).

17. G. Zonios et al., "Diffuse reflectance spectroscopy of human adenomatous colon polyps in vivo," Appl. Opt. **38** 6628-6637(1999).

18. J. R. Mourant, "Spectroscopic diagnosis of bladder cancer with elastic light scattering," Lasers Surg. Med. **17** 350-357(1995).

19. A. Amelink, H. Sterenborg, M. Bard, S. A. Burgers, "In vivo measurement of the local optical properties of tissue by use of differential path-length spectroscopy," Opt. Let **29** 1087-1089 (2004).

20. S. K. Chang, D. Arifler, R. Drezek, M. Follen, and R. Richards-Kortum, "Analytical model to describe fluorescence spectra of normal and preneoplastic epithelial tissue: comparison with Monte Carlo simulations and clinical measurements," J. Biomed. Opt. **9** 511-522 (2004).

21. S. K. Chang, N. Marin, M. Follen, and R. Richards-Kortum, "Model-based analysis of clinical fluorescence spectroscopy for in vivo detection of cervical intraepithelial dysplasia," J. Biomed. Opt. **11** 024008-024008 (2006).

22. P. V. Butte et al., "Intraoperative delineation of primary brain tumors using time-resolved fluorescence spectroscopy," J. Biomed. Opt **15**(2) 027008-027008 (2010).

23. W. H. Yong, et al., "Distinction of brain tissue, low grade and high grade glioma with time-resolved fluorescence spectroscopy," Frontiers in Biosciences, 11: 1255-1263 (2006).

24. T. J. Pfefer et al., "Reflectance-based determination of optical properties in highly attenuating tissue," J. Biomed. Opt. **8** 206-215(2003).

25. A. J. Welch, M. J. C. van Gemert, and W. M. Star, "Definitions and overview of tissue optics," In *Optical thermal response of laser irradiated tissue*, eds. A J Welch & M J C van Gemert, 2nd edn (Springer Science & Business Media, NY, 2011)

26. S. L Jacques, and S. A. Prahl. *Introduction to biomedical optics*. Available from: <http://omlc.org/education/ece532/index.html>

27. R. Graaff, J. G. Aarnoudse, F. de Mul, and J. W. Jentink, "Similarity relations for anisotropic scattering in absorbing media," Opt. Eng. **32** 244-252 (1993).

28. R. Drezek et al., "Understanding the contributions of NADH and collagen to cervical tissue fluorescence spectra: modeling, measurements, and implications," J. Biomed. Opt. **6** 385-396(2001).

29. S. L. Jacques, "Optical properties of biological tissues: a review," Phys. Med. Biol. **58** R37 (2013).

30. A. Kim, and B. C. Wilson, "Measurement of ex vivo and in vivo Tissue Optical Properties: Methods and Theories" In *Optical thermal response of laser irradiated tissue*, eds. A J Welch & M J C van Gemert, 2nd edn (Springer Science & Business Media, NY, 2014)

31. R. Drezek, A. Dunn, and R. Richards-Kortum, "Light scattering from cells: finite-difference time-domain simulations and goniometric measurements," Appl. Opt. **38**(16), 3651-3661(1999).

32. J. R. Mourant, et al., "Mechanisms of light scattering from biological cells relevant to noninvasive optical-tissue diagnostics." Applied optics 37(16) (1998): 3586-3593.

33. A. Dellas et al., "Angiogenesis in cervical neoplasia: microvessel quantitation in precancerous lesions and invasive carcinomas with clinicopathological correlations," Gynecol. Oncol. **67** 27-33(1997).

34. I. Pavlova et al., "Microanatomical and Biochemical Origins of Normal and Precancerous Cervical Autofluorescence Using Laser-scanning Fluorescence Confocal Microscopy," Photochem. Photobiol. **77** 550-555 (2003).

35. W. C. Lin et al., "Diffuse reflectance spectroscopy for in vivo pediatric brain tumor detection," J. Biomed. Opt. **15**(6), 061709-061709 (2010).

36. Z. Volynskaya et al., "Diagnosing breast cancer using diffuse reflectance spectroscopy and intrinsic fluorescence spectroscopy." J. Biomed. Opt. **13**, 024012-024012 (2008).

37. M. G. Müller, I. Georgakoudi, Q. Zhang, J. Wu, and M. S. Feld, "Intrinsic fluorescence spectroscopy in turbid media: disentangling effects of scattering and absorption," Appl. Opt. **40**, 4633-4646 (2001).

38. W. C. Lin et al., "In vivo brain tumor demarcation using optical spectroscopy," Photochem. Photobiol. **73**(4) 396-402 (2001).

39. S. A. Toms et al., "Intraoperative optical spectroscopy identifies infiltrating glioma margins with high sensitivity." Neurosurgery **57** 382-3914 (2005).

40. P. A. Valdés et al., "Combined fluorescence and reflectance spectroscopy for in vivo quantification of cancer biomarkers in low-and high-grade glioma surgery." J. Biomed. Opt. **16** 116007-11600714 (2011).

41. W. Stummer et al., "Fluorescence-guided surgery with 5-aminolevulinic acid for resection of malignant glioma: a randomised controlled multicentre phase III trial," Lancet Oncol. **7**(5), 392–401 (2006).

42. W. Stummer, et al. "Extent of resection and survival in glioblastoma multiforme: identification of and adjustment for bias." Neurosurgery **62**(3), 564-576 (2008).

43. T. O. McBride, B. W. Pogue, E .D Gerety, S. B. Poplack, U. L. Osterberg, and K. D. Paulsen, " Spectroscopic diffuse optical tomography for the quantitative assessment of hemoglobin concentration and oxygen saturation in breast tissue, Appl. Opt. **38** 5480-5490 (1999)

44. R. Reif, O. A'Amar, and I. J. Bigio," Analytical model of light reflectance for extraction of the optical properties in small volumes of turbid media," Appl. Opt. **40** 7317-7328 (2007).

45. N. Rajaram, T. J. Aramil, K. Lee, J. S. Reichenberg, T. H. Nguyen, and J. W. Tunnell, "Design andvalidation of a clinical instrument for spectral diagnosis of cutaneous malignancy," Appl. Opt. **49** 142-152 (2010).

46. S. Asgari, H. J. Röhrborn, T. Engelhorn, and D. Stolk, " Intra-operative characterization of gliomas by near-infrared spectroscopy: possible association with prognosis," Acta Neurochirurgica **145** 453-460(2003).

47. S. C. Gebhart, W. C. Lin, and A. Mahadevan-Jansen," In vitro determination of normal and neoplastic human brain tissue optical properties using inverse adding-doubling," Phys. Med. Biol. **51** 2011-2027 (2006).

48. N. Rajaram, T. H. Nguyen, and J. W. Tunnell, "Lookup table–based inverse model for determining optical properties of turbid media," J. Biomed. Opt. **13** 050501-050501 (2008)

49. M. Friebel, A. Roggan, G. Müller, and M. Meinke, "Determination of optical properties of human blood in the spectral range 250 to 1100nm using Monte Carlo

simulations with hematocrit-dependent effective scattering phase functions," J. Biomed. Opt. **11** 034021-034021 (2006).

50. V. N. Du Le, Z. Nie, J. E. Hayward, T. J. Farrell, and Q. Fang, "Measurements of extrinsic fluorescence in Intralipid and polystyrene microspheres," Biomed. Opt. Express **5** 2726-2735 (2014).

51. V. N. Du Le, Q. Wang, T. Gould, J. C. Ramella-Roman, and T. J. Pfefer," Vascular contrast in narrow band and white light imaging," Appl. Opt. **53** 4061-4071 (2014).

52. B. Yu, A. Shah, V. K. Nagarajan, and D. G. Ferris," Diffuse reflectance spectroscopy of epithelial tissue with a smart fiber-optic probe," Biomed. Opt. Express **5** 675-689 (2014).

53. Q. Liu, C. Zhu, and N. Ramanujam, "Experimental validation of Monte Carlo modeling of fluorescence in tissues in the UV-visible spectrum," J. Biomed. Opt. **8** 223-236 (2003).

54. B. W. Pogue and M. S. Patterson, "Review of tissue simulating phantoms for optical spectroscopy, imaging and dosimetry," J. Biomed. Opt. **11** 041102 (2006)

55. T. R. Wagner, W. G. Houf, and F. P. Incropera, "Radiative property measurements for India ink suspensions of varying concentration," Solar Energy **25** 549-554 (1980).

56. H. Xu and M. Patterson, "Determination of the optical properties of tissue-simulating phantoms from interstitial frequency domain measurements of relative fluence and phase difference," Opt. Express **14** 6485-6501(2006).

57. I. Barman, N. C. Dingari, N. Rajaram, J. W. Tunnell, R. R. Dasari, M. S. Feld, " Rapid and accurate determination of tissue optical properties using least-squares support vector machines," Biomed. Opt. Express **2** 592-599(2011).

58. S. L. Jacques, R. Samatham, N. Choudhury, "Rapid spectral analysis for spectral imaging," Biomed. Opt. Exp., **1**(1) 157-164 (2010).

59. M. S. Twardowski, E. Boss, J. M. Sullivan, P. L. Donaghay, "Modeling the spectral shape of absorption by chromophoric dissolved organic matter," Marine Chemistry **89**(1), 69-88 (2004).

60. X. Zhong, X. Wen, D. Zhu, "Lookup-Table-based inverse model for human skin reflectance spectroscopy: two-layered Monte Carlo simulations and experiments," Opt. Express **22**(2), 1852-1864 (2014).

61. P. R. Bargo et al., "In vivo determination of optical properties of normal and tumor tissue with white light reflectance and an empirical light transport model during endoscopy," J. Biomed. Opt. **10**, 03401815(2005)

62. S. Prahl," Tabulated molar extinction coefficient for hemoglobin in water," Oregon Medical Laser Center **4** (1998).

63. N. D. Louis et al., "The 2007 WHO classification of tumours of the central nervous system," Acta neuropathologica **114**(2), 97-109 (2007).

64. V. N. Du Le, M. S. Patterson, T. J. Farrell, J. E. Hayward, and Q. Fang, "Experimental recovery of intrinsic fluorescence and fluorophore concentration in the presence of hemoglobin: spectral effect of scattering and absorption on fluorescence," J. Biomed. Opt. **20**(12), 127003-127003 (2015).

65. Z. Nie et al., "Integrated Time-resolved Fluorescence and Diffuse Reflectance Spectroscopy Instrument for Intraoperative Detection of Brain Tumor Margin," Sel. Topics in Quantum Electronics, IEEE J. **22**(3), 6802109 (2016).

66. Y. Yuan et al., "High throughput AOTF-based time-resolved fluorescence spectrometer for optical biopsy", Opt. Let. **34**(7), 1132-1134 (2009).

67. D. J. Cappon, T. J. Farrell, Q. Fang, J. E. Hayward, "A Novel Fibre Optic Probe Design and Optical Property Recovery Algorithm for Optical Biopsy of Brain Tissue," J. Biomed. Opt. **18**(10),107004-107004, (2013).

68. K. M. Gauvain et al., "Evaluating pediatric brain tumor cellularity with diffusion-tensor imaging," American J. Roentgenology **177**(2), 449-454 (2001).

69. D. J. Brat et al., "Pseudopalisades in glioblastoma are hypoxic, express extracellular matrix proteases, and are formed by an actively migrating cell population," Cancer Research **64**(3), 920-927 (2004).

70. P. P. Pramanik et al. "Hypercellularity Components of Glioblastoma Identified by High b-Value Diffusion-Weighted Imaging." International J. Rad. Oncol. Biol. Phys. **92** 811-819 (2015).

71. S. Das, and P. A. Marsden, "Angiogenesis in glioblastoma." New England Journal of Medicine **369** 1561-1563(2013).

72. J. G. Ojemann et al., "Increased functional vascular response in the region of a glioma," J. Cerebral Blood Flow & Metabolism **18**, 148-153 (1998).

Chapter 6: Concluding Remarks

6.1 Achievement summary

Advancement in technologies for real-time detection of brain tumor can offer intraoperative guidance for neurosurgeons to perform a more accurate and complete surgical removal [1,2]. Although significant developments have been made to the conventional diagnostic technologies such as magnetic resonance imaging (MRI) and ultrasound, translation of these technologies to the operating room still remains challenges such as high capital cost, low accuracy, or prolonged operative time (Chapter 2). Diffuse reflectance spectroscopy (DRS) and fluorescence spectroscopy are relatively new technologies that have the potential to guide surgeons to detect malignant tissues, and may be able to overcome the challenges for neurosurgical application of the current conventional imaging techniques.

As mentioned in Chapter 1, although many studies have combined both DRS and fluorescence spectroscopy to improve accuracy in detecting tumors in human breast, skin, oral cavity, and cervix, only a few studies have used both techniques to study brain tissues whereas optical properties analysis across a range of glioma histologies have not been established to allow intraoperative differentiation of GBM and LGG for accurate and complete surgical resection. Therefore, more investigations are needed before the integrated DRS and fluorescence spectroscopy systems can be translated to the operating room setting for patient care.

In this dissertation, we have investigated the potential of the integrated DRS and fluorescence spectroscopy system in identifying brain tumors by: (i) developing fast and simple experimental algorithms to recover intrinsic fluorescence, to extract tissue optical properties, and (ii) performing *ex vivo* measurements of brain tissue specimens, specifically GBM and LGG.

As for the algorithms, prior to the work in Chapter 4 and 5, the recovery of intrinsic fluorescence in the research community was mostly performed with the aid of Monte Carlo simulations whereas the measurement of brain tissue optical properties was usually performed using integrating spheres coupled inverse adding doubling model. As discussed in Chapter 2, 4 and 5, such methods could be either time-consuming or not applicable for neurosurgery. To overcome such limitations, this dissertation has established experimental approaches that are simple, less time-consuming, and more applicable for real-time brain tissue measurement. Such approaches were extensively validated via experimental measurements of optical phantoms with controlled fluorescence properties and optical properties. In Chapter 4, the optical fiber's experimental collection efficiency was calculated and used to recover fluorescence peak in optical phantoms with average error of 3%. In Chapter 5, a combination of fitting algorithms and an experimental look-up table (LUT) were developed to extract optical properties with an average error of 12% and 6% for μ_a and μ_s', respectively. Furthermore, the experimental results of Intralipid fluorescence properties in Chapter 3 have brought to researchers' attention that careful treatment must be made when using lipid to produce optical phantoms for system calibration, and that polymer microspheres are recommended over Intralipid given available resources.

As for *ex vivo* measurements, a total of 21 data points were collected from seven glioma patients (Chapter 5). Histological analysis confirmed that three were LGG and four were GBM. Prior to this work, optical properties of LGG and GBM were usually averaged together and reported as optical properties of glioma group whereas separate optical observation for GBM and LGG was not available [3,4]. In this dissertation, it was found that, μ_s' is 2.4 times higher in GBM considering any wavelengths while μ_a was 48% higher within 350-700 nm. If wavelength at 650 nm was considered, on average, μ_a was about 3.2 times higher in GBM. These results are consistent with neoplastic progression described in Chapter 2, which likely cause an increase in cellular density and cell nuclei size (source of scatterers) [5,6] and an increase in microvessel proliferation or hemoglobin concentration (source of absorbers) [7]. Using both diffuse reflectance and fluorescence signal (Chapter 5), the sensitivity of 100% and specificity of 90% was obtained in differentiating GBM from LGG.

Given the flexibility of the current approach, it can also be used to study tumor progression in the breast. In fact, the current approach is being applied to study breast cancer during *ex vivo* measurement of breast tissue specimens [8], and the results will be reported in a near future. Meanwhile, using similar integrated systems, previous studies have shown that combining DRS and fluorescence spectroscopy could archive an accuracy of above 95% in differentiating invasive ductal carcinomas from normal breast tissues [9-11], and thus indicated the potential application of the current integrated system in breast cancer studies.

6.2 Future work

It is known that changes at cellular levels and tissue levels occur during tumor progression (Chapter 2). It is also known that the magnitude of scattering coefficients reflects the size and concentration of scatterer, and the magnitude of absorption coefficients reflects the level of disorganized vasculature (Chapter 2). Although this thesis was able to establish the relation between optical properties and glioma progression (from LGG to GBM) at reasonable trends, a quantitative relation between changes of cellular components and dynamic changes of optical properties have not been established. Such analysis will be useful in identifying different histological appearances of GBM or high grade glioma (i.e. different levels of cell density or of disorganized vasculature and microvessel proliferation) by accessing its optical properties. This can be accomplished if histopatholgical images of the brain tissue specimens were made available for further analysis, and if immunohistochemistry analysis is performed to access micro-vessel density.

In addition, although an experimental method was developed to recover intrinsic fluorescence on controlled phantoms, a quantitative relation between fluorescence and fluorphore concentration in brain tissue was not established. This will be accomplished if enzymic analysis of GBM and LGG is performed to extract and confirm the concentration of NADH in brain tissues [12]. For example, enzymic analysis of breast tissues showed that concentration of NADH concentration is about 0.82±0.33 μM/g in malignant breast tissues and about 0.44±0.25 μM/g in normal breast tissue [12]. Such quantitative analysis helped understanding spectroscopic observations which showed that the fluorescence intensity

from malignant breast tissue was about 2 times higher than that from the normal and benign tumor tissue [13].

Because the current sensitivity and specificity was optimized from a small sample size of seven glioma patients, it might undermine the reliability of the current approach although it was extensively validated on optical phantoms. In future work, more *ex vivo* measurements can be performed to increase the sample size.

Furthermore, in order to obtain a sufficient fluorescence signal to noise ratio in *ex vivo* brain specimen (Chapter 4 and 5), exposure time of spectrometers (UV-NIR-200, StellarNet Incorporation, Tampa, FL) was set to a minimum of 1 minute. This may limit the number of data collected during *in vivo* studies. To improve fluorescence signal to noise ratio, and to reduce the waiting time, a spectrograph coupled a charge couple detector camera can be used to replace current spectrometers [9].

6.3 Conclusion

In conclusion, this thesis successfully calibrated the integrated DRS and fluorescence spectroscopy system on the developed optical phantom models, established experimental models to extract brain tissue optical properties and optimized the system's sensitivity and specificity in differentiating GBM from LGG. The preliminary *ex vivo* results are promising, and indicate that the current technique has the potential for future *in vivo* detection of GBM and LGG, and that it might be a promising tool to aid neurosurgeons to determine the extent of surgical resection of glioma. Additional *ex vivo* measurements,

advancement in instrumentation, and tissue processing will make it more feasible for the translation from the current *ex vivo* studies to future *in vivo* studies.

References

1. J. Wadley, N. Kitchen, and D. Thomas, "Image-guided neurosurgery." Hospital medicine, **60**(1) 34-38(1999).

2. C. B. Lumenta, H. Gumprecht, and M. J. Krammer, "Image-guided neurosurgery," In Neurosurgery, pp. 579-590 (Springer Berlin Heidelberg, 2010).

3. W. C. Lin et al., "In vivo brain tumor demarcation using optical spectroscopy," Photochem. Photobiol. **73**(4), 396-402 (2001).

4. S. A. Toms et al., "Intraoperative optical spectroscopy identifies infiltrating glioma margins with high sensitivity." Neurosurgery **57**, 382-3914 (2005).

5. R. Drezek et al., "Light scattering from cervical cells throughout neoplastic progression: influence of nuclear morphology, DNA content, and chromatin texture, " J. Biomed. Opt. **8** 7–16 (2003).

6. D. Arifler et al., "Light scattering from normal and dysplastic cervical cells at different epithelial depths: finite-difference time-domain modeling with a perfectly matched layer boundary condition, " J. Biomed. Opt. **8** 484-494 (2003).

7. G. Zonios, L. T. Perelman, V. Backman, R. Manoharan, M. Fitzmaurice, J. V. Dam, and M. S. Feld, "Diffuse reflectance spectroscopy of human adenomatous colon polyps in vivo," Appl. Opt. **38** 6628 (1999).

8. N. Shalaby, A. Al-Ebraheem, V. N. Du Le, Q. Fang, T. Farrell, M. Farquharson "Differentiation of Tumour and Normal Breast Tissue using an Optical Spectroscopy System", McMaster's Radiology Research Day" (Oral presentation).

9. Z. Volynskaya et al., "Diagnosing breast cancer using diffuse reflectance spectroscopy and intrinsic fluorescence spectroscopy." J. Biomed. Opt. **13**, 024012-024012 (2008).

10. M. D. Keller al. "Autofluorescence and diffuse reflectance spectroscopy and spectral imaging for breast surgical margin analysis." Lasers Surg. Med. **42**, 15-23 (2010).

11. V. Sharma et al. "Auto-fluorescence lifetime and light reflectance spectroscopy for breast cancer diagnosis: potential tools for intraoperative margin detection." Biomedical optics express **3**, 1825-1840 (2012).

12. A. Uppal, and P. K. Gupta. "Measurement of NADH concentration in normal and malignant human tissues from breast and oral cavity." Biotechnology and applied biochemistry **37** 45-50(2003).

13. P. K. Gupta, S. K. Majumder, and A. Uppal. "Breast cancer diagnosis using N2 laser excited autofluorescence spectroscopy." Lasers Surg. Med. **21**(5), 417-422 (1997).

Appendix

A.1 Data analysis software in Chapter 3

Mie theory was used to calculate scattering properties of polymer microsphere. The program was developed in the MATLAB® (2013a, MathWork). Inputs are concentration of particle in gram per 100 ml of suspension solution (X), wavelength (λ), and sphere diameter (d). Principal outputs are scattering efficiency, (Q_s) scattering coefficient (μ_s), anisotropy (g), and reduced scattering coefficient (μ_s'). Fig. A.1 shows the developed graphical user interface of the program and Fig. A.2 shows the flowcharts of the data preprocessing. Note that to obtain the unit of cm^{-1} for μ_s and μ_s', units of inputs are converted correspondingly.

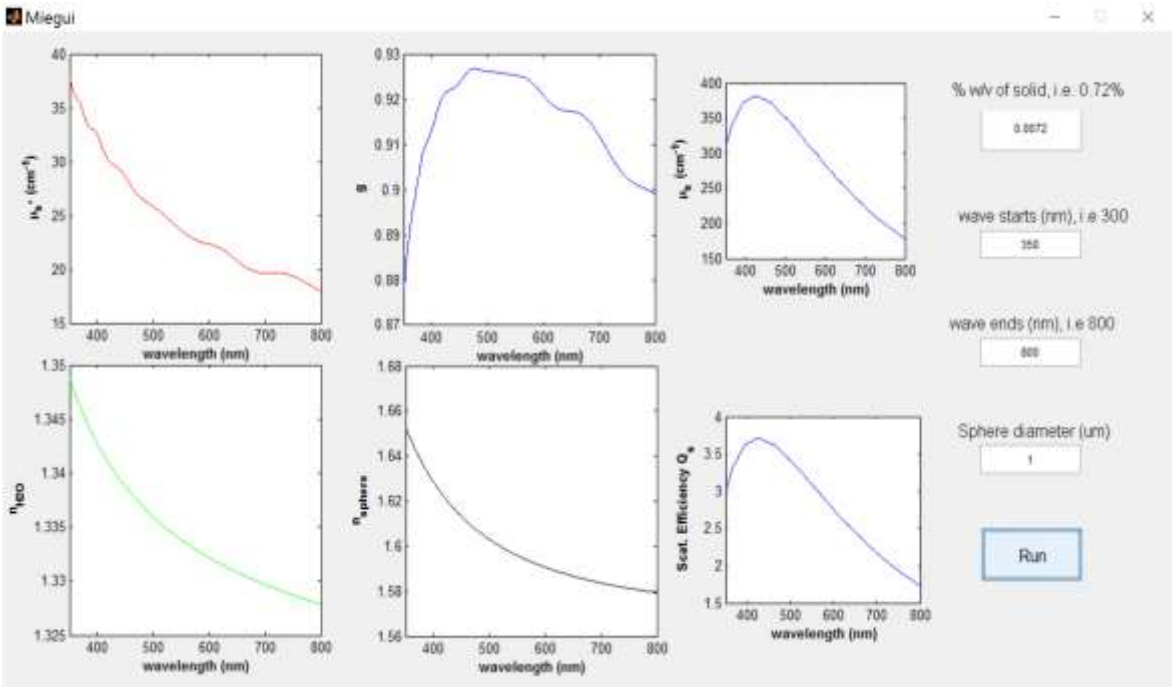

Fig. A.1 Software user interface for Mie theory calculation of scattering properties of polymer microsphere, including the data preprocessing and graphing.

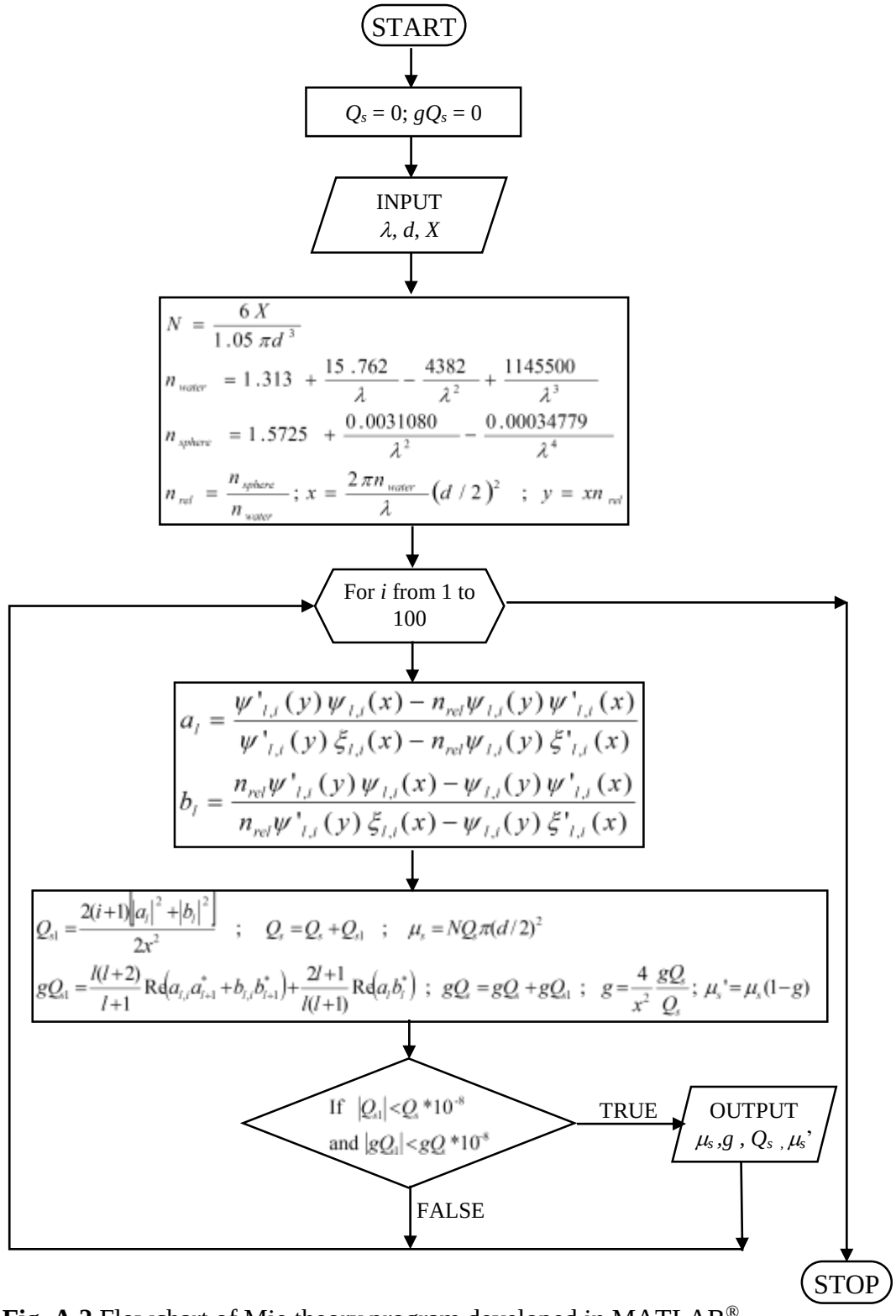

Fig. A.2 Flowchart of Mie theory program developed in MATLAB®

In Fig. A.2, a_l and b_l are Mie coefficients used to describe the amplitudes of the scattered field, and are calculated using MATLAB's built-in double-precision Bessel functions. Details derivation of Mie theory can be found in ref [23] of Chapter 3.

A.2 System schematic view and clinical set-up

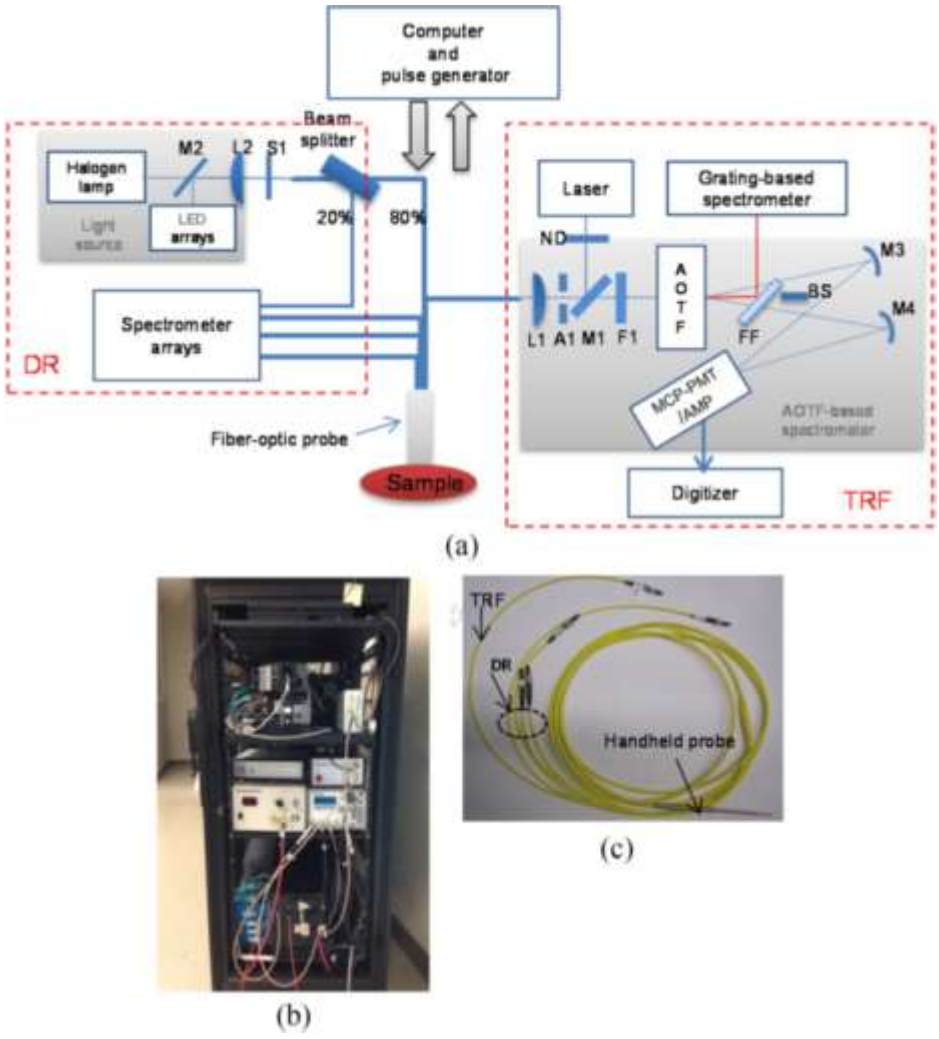

Fig. A.3 (a) The schematic view of an integrated spectroscopy system, (b) The integrated spectroscopy instrument housed in a mobile cart, (c) Sterilizable fiber optic probe used to collect fluorescence and reflectance signals. Reprinted from ref [65] in Chapter 1. Copyright © 2016, IEEE. Reprinted with permission.

A.3 Summary of previous research work

A.3.2 Measurement of optical properties in layered tissues

This work was performed in my first year (2010) as a research engineer at the Center for Devices and Radiological Health (CDRH) of the U.S. Food and Drug Administration (FDA). The objectives of this work were to develop and validate a fiber optics diffuse reflectance spectroscopy to measure optical properties of layered tissues using UV light. Mucosal tissues such as those lining the colon and cervix have two distinguished layers – the epithelium on top and the stroma at the bottom. During neoplastic progression, optical properties in each layer change differently. Therefore, accurate measurement of optical properties in each layer might improve mucosal disease diagnostics quality. The results showed that optical properties have mean errors of 19% from the theoretical analysis, and 27% from experiments, indicating that diffuse reflectance spectroscopy technique can provide moderately accurate estimates of optical properties in layered turbid media [1,2].

A.3.2 Quantification of vessel contrast in narrow-band and white light imaging

This work was performed in my second and third year (2011-2012) as a research engineer at CDRH-FDA [3-7]. Narrow band imaging (NBI) techniques have been widely used in the clinics as well as in research to enhance vessel contrast. However, prior to this work, theoretical analysis of NBI has not been the subject of extensive study in the biomedical optics literature, and widespread acceptance of supposed NBI mechanisms has occurred without rigorous validation. Specifically, tissue scattering was commonly cited as the primary mechanism behind spectral variations (415 to 540 nm) in vessel depth-

selectivity for clinical narrow band imaging of mucosa. In order to elucidate NBI mechanisms as well as white light imaging such as this in a quantitative manner, computational simulations and experimental measurements in tissue-simulating phantoms were performed [3-7]. The results showed that white light produced the lowest contrast for small vessels and intermediate contrast for large vessels at deep regions whereas 415 nm illuminations provided superior contrast for smaller vessels at shallow depths, and 540 nm provided superior contrast for larger vessels in deep regions. In addition, the simulation results indicated that the importance of three key mechanisms in determining spectral variations in contrast are: intravascular hemoglobin (Hb) absorption in the vessel of interest, diffuse Hb absorption from collateral vasculature, and bulk tissue scattering [3-7].

A.3.3 Measurement of skin oxygenation and perfusion

This work was performed during my graduate studies at the Catholic University at America (2010-2012). The objective of the study was to develop a skin sensor that allows measurement of oxygenation and perfusion of individuals with spinal cord injuries [8,9]. Wheelchair bound patients with a spinal cord injury likely experience pressure ulcers which are linked to skin hypoxia and loss of perfusion. Therefore, accurate measurements of skin oxygenation and perfusion can help to detect pressure ulcers. The sensor consists of a set of fiber optics probes, spectroscopic and Laser Doppler techniques that are used to obtain parameters of interest [8,9].

A.4 List of publications

Previous work

1. Q. Wang, V. N. Du Le, J. Ramella-Roman, J. Pfefer "Broadband UV-Vis optical property measurement in layered turbid media", Biomedical Optics Express **3** (6), 1226-1240 (2012).

2. V. N. Du Le, Q. Wang, J. Ramella-Roman, J. Pfefer , "Theoretical Analysis of a Technique for Broadband Optical Property Estimation in Two-layer Tissue" In CLEO: Applications and Technology, p. ATuB3. Optical Society of America, 2011 (Proceeding article & presentation).

3. V. N. Du Le, Q. Wang, T. Gould J. Ramella-Roman, J. Pfefer, "Vascular contrast in Narrow Band and white light imaging", Applied Optics **53** (18), 4061-4071 (2014).

4. V. N. Du Le, Q. Wang, J. Ramella-Roman, J. Pfefer "Monte Carlo modeling of light-tissue interactions in Narrow Band Imaging", Journal of Biomedical Optics **18** (1), 010504 (2013).

5. Q. Wang, V. N. Du Le, J. Ramella-Roman, J. Pfefer, "Spectral Variations in Narrow Band Imaging Depth-selectivity: Mucosal Scattering vs. Hemoglobin Absorption", In SPIE BiOS, pp. 85730N-85730N. International Society for Optics and Photonics, 2013 (Proceeding article & presentation).

6. V. N. Du Le, Q. Wang, J. Ramella-Roman, J. Pfefer , "Quantitative evaluation of mucosal vascular contrast in narrow band imaging using Monte Carlo modeling" In SPIE Defense, Security, and Sensing, pp. 836709-836709. International Society for Optics and Photonics, 2012 (Proceeding article & presentation).

7. J. Wang, J. Coburn, C. Liang, N. C. Woolsey, V. N. Du Le, J. C. Ramella-Roman, Y. Chen, J. Pfefer, "Characterization and application of 3D-printed phantoms for biophotonic imaging", In SPIE Defense, Security, and Sensing, pp. 87190Y-87190Y. International Society for Optics and Photonics, 2013 (Proceeding article & presentation).

8. J. Ramella-Roman, V. N. Du Le, A. Nguyen, A. Lichy, S.Groah, "Skin microvascular and metabolic response to pressure relief maneuvers in people with spinal cord injury", In SPIE BiOS, pp. 85790R-85790R. International Society for Optics and Photonics, 2013 (Proceeding article & presentation).

9. J. Ramella-Roman, T. Ho, V. N. Du Le, A. Nguyen, A. Lichy, S. Groah, "Monitoring the impact of pressure on the assessment of skin perfusion and oxygenation using a

novel pressure box", In SPIE BiOS, pp. 85760N-85760N. International Society for Optics and Photonics, 2013 (Proceeding article & presentation).

Current work

10. V. N. Du Le, M. S. Patterson, J. E. Hayward, T. J. Farrell, Q. Fang, "Optical Biopsy of Glioblastoma with Diffuse Reflectance Spectroscopy and Fluorescence Spectroscopy: Assessment of Optical properties, and Oxygen Saturation" Journal of Biomedical Optics (under review).

11. Z. Nie, V. N. Du Le, D. Cappon, J. Provias, N. Murty, J. E. Hayward, T. J. Farrell, M. S. Patterson, W. McMillan, and Q. Fang "Integrated Time-resolved Fluorescence and Diffuse Reflectance Spectroscopy Instrument for Intraoperative Detection of Brain Tumor Margin," J. Selected Topic in Quantum Electronics, IEEE **22**(3): 6802109 (2016).

12. V. N. Du Le, M. S. Patterson, T. J. Farrell, J. E. Hayward, Q. Fang, "Experimental recovery of intrinsic fluorescence and fluorophore concentration in the presence of hemoglobin: spectral effect of scattering and absorption on fluorescence," Journal of Biomedical Optics **20** (12), 127003 (2015).

13. V. N. Du Le, Z. Nie, J. E. Hayward, T. J. Farrell, Q. Fang, "Measurements of extrinsic fluorescence in Intralipid and polystyrene microspheres", Biomedical Optics Express **5** (8):2726-2735 (2014).